Ellen Gottschämmer

# Kinematic and Dynamic Simulation of Ground Motion: Implications for Seismic Hazard Assessment

Cuvillier Verlag Göttingen

# Kinematic and Dynamic Simulation of Ground Motion: Implications for Seismic Hazard Assessment

---

# Verbesserung der seismischen Gefährdungsabschätzung durch kinematische und dynamische Modellierung seismischer Bodenbewegung

Zur Erlangung des akademischen Grades eines

DOKTORS DER NATURWISSENSCHAFTEN

von der Fakultät für Physik der
Universität Karlsruhe (TH)
genehmigte

**DISSERTATION**

von

Dipl.-Geophys. Ellen Gottschämmer
aus Herborn/Lahn-Dill-Kreis

| | |
|---|---|
| Tag der mündlichen Prüfung: | 19. Juli 2002 |
| Referent: | Prof. Dr. Friedemann Wenzel |
| Korreferent: | Prof. Dr. Karl Fuchs |

Die Deutsche Bibliothek - CIP-Einheitsaufnahme

**Gottschämmer, Ellen:**
Kinematic and Dynamic Simulation of Ground Motion: Implications for Seismic Hazard Assessment : Verbesserung der seismischen Gefährdungsabschätzung durch kinematische und dynamische Modellierung seismischer Bodenbewegung / von Ellen Gottschämmer. - 1. Aufl. - Göttingen : Cuvillier, 2002
Zugl.: Karlsruhe, Univ. (TH), Diss., 2002
ISBN 3-89873-525-7

© CUVILLIER VERLAG, Göttingen 2002
Nonnenstieg 8, 37075 Göttingen
Telefon: 0551-54724-0
Telefax: 0551-54724-21
www.cuvillier.de

Alle Rechte vorbehalten. Ohne ausdrückliche Genehmigung des Verlages ist es nicht gestattet, das Buch oder Teile daraus auf fotomechanischem Weg (Fotokopie, Mikrokopie) zu vervielfältigen.
1. Auflage, 2002
Gedruckt auf säurefreiem Papier

ISBN 3-89873-525-7

# Zusammenfassung

In dieser Arbeit wird anhand von drei Beispielen gezeigt, wie die seismische Gefährdungsabschätzung erdbebengefährdeter Gebiete verbessert werden kann. Das Wellenfeld der Erdbeben wird dazu mit der Methode der Finiten Differenzen (FD) berechnet, die für die aktuellen seismologischen Fragestellungen weiterentwickelt, verbessert und angepasst wurde.
Die seismische Gefährdungsabschätzung hat sich in den letzten Jahren auf internationalem Gebiet zu einem bedeutsamen Forschungsbereich entwickelt. Die vielfältigen Fragestellungen verbinden jedoch nicht nur Wissenschaftler verschiedener Länder, sondern führen auch zu einer fruchtbaren interdisziplinären Zusammenarbeit und zum Austausch zwischen Geowissenschaftlern, Ingenieuren und Politikern.

## Einleitung

Die Modellierung des Wellenfeldes von Erdbeben mit der FD-Methode hat in den letzten Jahren eine weite Verbreitung gefunden [52, 71, 88, 111, 118]. Hierbei wird die Wellenausbreitung in einem räumlich begrenzten Volumen $V$ berechnet, in das die Quelle eingeschlossen ist. Dieses Volumen wird räumlich diskretisiert, indem man es mit einem nummerischen Gitter überzieht. An jedem Gitterpunkt wird die Wellengleichung gelöst. Deren partielle Ableitungen werden in der nummerischen Methode durch endliche (finite) Differenzen ersetzt.
In den frühen 80-er Jahren des 20. Jahrhunderts ermöglichten die Rechenkapazitäten die Berechnung des Wellenfeldes nur im zweidimensionalen Raum [134, 135]. Die rasante Entwicklung der Computertechnologie gestattete es, Anfang der 90-er Jahre Wellenausbreitung in kleinen dreidimensionalen Modellen zu berechnen [103]. Der Spektralgehalt der Seismogramme war dabei für typische Epizentraldistanzen von etwa 30 – 50 Kilometern auf Frequenzen unterhalb von 0,5 Hertz beschränkt, da die Maximalfrequenz des berechneten Signals umgekehrt proportional zum Abstand zwischen zwei Gitterpunkten ist (vgl. Kapitel 1). Moderne Parallelrechner bieten

mittlerweile die Möglichkeit, auch höherfrequente Signale (z.B. bis zu 1 – 1,5 Hertz [49, 88]) oder Wellenausbreitung in größeren Modellen zu simulieren. Die Anwendungen der FD-Modellierung erstrecken sich heute über mehrere Größenordnungen: Sie beinhalten lokale Untersuchungen wie z.B. Wellenausbreitung in schmalen Bruchzonen [63, 66, 124] oder vulkanischen Strukturen [92]. Eine typische Anwendung für die Untersuchung regionaler Effekte stellt die Berechnung von Erdbebenwellen in Grabenstrukturen [49, 104, 106, 118] oder die Simulation großer historischer [89, 93, 111] oder hypothetischer [59, 105] Beben dar. Im großen Maßstab konnte seismische Wellenausbreitung erfolgreich für die Unterkruste [73], den oberen Mantel [132] und in komplexen globalen Erdmodellen [64, 65] simuliert werden.
Die in dieser Arbeit vorgestellten Anwendungen enstammen dem Bereich der seismischen Gefährdungsabschätzung. Die Quantifizierung der seismischen Gefährdung einer Region schafft die notwendigen Vorbedingungen für die Erstellung von Bauvorschriften, die Gebäude, Brücken und Infrastruktur bei zukünftigen Erdbeben vor dem Zusammenbruch bewahren sollen. Sie hilft somit, Menschenleben zu retten, die Zahl der Verletzten zu reduzieren und die Versorgung der Überlebenden zu gewährleisten. Es ist deshalb nicht verwunderlich, dass sowohl öffentliches als auch wissenschaftliches Interesse an diesem Thema in den letzten Jahren deutlich angestiegen sind und auf dem Gebiet der seismischen Gefährdungsabschätzung sehr gute Fortschritte erzielt wurden. Diese Tatsache spiegelt sich in einer Vielzahl von Veröffentlichungen zu den Methoden der seismischen Gefährdungsabschätzung wider [15, 18, 20, 25, 34, 35, 39, 53, 90, 110, 139]. Grundsätzlich lassen sich zwei Ansätze unterscheiden: Bei der deterministischen Gefährdungsabschätzung wird die Bodenbewegung des größten Bebens, das in der Region aufgetreten ist, als Grundlage für Bauvorschriften herangezogen. Da die Bodenbewegung nicht an jedem Ort bekannt ist, wird eine vom Epizentrum radial abklingende Maximalamplitude angenommen, die sich mit empirisch bestimmten Abklingkurven [3, 6, 21, 22, 68, 117] berechnen lässt. Eine weitere Möglichkeit, mit dem deterministischen Ansatz die Bodenbewegung flächendeckend zu bestimmen, bietet die Methode der Finiten Differenzen. Die probabilistische Gefährdungsabschätzung bedient sich eines anderen Ansatzes. Hier wird die Wahrscheinlichkeit berechnet, mit der die Bodenbewegung einer bestimmten Stärke in einem gewissen Zeitraum eintritt. Die Ergebnisse der Gefährdungsabschätzung werden in regionalen und globalen Gefährdungskarten [40, 91, 125, 126] zusammengestellt.
Trotz der eindrucksvollen Entwicklung des Forschungsgebiets gibt es jedoch auch Defizite und Probleme, die bisher nicht behoben werden konnten. Ein Haupt-

kritikpunkt bei der Abschätzung der seismischen Gefährdung einer Region ist die Tatsache, dass die Dynamik der Erdbebenquelle bisher nicht in die Berechnungen mit einfließt. Hierzu zählt sowohl die oben angesprochene Bruchdynamik bei der Simulation synthetischer Seismogramme mit der Methode der Finiten Differenzen, als auch die Tatsache, dass der Bebenherd bei der Interpolation der Bodenbewegung mit Abklingkurven rechnerisch durch eine Punktquelle angenähert wird. Auch die lokalen Untergrundstrukturen werden bei der Berechnung der seismischen Gefährdung häufig nicht berücksichtigt. Lokale Beckenstrukturen oder eine oberflächennahe Gesteinsschichtung können die Amplitude der Bodenbewegung durch Fokussierungs- oder Resonanzeffekte deutlich erhöhen. Zonen erniedrigter seismischer Geschwindigkeit können als Wellenleiter wirken und seismische Energie in Gebiete transportieren, die weit vom Epizentrum entfernt liegen. Das Ziel der vorliegenden Arbeit ist es, diese Effekte zu quantifizieren, um so die Methoden der seismischen Gefährdungsabschätzung zu verbessern.

## Berechnung des Wellenfeldes

Die allgemeine Form der elastischen Bewegungsgleichung [4, 75] ergibt sich aus dem Kräftegleichgewicht zwischen der Trägheitskraft, die von der Dichte des Mediums $\rho$ und von der zweiten zeitlichen Ableitung der Bewegung $u_i$ abhängt, den Oberfächenkräften $\frac{\partial \sigma_{ij}}{\partial x_j}$ und den Volumenkräften $f_i$. Es gilt:

$$\rho \ddot{u}_i = \frac{\partial \sigma_{ij}}{\partial x_j} + f_i. \tag{1}$$

Die Komponenten des Spannungstensors $\sigma_{ij}$ werden über eine empirische Beziehung, das Hookesche Gesetz, mit denen des Deformationstensors des Mediums $\epsilon_{ij}$ verknüpft. Im isotropen Fall reichen zur Beschreibung zwei unabhängige Größen, die Laméschen Parameter $\lambda$ und $\mu$, und es gilt:

$$\sigma_{ij} = \lambda \epsilon_{kk} \delta_{ij} + 2\mu \epsilon_{ij}. \tag{2}$$

$\delta_{ij}$ steht hier für das Kronecker-Symbol. Die Voraussetzung der Homogenität des Mediums muss in diesem Fall nicht gegeben sein, d.h. $\lambda$ und $\mu$ können ortsabhängig sein.

Sind die betrachteten Deformationen $\epsilon_{ij}$ klein, so lassen sich diese durch die Verschiebungen $u$ ausdrücken:

$$\epsilon_{ij} = \frac{1}{2}(\frac{\partial u_i}{\partial x_j} + \frac{\partial u_j}{\partial x_i}). \quad (3)$$

Das Einsetzen von Gleichungen 2 und 3 in Gleichung 1 führt zu einem komplexen Gleichungssystem (vgl. Kapitel 1, Gleichungen 1.5 - 1.13), das mit der Finiten-Differenzen-Methode nummerisch gelöst wird. Die Berechnung wird für viele aufeinander folgende Zeitpunkte durchgeführt. Auf diese Weise erhält man an jedem Gitterpunkt ein Seismogramm.
Für die Implementierung der Quelle in das FD-Gitter gibt es zwei grundsätzlich unterschiedliche Ansätze. Zum einen kann man den Bruchverlauf durch die Definition einer Verschiebungsrate an jedem Punkt der Bruchfläche vorgeben. Diese Art der Implementierung empfiehlt sich für kleine Erdbeben, die als Punktquellen realisiert werden (vgl. Kapitel 2), für Erdbeben, deren Bruchfläche mit einem Winkel von $90^o$ einfällt (vgl. Kapitel 3), und für Bruchflächen, die tief in der Erde liegen (vgl. Kapitel 4). Soll das Beben auf einer schräg liegenden Bruchfläche stattfinden, die nah an die Erdoberfläche reicht oder bei der die Oberfläche sogar bricht, so ist es empfehlenswert eine dynamische Quelle in das FD-Gitter einzubauen. Bei dieser Art der Implementierung ist der Bruchverlauf nicht vorgegeben, sondern kann sich während der Berechnung frei entwickeln. Diese Implementierung ist zwar mit einem deutlich größeren Rechenaufwand verbunden, die Seismogramme beinhalten aber auch dynamische Effekte, die zum Beispiel durch die Interaktion der Normalspannungen mit der freien Oberfläche entstehen. In Kapitel 4 werden diese dynamischen Effekte genauer untersucht.

## Fallstudie I: Erdbeben im Rheingraben

Die erste Fallstudie beschäftigt sich mit der Frage, wie genau ein elastisches Untergrundmodell bekannt sein muss, um die berechnete Wellenausbreitung für hochfrequente (1 – 8 Hertz) seismische Gefährdungsabschätzung verwenden zu können. Dieser Frequenzbereich ist speziell in Mitteleuropa interessant für die Bestimmung der seismischen Gefährdung, da Eigenfrequenzen ein- bis zweistöckiger Gebäude in diesem Bereich liegen. Der Frequenzgehalt von 3D FD-Simulationen ist momentan auf Frequenzen unterhalb von etwa 1 – 1,5 Hertz beschränkt. Hierfür gibt es zwei Gründe. Zum einen begrenzt die Rechenkapazität selbst moderner Computer die Anzahl der Gitterpunkte im Modell und somit indirekt die Maximalfrequenz des Wellenpakets. Der zweite Grund liegt in der unzureichenden Kenntnis der geologischen Untergrundmodelle. Selbst wenn uns die sich ständig weiterentwickelnde

Computertechnologie sicher bald in die Lage versetzen wird Wellenausbreitung für Frequenzen bis 8 Hertz auch in drei Dimensionen zu berechnen, bleibt das Problem, dass die geologischen Modelle auf der Skala einer Wellenlänge (z.B. 250 m bei 8 Hertz und einer minimalen S-Wellengeschwindigkeit von 2 km/s) in den wenigsten Fällen bekannt sind. Dies aber wäre die Voraussetzung für die Rekonstruktion detailgetreuer Wellenformen. Für die Abschätzung der seismischen Gefährdung ist eine Simulation der exakten Wellenformen jedoch im Allgemeinen nicht notwendig. Bei der Bestimmung der seismischen Gefährdung spielen z.B. nur die Maximalwerte der Bodenschwinggeschwindigkeit und die spektrale Beschleunigungsantwort eine Rolle. Wenn sich diese Parameter mit einem heute bekannten Geschwindigkeitsmodell rekonstruieren lassen, kann es für die Bestimmung der seismischen Gefährdung verwendet werden. In Kapitel 2 wird das Wellenfeld dreier Beben mit Lokalmagnituden $M_L$ 3,5 – 3,6 im Frequenzbereich von 1 – 8 Hertz in einer 2D FD-Rechnung simuliert. Die in dieser Arbeit vorgestellten Berechnungen verwenden Quellparameter von Erdbeben, die in den Jahren 1996 und 1997 im Rheingraben stattgefunden haben [12, 13]. Gerade im Rheingraben spielt die Verwendung der FD-Methode für die Bestimmung der seismischen Gefährdung eine besondere Rolle, da für das letzte große Beben ($M_L = 6.5$), das im Jahre 1356 in der Nähe von Basel (Schweiz) stattgefunden hat [77], keine instrumentellen Aufzeichnungen existieren. Dies ist eine typische Situation für seismische Regionen in dem Inneren tektonischer Platten. Hier liegt das Wiederkehrintervall von Großereignissen bei bis zu mehreren tausend Jahren [25]. Auch für den Rheingraben ist es also durchaus denkbar, dass ein Beben dieser Stärke wieder auftritt. Um eine Aussage über die Güte der simulierten Seismogramme machen zu können, werden die synthetisch erzeugten Seismogramme mit registrierten Seismogrammen von 5 Stationen verglichen. Drei dieser Einkomponenten-Stationen (LIBD, FBB, BBS) liegen auf dem Sedimentgestein des Rheingrabens, während die Station FBB in der Nähe des Gipfels des Feldbergs im Schwarzwald steht. Eine weitere Station (MOF) gehört zum französischen Netzwerk ReNaSS (Réseau National de Surveillance Sismique) und befindet sich in den Vogesen. Bei dem Vergleich werden verschiedene Parameter untersucht: Ein erster Test überprüft das elastische Modell durch einen Vergleich der Ankunftszeiten der ersten Phase (Kompressionswelle) in den synthetischen und aufgezeichneten Seismogrammen. Hier zeigen sich ganz unterschiedliche Ergebnisse: An den drei Stationen im Rheingraben konnten die Ankunftszeiten der Wellen des Bebens vom 24. August 1996, dessen Epizentrum in Dessenheim (Frankreich) lag, mit einer Genauigkeit von $\pm$ 0,1 Sekunden simuliert werden. Dies ist die beste

Übereinstimmung, die im gesamten Datensatz gefunden wurde. Die größte Abweichung trat für das Beben vom 17. November 1997 mit Epizentrum in der Nähe von Weil am Rhein (Deutschland) aufgezeichnet an der Station FELD im Schwarzwald auf. Hier betrug die Differenz zwischen den Ankunftszeiten des synthetischen und des registrierten Seismogramms 1,2 Sekunden. Der zweite Parameter, der in Kapitel 2 verglichen wird, ist der Maximalwert der Bodenschwinggeschwindigkeit. Dieser Parameter spielt bei der Bestimmung der seismischen Gefährdung eine entscheidende Rolle, da er aussagt, welcher Maximalbelastung ein Gebäude während eines Erdbebens standhalten muss. Die Maximalwerte in den synthetischen Seismogrammen liegen in einigen Fällen über den Werten der Realdaten, in anderen Fällen sind sie niedriger. Die Abweichungen betragen in den meisten Fällen nicht mehr als einen Faktor 2 – 3. In diesen Fällen könnten die Simulationen für die Abschätzung der seismischen Gefährdung verwendet werden. Der Fehler, der durch eine ungenaue Magnitudenbestimmung historischer Beben auftritt, liegt in der gleichen Größenordnung. In einigen Fällen zeigten sich beim Vergleich der Maximalgeschwindigkeiten jedoch auch Diskrepanzen bis zu einem Faktor 10. Diese Abweichung ist zu groß um die simulierten Seismogramme für die Gefährdungsabschätzung einzusetzen. Ein ähnlicher Schluss muss für die Vergleiche der anderen Parameter gezogen werden. Sowohl die Erschütterungsdauer, die definiert ist als die Zeit, in der zwischen 5% und 75% der kumulierten quadrierten Bodenbeschleunigung aufgezeichnet werden [130], als auch die Amplituden der spektralen Antwortwerte können in den meisten Fällen mit einer maximalen Abweichung von einem Faktor 2 – 3 simuliert werden. Für den Zweck der seismischen Gefährdungsabschätzung wäre dieser Fehler zu tolerieren. In einigen Fällen weichen die Werte der simulierten Seismogramme jedoch so stark von denen der aufgezeichneten Daten ab, dass die Ergebnisse für eine zuverlässige Gefährdungsabschätzung nicht zu verwenden sind. In Kapitel 2 werden mögliche Erklärungen für diese Abweichungen diskutiert: Um auszuschließen, dass der lokale Stationsuntergrund für die Diskrepanzen verantwortlich ist, wird das Verhältnis von P/S-Amplituden verglichen. Die Gesteinszusammensetzung in den oberen Dutzend Metern kann die Wellenformen durch Resonanzen stark verändern. Dieser Effekt ist in den FD-Simulationen nicht berücksichtigt. Geht man davon aus, dass der Effekt die Amplituden von P- und S-Wellen in gleichem Maße beinflusst, so sollten die Amplitudenverhältnisse von P- zu S-Wellen frei sein von Einflüssen des lokalen Stationsuntergrunds und die Verhältnisse der simulierten und der aufgezeichneten Seismogramme sollten übereinstimmen. Das ist jedoch nicht der Fall. Eine weitere mögliche Erklärung für die Unterschiede der Seismogramme könnte darin liegen,

dass Materialdämpfung bei der Berechnung der Seismogramme mit der FD- Methode aus Gründen der Rechenzeit nicht berücksichtigt wurde. Eine ähnliche Studie [46] zeigte, dass die Maximalamplitude von Scherwellen für Epizentraldistanzen zwischen 40 und 60 Kilometern um etwa 22% reduziert wird, wenn Dämpfung ($Q_P = 1500$ and $Q_S = 1000$) mit berücksichtigt wird. In einigen Fällen würde die Übereinstimmung somit verbessert werden, in anderen Fällen würde sie sich verschlechtern. Auch die Topografie des Geländes wurde in die FD-Berechnungen nicht mit einbezogen. Gerade für die Station FELD, die auf einer Höhe von knapp 1500 Metern liegt, sind hier Änderungen zu erwarten. Die Berücksichtigung der Topografie wirkt sich durch den längeren Laufweg sowohl auf die Einsatzzeiten der Wellen in den Seismogrammen als auch auf die Amplituden aus, da diese durch geometrische Streuung weiter gedämpft würden. Als eine weitere mögliche Ursache für die Unterschiede wird eine ungenaue Bestimmung der Herdparameter in Betracht gezogen. Der Herdparameter mit der größten Ungewissheit ist die Herdtiefe [131]. Die Herdtiefen, die durch das Landesamt für Geologie, Rohstoffe und Bergbau in Baden-Württemberg bestimmt wurden, haben Fehlergrenzen von bis zu 5 Kilometern bei Herdtiefen zwischen 7 und 17 Kilometern. In einer Vorstudie zu dieser Arbeit [47] konnte gezeigt werden, dass die Bodenbewegung um den Faktor 2 ansteigt, wenn die Tiefe des Hypozentrum von 15 auf 10 Kilometer angehoben wird. Die bisher diskutierten Fehlerquellen erklären alle nur einen kleinen Teil der Unterschiede zwischen registrierten und simulierten Seismogrammen. Als wahrscheinlichste Erklärung für den Unterschied zwischen gemessenen und synthetischen Daten erscheint die Ungenauigkeit und die geringe Auflösung des elastischen Modells. Hochauflösende aktive seismische Experimente sind erforderlich um das Untergrundmodell zu verbessern, so dass es für die Abschätzung der seismischen Gefährdung der Region verwendet werden kann. Außerdem wäre eine flächendeckende und dauerhafte Installation von modernen Dreikomponenten-Seismometern zu wünschen um die Datenqualität zu verbessern.

## Fallstudie II: Jericho-Erdbeben

Die Auswirkungen der Bruchdynamik und der Einfluss eines Sedimentbeckens auf die Amplituden der Bodenbewegung werden in einer zweiten Fallstudie in Kapitel 3 anhand des Jericho-Bebens untersucht. Beide Effekte sind in radialsymmetrischen Abklingkurven, wie sie für die Amplitudeninterpolation bei der seismischen Gefährdungsabschätzung verwendet werden, nicht enthalten [3, 6, 21, 22, 68, 117]. Die

Berechnungen in Kapitel 3 quantifizieren den Einfluss der Bruchdynamik und der großflächigen Untergrundstrukturen. Sie zeigen durch die Simulation des Wellenfeldes eines Bebens mit Lokalmagnitude $M_L = 6{,}2$ in einem einfachen Grabenmodell [5, 37], dass für große Beben und für heterogene Modelle beide Parameter einen entscheidenden Einfluss auf die Amplituden der Bodenbewegung haben. Die Berechnungen stellen ein historisches Beben nach, das am 11. Juli 1927 in der Nähe der Stadt Jericho am nördlichen Ende des Toten-Meer-Beckens stattgefunden hat. Dieses Ereignis ist das jüngste in der über 4000 Jahre alten Geschichte großer ($M_L > 6.0$) Beben, die alle entlang der Verwerfungszone des Toten Meers aufgetreten sind. Es ist das Einzige dieser Beben, für das präzise Informationen über die Lage der Quelle und die Schadensverteilung zur Verfügung stehen [96, 123, 127]. Die makroseismische Intensitätsverteilung zeigt eine ungewöhnlich deutliche Ausprägung großer Intensitätswerte in Richtung Norden. Weiterhin ungewöhnlich ist die Lage des Intensitätsmaximums (Intensität X), das etwa 50 Kilometer nördlich vom Epizentrum entfernt zu finden ist. Zwei weitere Gebiete hoher Intensität (VIII – IX) liegen etwa 100 Kilometer nördlich des Epizentrums. Die hier gefundene Abweichung von einer radial abklingenden Bodenbewegung wurde auch bei anderen Ereignissen in der Region beobachtet [127, 141]. Eine mögliche Erklärung des Phänomens könnte in der Untergrundstruktur des Beckens liegen, von dem vermutet wird, dass es mit seiner langen Ausdehnung wie ein Wellenleiter wirkt [140]. Die FD-Berechnungen in Kapitel 3 bestätigen diese Annahme und weisen außerdem auf die Bedeutung des Einflusses der Bruchdynamik auf die Amplituden der Bodenbewegung hin. Die Untersuchungen beinhalten die Analyse des Wellenfeldes anhand der flächenhaften Amplitudenverteilung an der Oberfläche zu verschiedenen Zeitpunkten. Weiterhin werden Seismogramme an ausgewählten Stationen im Becken und auf dem anstehenden Gestein untersucht. Es werden Maximalwerte der Bodenschwinggeschwindigkeit sowie spektrale Beschleunigungen ($Y_{FD1}$) bei einer Frequenz von einem Hertz berechnet. Um den Untergrundeffekt zu eliminieren werden die spektralen Beschleunigungen des Beckenmodells mit spektralen Beschleunigungen verglichen, die in einem elastischen Halbraum mit der FD-Methode berechnet wurden ($Y_{FD2}$). Ein zweiter Vergleich wird mit spektralen Beschleunigungen durchgeführt, die mit einer Abklingrelation ($Y_{AR}$) berechnet wurden. Durch die Berechnung der Verhältnisse $R_{FD} = Y_{FD1}/Y_{FD2}$ und $R_{AR} = Y_{FD1}/Y_{AR}$ lassen sich die Ursachen für die Abweichung von einer radialen Verteilung der Bodenbewegung separieren und erklären. Wenn $R_{FD}$ große Werte annimmt, deutet das auf eine Verstärkung der Amplituden durch die Untergrundstruktur hin, da alle anderen

Parameter in den beiden FD-Berechnungen übereinstimmen. Im Gegensatz dazu weisen hohe Werte von $R_{AR}$ auf den Einfluss der Bruchdynamik hin, da er in der Berechnung der spektralen Beschleunigungen mittels Abklingkurven nicht enthalten ist. $R_{AR}$ kann auch dann hohe Werte annehmen, wenn die Amplituden der Seismogramme aus der FD-Berechnung durch Reflexionen erhöht worden sind. Solche Reflexionen können zum Beispiel am Rande des Beckens auftreten. Kleine Werte von $R_{AR}$ (Verstärkungen deutlich kleiner als ein Faktor 2) finden sich südlich des Epizentrums. Sie steigen in Richtung Norden langsam an. Das größte Verhältnis tritt am Rande des Beckens auf ($R_{AR} = 5{,}1$) und rührt von Reflexionen her, die in die Berechnung von $Y_{AR}$ nicht mit einfließen. In der Nähe des Epizentrums nimmt $R_{AR}$ Werte von 2,0 – 2,5 an, die durch die Bruchdynamik erklärt werden können. Der Einfluss des Untergrundes wiegt schwerer: Das Verhältnis $R_{FD}$ beträgt auf dem Sedimentgestein etwa einen Faktor 4. Die Amplitudenverstärkung durch die Reflexionen lässt sich auch hier beobachten, da die Schichtgrenze, an der die Reflexionen auftreten, im Halbraum nicht vorhanden sind. Auch hier findet sich eine Verstärkung um den Faktor 5,1. Die Ergebnisse aus Kapitel 3 zeigen somit (a) den bedeutenden Einfluss der Untergrundstruktur, die in die Berechnung der seismischen Gefährdung Israels bisher nicht eingeht, und (b), dass dieser Einfluss für ein Beben der Magnitude 6,2 sogar größer ist als der der Bruchdynamik. Für stärkere Beben und die damit verbundenen größeren Bruchflächen [138] kann sich diese Reihenfolge herumdrehen.

## Fallstudie III: Erdbeben auf schräg liegenden Bruchflächen

Die Bodenbewegung von Erdbeben mit schräg liegenden Bruchflächen wird in Kapitel 4 untersucht. Im Nahfeld eines Erdbebens ist die Verteilung der Bodenbewegung von Beben mit Fallwinkeln $\theta \neq 90^o$ häufig asymmetrisch. Im Hangenden treten deutlich größere Bodenschwinggeschwindigkeiten auf als im Liegenden. Dieser Effekt kann dadurch erklärt werden, dass die Normalspannungen auf der Bruchfläche durch die freie Oberfläche noch während des Bruchvorgangs beeinflusst werden, was sich auf die Fortsetzung des Bruchs auswirkt. Dieses Zusammenspiel wird als dynamische Interaktion bezeichnet und ist noch nicht vollständig verstanden. Am auffälligsten ist es bei flach liegenden Bruchflächen. Die Ausprägung der Asymmetrie der Bodenbewegung hängt weiterhin vom Fallwinkel ab. Die in der seismischen Gefährdungsabschätzung beliebte Berechnung von hypothetischen Erdbeben mit herkömmlichen FD-Methoden beinhaltet diese dynamische Interaktion im All-

gemeinen nicht. Bei der Berechnung von Beben, die durch eine Punktquelle oder durch eine senkrecht liegende Bruchfläche charakterisiert werden (z.B. in Kapitel 2 und 3), tritt der Effekt nicht auf. Hier empfehlen sich FD-Methoden, die die dynamische Interaktion nicht berücksichtigen, da sie deutlich weniger rechenintensiv sind. Bei der Simulation von Beben auf schräg liegenden Bruchflächen, besonders wenn diese in die Nähe der Oberfläche reichen, ist die Berücksichtigung des Effekts dynamischer Interaktion jedoch notwendig. Es ist nicht sehr wahrscheinlich, dass dies routinemässig in naher Zukunft geschehen wird, da zum einen die Implementierung der Bruchdynamik in vorhandene FD-Programme sehr zeitaufwändig ist und die FD-Rechnungen einen grösseren virtuellen Speicher als auch eine deutlich längere Rechenzeit brauchen. In Kapitel 4 werden verschiedene Szenarien von Beben auf schräg liegenden Verwerfungen mit Fallwinkeln von $30^o$, $45^o$ und $60^o$ in einem homogenen Halbraum berechnet. Die Oberkanten der Verwerfungen liegen zwischen null Kilometern (Bruch reicht bis an die Oberfläche) und 5 Kilometern Tiefe. Die Seismogramme werden sowohl mit als auch ohne dynamische Interaktion berechnet. So kann zum Einen ein Schwellenwert für die Tiefenlage der Oberkante der Bruchfläche bestimmt werden, unterhalb der die dynamische Interaktion zu vernachlässigen ist, und zum Zweiten kann der Effekt der dynamischen Interaktion für geringe Tiefen quantifiziert werden. Diese Korrekturen können dann bei zukünftigen Berechnungen hypothetischer Beben, die die dynamische Interaktion nicht berücksichtigt haben, auf die Amplituden der Bodenbewegung aufaddiert werden. In Kapitel 4 werden zunächst die Bodenbewegungen an der Oberfläche und in Vertikalschnitten sowie die Spannungsverteilung auf der Bruchfläche visualisiert. Vorgehende Untersuchungen [2, 24, 28, 30, 54, 67, 82, 97] verifizierend wird gezeigt, dass die ungleichmässige Verteilung der Bodenbewegung auf die Interaktion der Normalspannungen mit der freien Oberfläche zurückzuführen ist. Die Untersuchung zeigt, dass die stärksten dynamischen Effekte für Bruchflächen auftreten, die bis zu einem Kilometer an die Oberfläche herankommen. Amplitudenverstärkungen der Bodenschwinggeschwindigkeit bis zu einem Faktor 3 werden durch Bruchgeschwindigkeiten verursacht, die oberhalb der Scherwellengeschwindigkeiten liegen. Am deutlichsten sind diese Effekte an der Oberfläche in einem Bereich von etwa 3 Kilometern (für einen Fallwinkel von $30^o$) bis zu 13 Kilometern (für einen Fallwinkel von $60^o$) um die Bruchfläche herum zu beobachten. Auch das seismische Moment, in dessen Berechnung die durchschnittliche Verschiebung auf der Bruchfläche mit eingeht, ändert sich unter Berücksichtigung der Bruchdynamik in den FD-Simulationen. Reicht der Bruch bis an die Oberfläche, so steigt das seismische Moment um bis zu 71% an.

Dieser stärkste Anstieg wurde für einen Fallwinkel von $60^o$ und für ein dynamisches Modell gefunden, bei dem nur die dynamische Abschwächung der Verschiebung berücksichtigt wird. Verwendet man ein realistischeres Modell, das auch noch die Abschwächung der Verschiebungsrate mit einbezieht, so ändern sich die Ergebnisse für die Maximalwerte der Bodenschwinggeschwindigkeit nicht. Das seismische Moment wird aber um einen Faktor von etwa 13% reduziert. Bei einer weiteren Untersuchung in Kapitel 4 wurden zuerst eine und dann zwei Schichten erniedrigter seismischer Geschwindigkeiten in das elastische Modell eingebaut. Der Effekt der dynamischen Interaktion der Normalspannungen mit der freien Oberfläche wird durch die Einfügung von Schichten mit erniedrigten Geschwindigkeiten verstärkt. Hier wird auf einer Bruchfläche mit einem Fallwinkel von $45^o$ sogar die neunfache Bodenschwinggeschwindigkeit erreicht. Dieser größte Wert wird nicht, wie erwartet, im Modell mit zwei Schichten erniedrigter Geschwindigkeit erreicht, sondern tritt im Modell auf, bei dem der Halbraum nur mit einer Schicht bedeckt ist. Er kommt durch ein Zusammenspiel zweier Faktoren zustande: die Verstärkung durch die Dynamik wird zusätzlich durch Resonanzeffekte in der obersten Schicht beeinflusst, was zu einer zusätzlichen Amplitudenverstärkung führt. Das seismische Moment steigt für die Berechnungen in den geschichteten Modellen um 72% (eine Schicht über einem Halbraum) bzw. 82% (zwei Schichten über einem Halbraum). Die Ergebnisse in Kapitel 4 zeigen somit, dass die dynamische Interaktion einen deutlichen Einfluss auf die Amplituden der Bodenschwinggeschwindigkeit hat und dass diese Effekte bei der Bestimmung der seismischen Gefährdung an flachen, schräg liegenden Bruchflächen berücksichtigt werden müssen.

# Contents

**Introduction** **15**

**1 Concepts of Finite Difference Modeling** **19**
1.1 Stability of a System . . . . . 21
1.2 Numerical Dispersion . . . . . 22
1.3 Staggered Grids and Accuracy of the System . . . . . 22
1.4 Lateral and Bottom Boundaries . . . . . 23
1.5 Free-Surface Boundary-Condition . . . . . 24
1.6 Implementation of the Source . . . . . 25
1.6.1 Kinematic Ruptures . . . . . 25
1.6.2 Dynamic Ruptures . . . . . 28

**2 Case Study I: Rhinegraben-Earthquakes** **31**
2.1 Motivation . . . . . 31
2.2 Upper Rhinegraben . . . . . 32
2.2.1 Tectonics and Geology . . . . . 32
2.2.2 Seismicity . . . . . 33
2.2.3 Three Rhinegraben Earthquakes ($M_L$ 3.5 – 3.6) . . . . . 33
2.3 Modeling Parameters . . . . . 35
2.3.1 Elastic Model and Geometry . . . . . 35
2.3.2 Computational Parameters . . . . . 37
2.4 Numerical Results . . . . . 38
2.4.1 Arrival Times of P-Waves . . . . . 39
2.4.2 Peak Ground Velocities . . . . . 40
2.4.3 Amplitude Ratios . . . . . 42
2.4.4 Duration of Shaking . . . . . 44
2.4.5 Response Spectra . . . . . 44
2.5 Discussion . . . . . 45

**3 Case Study II: The 1927 Jericho Earthquake 51**
3.1 Motivation . . . 51
3.2 Dead Sea Rift Transform Fault . . . 52
3.2.1 Tectonics and Geology . . . 52
3.2.2 Seismicity . . . 52
3.2.3 The 1927 Jericho Earthquake . . . 52
3.3 Modeling Parameters . . . 54
3.3.1 Elastic Model and Geometry . . . 54
3.3.2 Computational Parameters . . . 55
3.4 Numerical Results . . . 56
3.4.1 Snapshots of the Wavefield . . . 56
3.4.2 Seismograms . . . 57
3.4.3 Peak Ground Velocities . . . 58
3.4.4 Spectral Accelerations . . . 59
3.5 Discussion . . . 62

**4 Case Study III: Earthquakes on Dipping Faults 65**
4.1 Motivation . . . 65
4.2 Modeling Parameters . . . 67
4.2.1 Elastic Model and Geometry . . . 67
4.2.2 Dynamic Computational Parameters . . . 67
4.2.3 Kinematic Computational Parameters . . . 69
4.3 Numerical Results . . . 70
4.3.1 Uniform Halfspace (UHS) Model . . . 70
4.3.2 Layered Model, $45^o$ Dipping Thrust Fault . . . 75
4.3.3 Variation of Initial Stress Distribution . . . 79
4.3.4 Deeper Versus Shallower Events . . . 86
4.4 Discussion . . . 87

**Summary 89**

**A Free-Surface Boundary-Condition 95**
A.1 Explicit Free-Surface Boundary-Condition . . . 96
A.1.1 Free-Surface Boundary-Condition FS1 . . . 96
A.1.2 Free-Surface Boundary-Condition FS2 . . . 97
A.2 Source and Receiver Configuration and Model Description . . . 98
A.3 Numerical Results . . . 99

A.3.1 Comparison Between FS1 and FS2 . . . . . 99
A.3.2 Refinement of FS1 and FS2 . . . . . 101

**Bibliography** **105**

**Acknowledgements** **119**

**Lebenslauf** **121**

# List of Figures


1.1 Staggering of the Wavefield Parameters . . . . . 23
1.2 Prevention of Artificial Reflections by an Exterior Grid and an Explicit Boundary-Condition . . . . . 24
1.3 Mapping of Dipping Faults Onto the Numerical Grid . . . . . 28

2.1 Map of the Upper Rhinegraben . . . . . 34
2.2 Vertical Component Velocity Seismograms Recorded at Five Stations in the Rhinegraben, the Vosges Mountains, and in the Black Forest . 36
2.3 Compressional Wave Model of the Rhinegraben . . . . . 37
2.4 Horizontal and Vertical Component Velocity Seismograms Computed Along Profile 1 in the Rhinegraben. . . . . 39
2.5 Data and Synthetics for a $M_L = 3.5$ Earthquake on August 24, 1996 Recorded and Computed at Stations MOF, FBB, LIBD and BBS . . 40
2.6 Data and Synthetics for a $M_L = 3.6$ Earthquake on February 1, 1997 Recorded and Computed at Stations LIBD and BBS . . . . . 41
2.7 Data and Synthetics for a $M_L = 3.5$ Earthquake on November 17, 1997 Recorded and Computed at Stations FBB, BBS and FELD . . . 42
2.8 Response Spectra for Three Rhinegraben Earthquakes . . . . . 46

3.1 Map of the Dead Sea Rift Transform and the Dead Sea Basin . . . . 53
3.2 Distribution of Macroseismic Intensity for the 1927 Jericho Earthquake 55
3.3 Model of Elastic Parameters used for the Modeling of the Jericho Earthquake . . . . . 56
3.4 Snapshots of the Wavefield at the Surface for the Jericho Earthquake 58
3.5 Velocity Seismograms Calculated at the Surface for the Jericho Earthquake . . . . . 59
3.6 Vertical and Horizontal Components of Peak Ground Velocities ($v_r$ = 70% $v_s$) for the Jericho Earthquake . . . . . 60
3.7 Averaged Spectral Acceleration Response for the Jericho Earthquake 61

3.8 Averaged Horizontal Component of Peak Ground Velocities ($v_r$ = 90% $v_s$) for the Jericho Earthquake . . . . . 63

4.1 Illustration of the Time-Dependent Normal-Stress Effects . . . . . 66
4.2 Modeling Area and Location of Three Profiles for Simulations of Ground Motion on Dipping Faults . . . . . 68
4.3 Final Slip Distribution for an Earthquake on a $45^o$ Dipping Fault . . 70
4.4 Snapshots of the Wavefield for a $45^o$-Dipping Thrust Fault in the UHS Model . . . . . 73
4.5 Ratios Between Peak Displacements and Peak Velocities on a $45^o$-Dipping Fault Including Slip- and Sliprate-Weakening Friction . . . . 74
4.6 Ratios Between Peak Displacements and Peak Velocities on a $45^o$-Dipping Fault Including Only Slip-Weakening Friction . . . . . 75
4.7 Velocity Seismograms for a $45^o$-Dipping Thrust Fault in the UHS Model 76
4.8 Snapshots of Normal Stress on the Fault Plane for a $45^o$-Degree Dipping Thrust Fault in the UHS Model . . . . . 77
4.9 Snapshots of the Sliprate on a $45^o$-Dipping Fault in the UHS Model . 78
4.10 Ratios Between Peak Displacements and Peak Velocities on a $30^o$-Dipping Fault Including Only Slip-Weakening Friction . . . . . 79
4.11 Ratios Between Peak Displacements and Peak Velocities on a $60^o$-Dipping Fault Including Only Slip-Weakening Friction . . . . . 79
4.12 Snapshots of the Sliprate on a $45^o$, $30^o$, and $60^o$, Dipping Fault in the UHS Model and on a $45^o$-Dipping Fault in the UHS, 1LOH and the 2LOH Models . . . . . 80
4.13 Dynamically and Kinematically Computed Velocity Seismograms for a $45^o$-Dipping Thrust Fault in the 1LOH Model . . . . . 81
4.14 Dynamically and Kinematically Computed Velocity Seismograms for a $45^o$-Dipping Thrust Fault in the 2LOH Model . . . . . 82
4.15 Dynamically Computed Velocity Seismograms for a $45^o$-Dipping Thrust Fault in the UHS and 1LOH Model . . . . . 83
4.16 Dynamically Computed Velocity Seismograms for a $45^o$-Dipping Thrust Fault in the UHS and 2LOH Model . . . . . 84
4.17 Ratios Between Peak Displacements and Peak Velocities on a $45^o$-Dipping Fault for the 1LOH and 2LOH Models . . . . . 85
4.18 Variations of Initial Stress Distributions for Earthquakes on Dipping Faults . . . . . 86

4.19 Acceleration Response Spectra for a $M_W$ 7.0 Event and for a $M_W$ 7.1 Event . . . . . 87

A.1 Source Time Function for the Accuracy Test . . . . . 98
A.2 Misfit for FS1 and FS2 . . . . . 100
A.3 Surface Velocity Time-Histories for FS1 and FS2 . . . . . 102
A.4 Averaged Surface Velocity Time-Histories for FS1 and FS2 . . . . . 103

# List of Tables


2.1 Source Parameters for Three Rhinegraben Events . . . . . 35
2.2 Geographical Coordinates for Five Seismic Stations in the Rhinegraben, the Vosges Mountains, and the Black Forest . . . . . 35
2.3 Minimum and Maximum Elastic Parameters in the 3D Rhinegraben Model . . . . . 37
2.4 Profiles Used for the Rhinegraben Earthquake Simulations . . . . . 38
2.5 Geometrical Modeling Parameters Used for the Rhinegraben Earthquake Simulations . . . . . 38
2.6 Peak Ground Velocities for Compressional Waves for Three Rhinegraben Earthquakes . . . . . 41
2.7 Peak Ground Velocities for Shear Waves for Three Rhinegraben Earthquakes . . . . . 43
2.8 P/S Wave Amplitude Ratios for Data and Synthetics for Three Rhinegraben Earthquakes . . . . . 43
2.9 Duration of Shaking for Data and Synthetics for Three Rhinegraben Earthquakes . . . . . 44

3.1 Large Historic Earthquakes Connected to the Dead Sea Rift Transform Fault . . . . . 54
3.2 Geometrical Modeling Parameters Used for the Simulation of the Jericho Earthquake . . . . . 57

4.1 Model of Elastic Parameters Used for the Simulation of Ground Motion from Dipping Faults . . . . . 67
4.2 Geometrical Modeling Parameters Used for the Simulations of Ground Motion on Dipping Faults . . . . . 69
4.3 Dynamic Modeling Parameters Used for the Simulations of Ground Motion on Dipping Faults . . . . . 69
4.4 Seismic Dynamic/Prescribed Moment Ratios in a Halfspace Model . . 71

4.5 Seismic Dynamic/Prescribed Moment Ratios for $45^o$-Dipping Fault: Effects of Near-Surface Layers and Near-Surface Stress . . . . . 71

A.1 Geometrical Modeling Parameters for the Accuracy Test . . . . . 99

# List of Abbreviations and Symbols

| | | |
|---|---|---|
| 1LOH | - | Model with one layer over a halfspace |
| 2D | - | Two-dimensional |
| 2LOH | - | Model with two layers over a halfspace |
| 3D | - | Three-dimensional |
| | | |
| b1 - b5 | - | Regression coefficient used in chapter 3, equation 3.1 |
| BBS | - | Seismometer station in the Rhinegraben (Switzerland) |
| $c$ | - | Constant used in computation of stability criterion |
| $\mathbf{d}$ | - | Unit vector in direction of slip |
| $\mathbf{D}$ | - | Slip vector |
| $\dot{\mathbf{D}}$ | - | Slip rate vector |
| $D_c$ | - | Slip weakening distance |
| $D_n^l$ | - | FD approximation to differential operator in direction $l$ at level $n$ |
| DSB | - | Dead Sea Basin |
| DSR | - | Dead Sea Rift |
| $dt$ | - | Temporal sampling interval |
| $dx$ | - | Spatial sampling interval |
| E | - | East |
| EDHD | - | Ratio of epicentral and hypocentral distance |
| $f$ | - | Frequency |
| $\mathbf{f}$ | - | Body forces |
| $f_{\max}$ | - | Maximum frequency included in a simulation |
| FBB | - | Seismometer station in the Rhinegraben |
| FD | - | Finite Differences |
| FELD | - | Seismometer station in the Black Forest |
| FS1 | - | Free surface position colocated with the normal stresses |
| FS2 | - | Free surface position located half a grid point vertically from FS1 |
| $g$ | - | Constant used in computation of dispersion criterion |

| | | |
|---|---|---|
| Hz | - | Hertz |
| km | - | Kilometers |
| LIBD | - | Seismometer station in the Rhinegraben (Germany) |
| m | - | Meters |
| $\mathbf{M}$ | - | Seismic moment tensor |
| $M_0$ | - | Scalar seismic moment |
| $M_{ij}$ | - | Elements of the moment tensor |
| $\dot{M}_{ij}$ | - | Elements of the moment rate tensor |
| $M_L$ | - | Local magnitude |
| $M_W$ | - | Moment magnitude |
| MOF | - | Seismometer station in the Vosges Mountains (France) |
| MPa | - | $10^6$ Pascal |
| MSK | - | Medvedev-Spohnheuer-Karnik intensity scale |
| $\mathbf{n}$ | - | Unit vector |
| N | - | North |
| Nm | - | Newton $\cdot$ meter |
| $nx$ | - | Number of grid points in simulation (x-direction) |
| $ny$ | - | Number of grid points in simulation (y-direction) |
| $nz$ | - | Number of grid points in simulation (z-direction) |
| $nxr$ | - | Number of grid points in rupture plane (x-direction) |
| $nyr$ | - | Number of grid points in rupture plane (y-direction) |
| $nxs$ | - | Hypocenter coordinates (x-direction) |
| $nys$ | - | Hypocenter coordinates (y-direction) |
| PD | - | Peak displacement |
| PGV | - | Peak ground velocity |
| PHV | - | Peak horizontal velocity |
| PV | - | Peak velocity |
| PVV | - | Peak vertical velocity |
| $Q_P$ | - | Quality factor for compressional waves |
| $Q_S$ | - | Quality factor for shear waves |
| $r$ | - | Distance dependent parameters used in chapter 3, equation 3.1 |
| $R$ | - | Hypocentral distance |
| $R_{AR}$ | - | Ratio of $Y_{FD1}$ and $Y_{AR}$ |
| $R_{FD}$ | - | Ratio of $Y_{FD1}$ and $Y_{FD2}$ |
| $RD$ | - | Ratio of dynamic and kinematic peak displacement |
| $RV$ | - | Ratio of dynamic and kinematic peak velocity |

| | | |
|---|---|---|
| ReNaSS | - | Réseau National de Surveillance Sismique |
| s | - | Seconds |
| S | - | South |
| $S_{FD}$ | - | Seismogram computed using the FD method |
| $S_l$ | - | Line source velocity seismograms |
| $S_p$ | - | Point source velocity seismograms |
| $S_{REFL}$ | - | Seismogram computed using the reflectivity method |
| $t$ | - | Time |
| $\mathbf{u}$ | - | Vector of ground displacement |
| UBC | - | Uniform building code |
| UHS | - | Uniform halfspace |
| USA | - | United States of America |
| UT | - | Universal time |
| $\mathbf{v}$ | - | Vector of ground velocity |
| $V$ | - | Modeling volume |
| $v_a$ | - | Regression coefficient used in chapter 3, equation 3.1 |
| $v_{\max}$ | - | Maximum wave velocity |
| $v_{\min}$ | - | Minimum wave velocity |
| $v_p$ | - | Compressional wave velocity |
| $v_R$ | - | Rupture velocity |
| $v_s$ | - | Shear wave velocity |
| $v_{s30}$ | - | Shear wave velocity in upper 30 meters |
| $V_c$ | - | Slip rate weakening distance |
| W | - | West |
| $\mathbf{x}$ | - | Coordinates of a grid point |
| $Y$ | - | Averaged horizontal spectral acceleration |
| $Y_{FD1}$ | - | $Y$ computed using the FD method for the DSB model |
| $Y_{FD2}$ | - | $Y$ computed using the FD method for a homogeneous model |
| $Y_{AR}$ | - | $Y$ computed using an attenuation relation |
| | | |
| $\delta_{ij}$ | - | Kronecker delta function |
| $\epsilon_{ij}$ | - | Elements of the strain tensor |
| $\theta$ | - | Dip angle |
| $\lambda$ | - | First Lamé parameter |
| $\Lambda$ | - | Rake angle |
| $\mu$ | - | Second Lamé parameter, shear modulus |

$\mu_d$ - Dynamic friction coefficient
$\mu_s$ - Static friction coefficient
$\phi$ - Strike angle
$\rho$ - Density of a medium
$\sigma$ - Standard deviation
$\sigma_0$ - Scalar initial stress
$\sigma_e$ - Scalar elastic stress
$\sigma_{ij}$ - Element of the stress tensor
$\sigma_n$ - Stress component normal to the fault plane
$\sigma_y$ - Scalar yield stress
$\tau_r$ - Rise time

# Introduction

In recent years Finite Difference (FD) methods have become a powerful tool for forward modeling the seismic wavefield of earthquakes (e.g. [52, 71, 88, 103, 134]. Applications include a large range of scales. Effects of local extend are treated in the modeling of wave-propagation in narrow fault zones [63, 66, 124] or in volcanic structures [92]. Regional effects are studied when investigating basin structures [49, 104, 106, 118], simulating large past events [89, 93, 111] or scenario earthquakes [59, 105]. Large-scale wave-propagation could be successfully modeled in the lower crust [73], the upper mantle [132] and in global earth models [64, 65]. In these above mentioned studies, the simulation of seismic waves has been used to answer a variety of different questions: Seismic wave-propagation is modeled in order to better understand effects the seismic source process, focusing and defocussing or seismic scattering, to evaluate existing subsurface models, or to illuminate the process of wave-propagation in complex earth models. For frequencies below 1-1.5 Hz, the FD method allows the prediction of ground motion with very good accuracy if the geological model is accurate to this scale.

A promising application for FD simulations is the field of seismic hazard assessment. When the seismic hazard of an earthquake-prone region is quantified, buildings can be constructed accordingly, and the number of casualities and fatalities can be greatly reduced in future large earthquakes. The increased public and scientific interest in the estimation of seismic hazard paved the way for a rapid development of the field. This is reflected in a growing number of publications (e.g. [15, 18, 20, 25, 34, 35, 39, 53, 90, 110, 139]). Generally, the efforts can be divided into two approaches: Applying the deterministic approach, strong ground motion is predicted for every point of the surface based on ground motion measurements from recent events. Interpolation of ground motion amplitudes is provided by radial attenuation laws [3, 6, 21, 22, 68, 117]. Using the deterministic approach, the areal ground motion distribution can also be computed using wave-simulation techniques such as the FD method. The probabilistic approach computes the probability of exceedance of a

certain ground motion intensity level at a given site in a given period of time. The results of this method are compiled in hazard maps for many regions of the world [40, 91, 125, 126].

However, there are still shortcomings in the procedure of hazard estimation. One of the main problems is that source physics is not taken into account when the seismic hazard of a region is estimated. The extension and the orientation of a fault, as well as the dynamics of the rupture process lead to a large variability of earthquake ground motion close to the fault [45] and to significant deviations from radial ground motion attenuation relations. Another important factor affecting ground motion amplitudes generally not included in seismic hazard assessment is the local subsurface geological structure. Any deviation from homogeneous distributions of elastic subsurface parameters can enhance ground motion amplitudes due to focusing of seismic waves [49, 104, 106, 118] or trapping of seismic energy in wave-guides [63, 66, 92, 124, 140].

The purpose of this work is to quantify the above mentioned effects in order to include the insights in future seismic hazard estimations. This goal is addressed by 2D and 3D ground motion modeling using a fourth-order staggered-grid FD method [103, 109]. Different aspects of the issue are illuminated by three case studies in chapters 2 – 4.

The first case study (chapter 2) investigates the usefulness of a current first-order geological subsurface model for high-frequency (1 Hz $\leq$ f $\leq$ 8 Hz) simulations. This is done by 2D modeling wave-propagation for three magnitude $M_L = 3.5 - 3.6$ earthquakes that occured in the Rhinegraben (Germany) in 1996 and 1997. A comparison between data and synthetics for the three events shows that basic features of the wavefield can be simulated in many but not all cases, thus leading to the conclusion that a refinement of the geological model is necessary before reliable high-frequency predictions can be made for the Rhinegraben.

Wave-propagation of a magnitude $M_L = 6.2$ earthquake is simulated in chapter 3. The earthquake occured in 1927 at the edge of the Dead Sea Basin close to the city of Jericho, Israel. Wave-propagation towards the north is anomalously efficient for earthquakes being located close to the Basin. Up to now the building code of Israel does not include this deviation from radially decaying amplitudes which goes along with an underestimation of the seismic hazard of the region. The simulations in chapter 3 point out possible explanations for the large wave amplitudes in the north of the Dead Sea Basin including both, source physics and particularly the basin substructure. The results show that the geological subsurface structure of the

Dead Sea Basin plays a crucial role for ground motion amplitudes and has to be considered when the hazard of the region is estimated.
Ground motion from earthquakes on dipping faults is investigated in chapter 4. Faults dipping at angles $\theta \neq 90°$ show increased values of ground motion on the hanging wall relative to the median for this distance range. The modeling in chapter 4 gives insight into the ground motion at the surface, in vertical cross-sections through the model, and into stress distributions on the fault plane. The increased ground motion on the hanging wall can be explained by the interaction of normal-stresses with the free-surface. These effects are only included in dynamic FD simulations. In chapter 4 differences in ground motion from dynamic and prescribed ruptures are discussed so that the results can be included in conventional (prescribed) ground motion estimates for hazard assessment.
The three case studies are preceded by a short introduction to the concepts of Finite Difference modeling (chapter 1). Starting from the three-dimensional wave-equation, the basics of FD modeling are derived. Terms commonly used in the context of FD modeling are explained, and difficulties and possible problems that might occur in FD schemes are pointed out. A major part of the chapter is devoted to the numerical insertion of the earthquake source into the Finite Difference scheme. Following the structure of this thesis the insertion of a kinematic source is explained first, moving from a simple point source (as used in the simulations in chapter 2) to the implementation of an extended vertical fault plane (used in chapter 3). The chapter is completed by a presentation of the concept of dynamic ruptures (made use of in chapter 4) and its numerical implementation into the FD scheme.
The appendix deals with the problem of the free-surface location in a staggered-grid scheme. There are two possible locations for the free surface, one being co-located with the normal stresses, and the other one half a grid point apart vertically. By comparsion of seismograms to a reflectivity solution, the accuracy of the two implementations is studied. This result is of great interest for the development of Finite-Difference methods in general due to the fact that staggered grid schemes with both implementations are commonly and equally used. In the appendix it is shown that the implementation located half a grid points apart vertically from the normal stresses gives more accurate results. For all simulations in this thesis, the free surface is therefore implemented at this location.

# Chapter 1

# Concepts of Finite Difference Modeling

The most fundamental equation underlying the theory of seismology is the equation of motion which describes the propagation of waves radiated from earthquakes sources and relates forces in the medium to measurable ground motion [4, 75]. In its most general form and for an inhomogeneous anisotropic medium it can be written as

$$\rho \ddot{u}_i = \frac{\partial \sigma_{ij}}{\partial x_j} + f_i, \tag{1.1}$$

where $\rho$ is the density of the material, $\ddot{u}_i$ denotes the second derivative of the three elements of the ground displacement vector $\mathbf{u}$ with respect to time, $\sigma_{ij}$ is the ijth component of the stress tensor and $f_i$ denote the components of the body forces. The indices $i$ and $j$ stand for the spatial directions.
In an earthquake almost all Earth materials show a linear proportionality between stress $\sigma_{ij}$ and strain $\epsilon_{kl}$. For a linear elastic medium, the empirical relationship between stress and strain is known as Hooke's law. In case of general isotropy only two elastic moduli are needed to describe the proportionality. A common representation is done using Lamé parameters $\lambda$ and $\mu$ which are material dependent and may vary with location:

$$\sigma_{ij} = \lambda \epsilon_{kk} \delta_{ij} + 2\mu \epsilon_{ij}. \tag{1.2}$$

$\delta_{ij}$ indicates the Kronecker delta function, and the indices $i$, $j$, and $k$ stand for the three spatial directions.

Using this simplified formulation of Hooke's law, and a relationship between strain and displacement

$$\epsilon_{ij} = \frac{1}{2}\left(\frac{\partial u_i}{\partial x_j} + \frac{\partial u_j}{\partial x_i}\right) \tag{1.3}$$

valid for infinitesimal strain,
Combinig equations 1.1 – 1.3 yields the wave-equation for an inhomogeneous isotropic medium:

$$\rho\ddot{u}_i = (\lambda + \mu)u_{j,ij} + \mu u_{i,jj} + \lambda_{,i}u_{j,j} + \mu_{,j}(u_{i,j} + u_{j,i}) + f_i \tag{1.4}$$

This equation can be rewritten as a system of second order partial differential equations. A common representation for Finite Difference applications is the velocity-stress formulation [78, 134, 135] which is also used by the Finite Difference method throughout this thesis. There are several advantages of this formulation over the formulation expressed in displacements (e.g. [74]). The scheme is stable for all values of Poisson's ratio, grid dispersion and grid anisotropy are small, both, surface and buried sources can easily be implemented, and the free-surface boundary condition is easily satisfied [76]. The equations of motions are given by

$$\rho\frac{\partial v_x}{\partial t} = \frac{\partial \sigma_{xx}}{\partial x} + \frac{\partial \sigma_{xy}}{\partial y} + \frac{\partial \sigma_{xz}}{\partial z} + f_x, \tag{1.5}$$

$$\rho\frac{\partial v_y}{\partial t} = \frac{\partial \sigma_{xy}}{\partial x} + \frac{\partial \sigma_{yy}}{\partial y} + \frac{\partial \sigma_{yz}}{\partial z} + f_y, \tag{1.6}$$

$$\rho\frac{\partial v_z}{\partial t} = \frac{\partial \sigma_{xz}}{\partial x} + \frac{\partial \sigma_{yz}}{\partial y} + \frac{\partial \sigma_{zz}}{\partial z} + f_z, \tag{1.7}$$

where $v_x$, $v_y$, and $v_z$ denote the particle velocity components, $\sigma_{xx}$, $\sigma_{yy}$, and $\sigma_{zz}$ are the normal stresses, and $\sigma_{xy}$, $\sigma_{xy}$, and $\sigma_{yz}$ are the shear stresses. The constitutive laws are then expressed as

$$\frac{\partial \sigma_{xx}}{\partial t} = \lambda\left(\frac{\partial v_x}{\partial x} + \frac{\partial v_y}{\partial y} + \frac{\partial v_z}{\partial z}\right) + 2\mu\frac{\partial v_x}{\partial x}, \tag{1.8}$$

$$\frac{\partial \sigma_{yy}}{\partial t} = \lambda\left(\frac{\partial v_x}{\partial x} + \frac{\partial v_y}{\partial y} + \frac{\partial v_z}{\partial z}\right) + 2\mu\frac{\partial v_y}{\partial y}, \tag{1.9}$$

$$\frac{\partial \sigma_{zz}}{\partial t} = \lambda\left(\frac{\partial v_x}{\partial x} + \frac{\partial v_y}{\partial y} + \frac{\partial v_z}{\partial z}\right) + 2\mu\frac{\partial v_z}{\partial z}, \tag{1.10}$$

$$\frac{\partial \sigma_{xy}}{\partial t} = \mu \left( \frac{\partial v_y}{\partial x} + \frac{\partial v_x}{\partial y} \right), \tag{1.11}$$

$$\frac{\partial \sigma_{xz}}{\partial t} = \mu \left( \frac{\partial v_z}{\partial x} + \frac{\partial v_x}{\partial z} \right), \tag{1.12}$$

$$\frac{\partial \sigma_{yz}}{\partial t} = \mu \left( \frac{\partial v_z}{\partial y} + \frac{\partial v_y}{\partial z} \right). \tag{1.13}$$

In order to solve the equations numerically, in a Finite Difference scheme the modeling volume $V$ is discretized into nx $\cdot$ ny $\cdot$ nz grid points with distance $dx$ to the neighboring grid point. Given a continuous solution of the wave-equation in the volume $V$ the solution at those discrete points can be obtained by indirectly approximating the continuous solution. This is achieved by the approximation of derivatives. Traditionally, Taylor series expansions of the solution in the neighborhood of point $x_i$ are used. Another possibility for obtaining the approximation is by the computation of the tangent line to the function [72, 128]. The discretized form of equations 1.5 – 1.13 can be found in [76].

## 1.1 Stability of a System

A crucial issue for explicit Finite Difference numerical methods is stability. Stability of a system is in practical terms connected to an energy limit and reflects the fact that the total energy in a physical system should not change.
Mathematically this is achieved when the Courant-Friedrichs-Lewy (CFL) stability criterion

$$\frac{dt \cdot v_{\max}}{dx} \leq c \tag{1.14}$$

is met (e.g. [103]), where $v_{\max}$ is the maximum (compressional wave) velocity in the modeling volume $V$, $dx$ is the grid spacing, $dt$ the sampling interval in time, and $c$ some constant number which has to be determined empirically. In this study, for $c$ a value of 0.45 is used [103]. This is a conservative estimate. Other authors suggest to use a slightly larger value of 0.5 (e.g. [71, 119]).

## 1.2 Numerical Dispersion

In a Finite Difference scheme, special attention has to be given to avoid numerical dispersion. Dispersion occurs when the synthetics contain frequencies above a certain frequency limit, $f_{\max}$ which is defined as

$$f_{\max} = \frac{v_{\min}}{g \cdot dx}, \tag{1.15}$$

with $v_{\min}$ the minimum (shear wave) velocity in the modeling volume $V$, the grid spacing $dx$, and a constant $g$ which stands for the number of points per wavelength that will be computed. For 3D simulations the computation of 5 points per wavelength is sufficient in order to avoid numerical dispersion [76] for distances generally considered in Finite Difference simulations.
When the velocity model is kept constant, equation 1.15 displays a proportionality between the maximum frequency included in the simulation $f_{\max}$ and the grid interval $dx$. Thus, for 3D simulations, an increase of $f_{\max}$ by a factor of 2 requires the computation of the wave-equation at $2^3$ as many grid points as before. Additionally, in order to keep the system stable, the number of time steps has to be doubled (see equation 1.14). For that reason, and the limitation of computational power, the frequency content of synthetic seismograms computed with 3D FD methods has so far been restricted to frequencies below 1 – 1.5 Hz, depending on the size of the modeling volume.

## 1.3 Staggered Grids and Accuracy of the System

A common way of arranging Finite Difference schemes is to compute the wavefield components on a staggered grid in both, space and time. This is done in order to increase the accuracy of the computation without increasing the number of points at which equations 1.5 – 1.13 have to be solved [33]. In a spatially staggered grid, some of the components of the velocity and stresses are computed in between the grid nodes. In the Finite Difference scheme used in this thesis, the particle velocities $v_x$ are defined on the grid nodes, while $v_y$ and $v_z$ are defined half a grid point apart in both, x-direction and y- and z-direction, respectively. The normal stresses $\sigma_{xx}$, $\sigma_{yy}$, and $\sigma_{zz}$ are located at the level of the grid points in vertical and x-direction and are shifted for half a grid point in y-direction. The shear stresses $\sigma_{xy}$ are defined half a grid point apart in y-direction, $\sigma_{xz}$ half a grid point apart vertically, and $\sigma_{yz}$ are located in the center of a cell (see figure 1.1). Temporal staggering of the

wavefield parameters is done similarly [78]. For an accuracy of second order in time and fourth order in space the wavefield parameters half a grid point and 3/2 grid points apart from the pivot point are needed for an update [76].

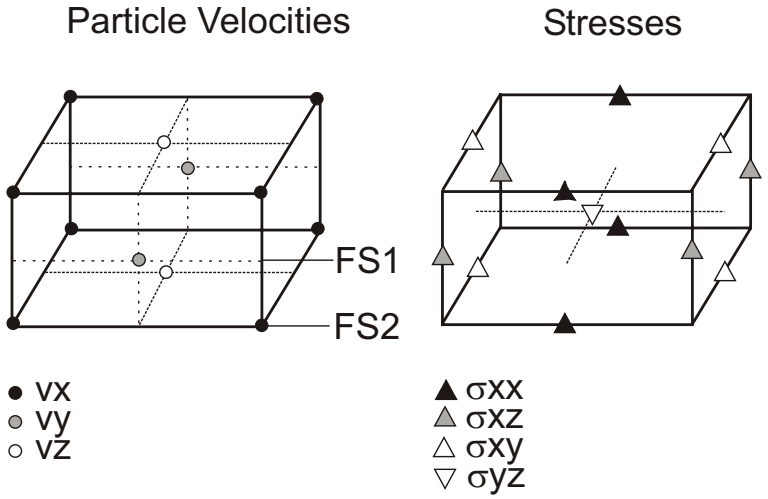


Figure 1.1: *Staggering of the wavefield parameters.*

## 1.4 Lateral and Bottom Boundaries

A further difficulty arises in Finite Difference simulations when the waves reach the boundaries of the modeling volume $V$ since the boundaries act as reflectors. In order to suppress these unwanted reflections, at the lateral and bottom edges an explicit boundary-condition is applied [27]. In the boundary region, the wave-equation is replaced by a one-way wave-equation which does not permit energy to propagate from the boundaries back into the numerical grid. This approach is successful for events that impinge on the boundaries at steep angles. Its effectiveness, however, degrades for waves with shallow incidence angles. To further limit reflections from the boundaries, the interior grid is surrounded with another, larger grid, that consists of attenuative material (figure 1.2) [26]. The attenuation in this region has to be chosen carefully, since a value too low attenuates the amplitude too little while very strong attenuation might produce reflections at the boundary between the interior to the exterior grid.

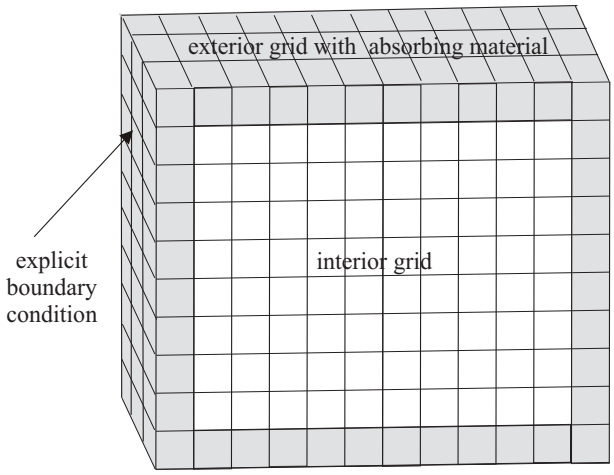


Figure 1.2: *Prevention of artificial reflections by an exterior grid and an explicit boundary-condition.*

## 1.5 Free-Surface Boundary-Condition

The numerical treatment of the free surface in Finite Difference methods has received considerable attention in the literature. The majority of these publications are concerned with the treatment of irregular free surfaces, in order to simulate the effects of topographic scattering [60, 100, 105, 113]. For those so called vacuum methods a layer where all elastic parameters are equal to zero is introduced. This method is used in chapter 4 where ground motion from earthquakes on dipping faults is simulated. While this method allows the flexibility of computing models with dipping faults or including mountain topography, it also generally requires a relative dense sampling of the wavefield, e.g. 25 points per wavelength for stable and accurate results [100]. In the cases where effects of surface relief are expected to be negligible, e.g. for long-period waves propagating in areas of smooth topography, it is possible to formulate an explicit boundary-condition valid for a planar surface [51, 76]. This explicit free-surface boundary-condition is used for the simulations in chapters 2, 3, and in the appendix. The advantage of this formulation is generally that it requires less points per wavelengths (e.g. 5 points per wavelength [76]) compared with the formulation for irregular free surfaces. Clearly, the explicit free-surface condition should be considered for numerical reasons in situations where applicable.

There are two different possibilities for the implementation of the explicit free-surface boundary-condition in the staggered grid, half a grid point apart vertically. Both

are discussed in the appendix. In this study the free-surface boundary-condition is co-located with the shear stresses $\sigma_{xz}$ and $\sigma_{yz}$ which was found to be superior to the co-location with the normal stresses $\sigma_{xx}$, $\sigma_{yy}$, and $\sigma_{zz}$, and the shear stress $\sigma_{xy}$ [42].

## 1.6 Implementation of the Source

While rupture propagation is based on the same principle in every Finite Difference scheme, for the implementation of the source two fundamentally different approaches exist. Most Finite Difference schemes compute the ground shaking on the basis of a kinematic definition of the source [47, 48, 49, 52, 71, 103, 136]. In those cases the rupture is prescribed and can not develop dynamically. This approach is useful for point sources where the interaction of rupture and structure is negligible, and for both, vertical dipping faults, or faults buried 5 kilometers or deeper, since in those cases the dynamic interaction of stresses on the fault with the free surface is marginal [43]. The implementation of kinematic ruptures is described in section 1.6.1. Section 1.6.2 is devoted to the implementation of dynamic ruptures.

### 1.6.1 Kinematic Ruptures

The kinematic (prescribed) source is implemented in the Finite Difference grid by adding

$$-dt \cdot \frac{\dot{M}_{ij}}{dx^3} \tag{1.16}$$

to $\sigma_{ij}(t)$, where $dt$ is the time sampling interval, $\dot{M}_{ij}$ is the $ij$th component of the moment rate tensor for the earthquake, $dx^3$ is the cell volume, and $\sigma_{ij}(t)$ is the $ij$th component of the stress tensor on the fault at time $t$.
The components of the moment tensor are computed from the shear modulus $\mu$, the area of a cell $dx^3$, the elements of the normal to the plane $n_i$ and $n_j$, and the elements of the slip vector $\mathbf{D}$ which in the following equation is expressed by the absolute slip value $|\mathbf{D}| = D$ averaged over one cell and the unit vectors in the direction of the slip, $d_i$ and $d_j$. The moment tensor on the fault plane is given by

$$M_{ij} = \mu \cdot dx^2 \cdot D\,(d_i n_j + d_j n_i). \tag{1.17}$$

The normal to the fault plane is expressed by the strike angle with respect to north, $\phi$, and the dip angle of the fault plane, $\theta$, which is measured from the horizontal.

The slip on the fault plane is given by the rake angle $\Lambda$ measured from the strike direction. The slip vector computes then to

$$\mathbf{D} = D\cos\Lambda \begin{pmatrix} \cos\phi \\ \sin\phi \\ 0 \end{pmatrix} - D\sin\Lambda \begin{pmatrix} -\sin\phi\cos\theta \\ \cos\phi\cos\theta \\ \sin\theta \end{pmatrix}, \tag{1.18}$$

where the slip is a function of time $t$. The function is constrained by the rise time $\tau_r$ after which the peak slip value is reached. The rise time is computed by a scaling relation from the magnitude of the event [58]. The shape of the sliprate function has also to be predefined. Typical sliprates are gaussian shaped, triangular, or half-cosines.

In 3D simulations (chapters 3 – 4 and appendix) the implementation of the source is straightforward since the possible orientations of the fault plane and thus the values taken by the angles $\phi$, $\theta$ and $\Lambda$ can easily be mapped onto the three-dimensional grid. The three-dimensional seismic moment tensor contains nine elements $M_{ij}$ with i,j = x,y,z. In 2D simulations as carried out in chapter 2, the moment tensor contains only four elements with i,j = x,z. In order to simulate the horizontal (radial) component correctly, the strike angle $\phi$ given by the fault plane solution has to be considered with respect to the orientation of the profile on which the seismic waves are simulated. The approximated double-couple point sources translate in 2D simulations to line sources. Therefore, the seismograms need to be corrected for this effect after the simulations. The synthetic line source seismograms $S_l$ are transformed into point source velocity seismograms $S_p$ by the following equation:

$$S_p(t) = \frac{1}{\sqrt{R}} \frac{d}{dt} \left( \frac{1}{\sqrt{t}} * S_l(t) \right), \tag{1.19}$$

where $R$ is the distance from the source to the receiver, $t$ is the time, and $*$ denotes a convolution in time [133]. This correction is applied to all of the 2D synthetics shown in chapter 2.

### Point Source

The size of the rupture area scales with the magnitude of an event. A large number of scaling relations are available for different source mechanisms and earthquake regions [19, 70, 114, 115, 120, 121, 122, 137, 138]. It is in accordance with all those authors, that for small earthquakes (i.e. $M_L < 4.0$) the rupture planes are small enough (e.g. a few hundred meters) that rupture dynamic effects are not resolvable

at the frequencies considered in the simulations. In those cases, the grid spacing interval $dx$ can be chosen in a way that the squared interval $dx^2$ is in the order of the size of the fault plane. Those earthquakes are therefore modeled as point sources and the source is added to one grid point only.
For the simulation of the Rhinegraben earthquakes ($M_L$ = 3.5 – 3.6) in chapter 2 this is the case. The grid spacing interval in those simulations amounts to 50 m.
The accuracy study described in the appendix also uses point sources for the 3D simulations in order to keep the model as simple as possible. That way, differences in ground motion between the two implementations of the free-surface conditions are not affected by rupture dynamics but are only due to the different locations of the free surface.

**Extended Source**

For moderate and large events (i.e. $M_L \geq 4.0$), rupture dynamics plays a crucial role within the frequency range considered in the simulations. Thus, the finite size of the fault plane has to be taken into account. This is done by defining a rupture area of nxr · nyr grid points. The rupture is initiated at the hypocenter (nxs,nys), one of the grid points of the rupture plane, from where it propagates with variable rupture velocity $v_r$ to each of the grid points on the fault area that break successively. In this case, the sliprate function $\dot{D}(t)$ needs to be defined at every grid point on the rupture area [88]. Examples of ground motion from earthquakes with finite rupture are shown in chapter 3 and 4. For the Jericho earthquake ($M_L$ = 6.2) analyzed in chapter 3, a constant sliprate function was used at every grid point. The kinematic ruptures simulated in chapter 4 use a variable sliprate that is equivalent to the sliprate computed from dynamic simulations for a fault buried 5 km deep.
Extended rupture planes that lie vertically within the modeling volume (corresponding to a dip of 90°) are straightforward to implement since the fault plane coincides with the grid points (e.g. in chapter 3). Further considerations have to be taken into account for faults with dipping angles $\theta \neq 90°$. The simulations in chapter 4 are computed on faults with dip angles $\theta = 30°$, $\theta = 45°$, and $\theta = 60°$. In order to avoid numerical errors due to averaging procedures, the numerical grid is kept parallel to the fault plane (figure 1.3). The free surface is then rotated for an angle $\pi/2 - \theta$ with respect to the numerical grid. Above the free surface a vacuum-layer is introduced. As explained above (section 1.5), due to the step-like free surface and in order to keep the system stable, the grid sampling needs to be finer than for flat free surfaces where an explicit free-surface boundary-condition can be applied.

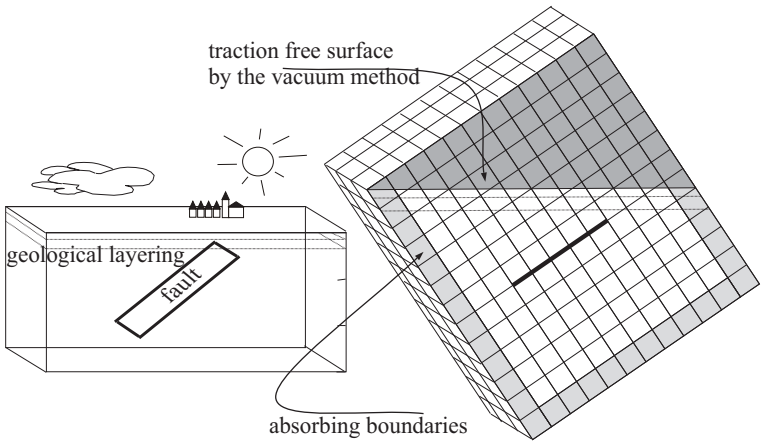


Figure 1.3: *Location of a dipping fault in a geological model (left) and mapping of dipping faults onto the numerical grid (after [93]). In the right image, the fault plane is indicated as a fat line. The dark grey squares represent the area above the free surface. The light grey shading displays the area covered by the absorbing boundaries.*

### 1.6.2 Dynamic Ruptures

In reality, the process of rupture is not predefined but develops due to the complex interaction of stresses, traction and slip on the fault plane. The assumption, that traction and slip are related by a friction law across the fault zone is used by dynamic rupture models. Dynamic rupture simulation has become increasingly popular for the simulation of earthquakes on dipping faults [83, 93, 107, 111] and considerable differences are found between kinematic and dynamic rupture simulations for dip angles $\theta \neq 90°$ [43]. In chapter 4, ground motion from dynamic ruptures is computed and analyzed in comparison to kinematic rupture models. For the dynamic implementation, an algorithm inspired by Madariaga et al. [80] and further developed by Nielsen and Olsen [93] is used. Both friction and dislocation are co-located on the same grid points, exactly on the fault surface [93]. Using Betti's Theorem [4], the total stress $\sigma(\mathbf{x}, t)$ on the fault can be written as a function of the local slip velocity $\dot{D}$, the long range elastic stress $\sigma_e$ and two material properties $\mu$ and $v_s$. The dynamic condition on the fault plane can then be expressed as

$$\sigma(\mathbf{x}, t) = \frac{\mu}{2v_s}\dot{D}(\mathbf{x}, t) + \sigma_e(\mathbf{x}, t) + \sigma_0(\mathbf{x}, t_0), \tag{1.20}$$

where $\mu$ and $v_s$ denote the shear modulus and the shear wave velocity, and $\sigma_0$ is the initial stress distribution on the fault at the time $t_0$ the fracture starts [94]. The long range stress $\sigma_e$ combines all non local contributions to the stress that results

from slip occuring at any segment of the fault at time $t$. No analytical form of $\sigma_e$ is known for an inhomogeneous medium, and in the method this term is computed numerically by the Finite Difference scheme and then substituted into expression (1.20). In the static case, when no slip occurs at any part of the fault, equation 1.20 reduces to

$$\sigma(\mathbf{x}) = \sigma_0(\mathbf{x}, t_0). \tag{1.21}$$

Rupture starts when $\sigma$ exceeds the yield stress $\sigma_y$ and the contribution of static friction expressed by the static friction coefficient $\mu_s$ and the stress component normal to the fault plane $\sigma_n$:

$$\sigma(\mathbf{x}, t) \geq \sigma_y(\mathbf{x}) + \mu_s \sigma_n(\mathbf{x}, t). \tag{1.22}$$

It heals when the shear traction on the fault becomes larger than the radiated stress ($\sigma > \sigma_e$ in equation 1.20).
When the fault is slipping the classical Coulombian model where the friction drops suddenly when the rupture starts and the stress $\sigma$ on the fault is expressed by a dynamic friction coefficient $\mu_d$ as

$$\sigma(\mathbf{x}, t) = \mu_d \sigma_n(\mathbf{x}, t) \tag{1.23}$$

leads for seismological applications to an impasse because of infinite stress singularities and other physical problems [83]. Experience tells that near the rupture front the finite energy release rate needs to be defined by introducing a length scale. Today, two different approaches of friction laws are in use. A simple slip weakening law was proposed by Ohnaka and Shen [101, 102] which makes use of the slip weakening distance $D_c$. Laboratory studies [31, 32, 116] proposed a rate- and state-dependent friction law which was introduced in dynamic rupture modeling for plane 2D ruptures [10, 11, 62] and for 3D fault models [29]. For the dynamic simulations computed in chapter 4, the second approach is applied. When slipping occurs the stress on the fault can be expressed by

$$\sigma(\mathbf{x}, t) = \mu_d \sigma_n + (\sigma_y + \mu_s \sigma_n) \operatorname{Max} \left[ \frac{1}{1 + \dot{D}/D_c} \, , \, \frac{1}{1 + \dot{D}/V_c} \right], \tag{1.24}$$

where $\sigma_y$, $\sigma_n$, $D_c$ and $V_c$ represent the yield stress (in the absence of normal stress perturbations), the stress normal to the fault (in excess of the lithostatic stress), the slip weakening distance, and the rate weakening distance, respectively. When either

the slip weakening distance $D_c$ or the rate weakening distance $V_c$ become very small, the corresponding expression in the square brackets goes to zero, and the rupture is dominated by the remaining parameter, $V_c$ or $D_c$, respectively. In case that both, slip and rate weakening distance become infinitely small, equation 1.24 reduces to the static case (equation 1.21). For the simulations in chapter 4, the static and the dynamic friction coefficients take the values $\mu_s = 0.7$ and $\mu_d = 0.3$, respectively [93, 97].

The computations presented in this thesis have been carried out on an SGI Origin 3200 (Geophysical Institute, Karlsruhe University) using 6 processors. The Finite Difference method used throughout this thesis is based on the work by K.B. Olsen [103, 109].

# Chapter 2

# Case Study I: Modeling Earthquakes in the Rhinegraben

## 2.1 Motivation

The Rhinegraben belongs to the seismically most active regions in Germany. Today the seismicity is characterized by small to moderate crustal events. Larger events occured in the past (e.g. in the year 1356 close to the city of Basel, Switzerland) and are likely to happen again [25]. The Upper Rhinegraben, situated close to the border with France and Switzerland hosts significant traffic routes. The fact that the river Rhine is a major waterway in Europe has led to the development of a highly industrialized region which has on average a population density of more than 300 inhabitants per $km^2$ (for comparison: USA: 15, California: 73.5, Western Europe: 102). The high vulnerability of the region in combination with the moderate seismic activity leads to a seismic risk which is not negligible.
A common way to study seismic hazard is to analyze seismograms for the largest possible event in the region. This analysis is generally done in the time- and in the frequency-domain and comprises for example the estimation of peak ground motion or the computation of response spectral values from the data. The method requires digital seismogram recordings of the largest event.
In interplate seismic regions (e.g. at the North Anatolian Fault (Turkey) or at the San Andreas Fault, USA) the recurrence interval of large earthquakes is generally shorter than in intraplate regimes as in the Rhinegraben where it can amount up to several thousand years. In the latter, digital data of the largest event is therefore often not available. Finite Difference methods provide a powerful tool for the synthetic computation of the wavefield for those large events. So far, the computational power

and the limited knowledge of the subsurface structures has restricted the simulations to frequencies below 1 – 1.5 Hz, depending on the size of the modeling volume and the constraints on the model of elastic parameters. For hazard assessment in the Rhinegraben the wavefield needs to be known up to frequencies around 8 Hz, because the frequency range from 1 – 8 Hz covers the eigenfrequencies of most buildings in the region. While the drawback of limited computational power will presumably be solved in the near future it would require expensive high-resolution experiments to resolve the 3D geological structures precisely enough in order to simulate correct waveforms up to 8 Hz. The exact wiggle-by-wiggle simulation of time-histories including these frequencies requires subsurface models containing all features down to the scale of one wavelength (e.g. 250 m in the simulations in this study). However, when assessing the seismic hazard of a region, it is sufficient to know peak amplitudes of the ground motion or response values at certain frequencies while the knwoledge of the exact waveforms is not necessary.
The purpose of this study is to find out how well peak amplitudes of ground motion, P/S amplitude ratios, arrival times, the duration of shaking, and spectral values of displacement, velocity, and acceleration can be reproduced in the frequency band from 1 to 8 Hz with a first-order velocity and density model available for the Rhinegraben. This is done by the 2D simulation of three $M_L$ 3.5 – 3.6 earthquakes that occured in the Rhinegraben in 1996 and 1997, followed by a comparison of the synthetic time-histories to data recorded at five stations within the Graben, in the Vosges mountains, and the Black Forest. In order to account for differences in amplitudes between simulations in 2D and 3D, an amplitude correction is applied after the simulation [133]. The results will provide guidance for future high-frequency 3D simulations facilitated by massively parallel computers.

## 2.2 Upper Rhinegraben

### 2.2.1 Tectonics and Geology

The Rhinegraben comprises the central and most prominent part of the European Cenozoic Rift System, one of the major tectonic features in western Europe. Its southern part extends almost 300 km from Basel to Frankfurt and is, on average, 30 – 40 km wide. Subsidence of the Rhinegraben began in the Upper Eocene in the southern part of the graben and was interrupted by a broad uplift in the Mid-Miocene [55] due to mass movements in the Alpine region. Today, subsidence is only

found in the northern part of the Rhinegraben. On its eastern and western side the Upper Rhinegraben is flanked by the Black Forest and the Vosges Mountains.

### 2.2.2 Seismicity

Today the seismicity in the area is characterized by small to moderate crustal activity. The largest event that is known to have taken place in the Rhinegraben was the Basel earthquake in 1356 which caused a large amount of damage in the town and the surroundings [86]. The maximum intensity of this event is determined to X corresponding to magnitude $M_L$=6.5 [77]. Paleoseismological investigations have shown several examples of earthquakes of comparable magnitude in the past [87].

### 2.2.3 Three Rhinegraben Earthquakes ($M_L$ 3.5 – 3.6)

In this section I show data from three events that took place in the Upper Rhinegraben during 1996 and 1997 with local magnitudes $M_L$ between 3.5 and 3.6. The data have been recorded by the seismological network of the State Geological Survey (*Landesamt für Geologie, Rohstoffe und Bergbau, Baden-Württemberg*, stations LIBD, FBB and FELD), by one station of the french network ReNaSS (Réseau National de Surveillance Sismique, station MOF), and by one station of the Swiss Seismological Service (station BBS). Stations BBS, FELD, and LIBD are equipped with S-13 velocity transducers, and station FBB consists of a LED-3D, both with a response flat with respect to ground velocity between 1 Hz and 12 Hz. At station MOF the data are recorded with a SS-1 instrument. The data have been bandpass-filtered between 1 and 8 Hz and, except for the data recorded at station FBB, corrected for the transfer function of the corresponding instrument within this frequency band. At station FBB the transfer function is not well known. It is deployed as a strong motion station since it is located in an urban area and is mainly used for demonstration purposes (S. Stange, pers. comm., 1999). Therefore, at station FBB the amplitude is displayed in counts instead of ground velocity. This station can not be used to compare peak velocities of recorded data and synthetics. However, the usefulness of the model for hazard assessment can be verified by a comparison of amplitude ratios between compressional and shear waves, by checking the P-wave arrival times, and by a comparison of the signal duration.
The distance from the hypocenters to the stations ranged between 20 to 60 km. Epicenter and station locations are depicted in figure 2.1, and listed in tables 2.1 and 2.2, respectively [12, 13, 131].

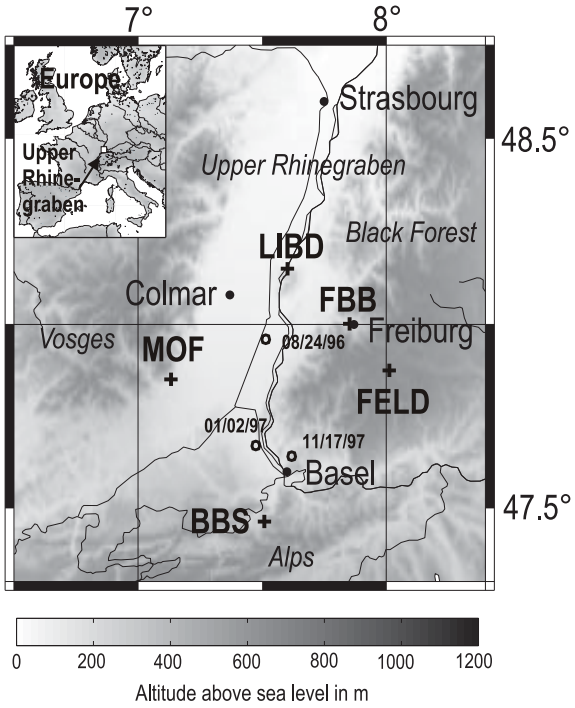


Figure 2.1: *Map of the Upper Rhinegraben showing station (+) and epicenter (∘) locations for the three events analyzed in this study.*

### August 24, 1996, $M_L$=3.5

This event took place close to the village of Dessenheim (France) in the Alsace region. It was the main event of a series of 8 small earthquakes of which the first one occured in July of the same year with a local magnitude of 1.7. The series ended with a magnitude 1.9 event in January 1997. On August 24, two magnitude 2.2 events preceded the main shock. The main event was felt with MSK intensity IV at Müllheim (Germany). Figure 2.2 (left) shows the vertical component of the velocity-seismograms recorded at the five stations.

### February 1, 1997, $M_L$= 3.6

On February 1, 1997, a magnitude 3.6 event occured close to the French village Sierentz, Alsace. This region is known as the source area for an event with local magnitude 4.7 that took place in 1980. The recent event had a MSK intensity of IV, and was felt in Basel, Switzerland and several villages on the German side of the border all the way to the city of Freiburg. The data recorded at the five stations is shown in figure 2.2 (middle).

| **Event** | **1** | **2** | **3** |
|---|---|---|---|
| **Date** | 24 Aug 96 | 01 Feb 97 | 17 Nov 97 |
| **Origin time (UT)** | 23:39:00,7 | 14:01:58,7 | 17:09:22,6 |
| **Magnitude** $M_L$ | 3.5 | 3.6 | 3.5 |
| **Longitude (° E)** | 7.50 | 7.48 | 7.62 |
| **Latitude (° N)** | 47.96 | 47.67 | 47.64 |
| **Hypocentral depth (km)** | $7 \pm 5$ | $10 \pm 3$ | $17 \pm 2$ |
| **Strike (°)** | 116 | 28 | 147 |
| **Dip (°)** | 46 | 63 | 38 |
| **Rake (°)** | 246 | 353 | 257 |

Table 2.1: *Source parameters for the three events used in this study.*

| **Station** | **Longitude** | **Latitude** |
|---|---|---|
| **LIBD** | 7.60 ° E | 48.15 ° N |
| **MOF** | 7.13 ° E | 47.85 ° N |
| **FELD** | 8.00 ° E | 47.88 ° N |
| **BBS** | 7.51 ° E | 47.65 ° N |
| **FBB** | 7.85 ° E | 48.00 ° N |

Table 2.2: *Locations for five seismic stations in the Rhinegraben, the Vosges mountains, and the Black Forest.*

**November 17, 1997, $M_L$= 3.5**

A magnitude 3.5 earthquake occured on November 17, 1997 close to Weil am Rhein (Germany) just a few kilometers from the city of Basel. It was clearly felt up to epicentral distances of 40 km. Individual observations arrived from places more than 100 km away. The source mechanism was determined by the State Geological Survey as a thrust event. Figure 2.2 (right) displays the seismograms for this event.

## 2.3 Modeling Parameters

### 2.3.1 Elastic Model and Geometry

Numerous seismic refraction and reflection profiles through the graben and its adjacent areas such as the Black Forest offer a picture of the geological structure and provide constraints on the P- and S- wave velocities. The 3D compressional wave

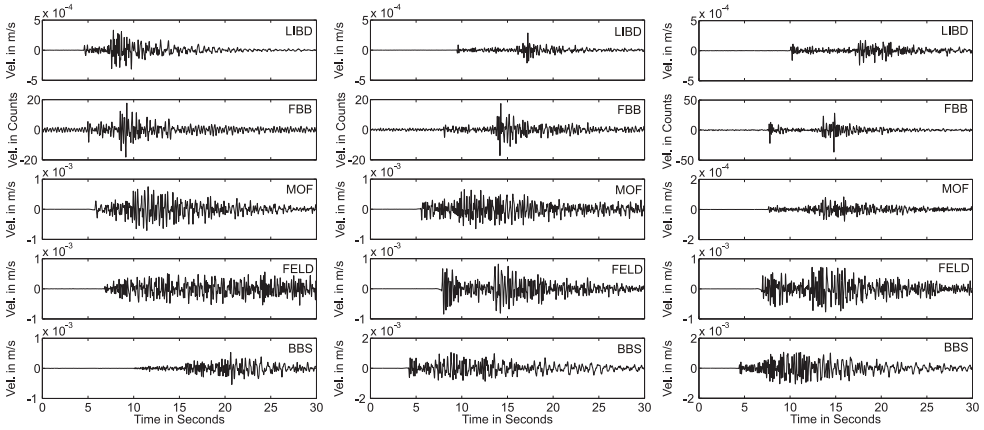


Figure 2.2: *Vertical component velocity seismograms recorded at five stations in the Rhinegraben, the Vosges mountains, and in the Black Forest. From left to right: Seismograms for event 1 on August 24, 1996, seismograms for event 2 on February 1, 1997, and seismograms for event 3 on November 17, 1997. For stations LIBD, MOF, FELD, and BBS the amplitudes are displayed in m/s while the amplitude at station FBB is shown in counts. Time equal to zero seconds corresponds to the origin time of the earthquakes.*

model (figure 2.3) used for the simulations has been constructed compiling 2D cross-sections derived from those experiments: One profile is located almost perpendicular to the strike of the graben at the northern part of the map displayed in figure 2.1, a second profile runs parallel to the strike of the graben through the Black Forest. A third profile crosses profile 2 in the southern part of the Black Forest at an angle of approximately 45 ° from southwest to northeast [61]. Further information provided a 2D velocity model on a line crossing the graben close to Strassbourg [112]. In addition, the 3D model was constrained by two more cross-sections, the first running perpendicular to the strike of the graben, close to the city of Freiburg and a second one parallel to it from north to south [143]. Additionally, maps displaying the depth of the sediment filling, and information on the depth of the Moho [55, 142] have been added to compile the 3D model. The shear wave model has been computed assuming a constant Poisson's ratio of $\nu = 0.25$. The density has been chosen according to the geological interpretation in the above mentioned papers. Minimum and maximum elastic parameters are compiled in table 2.3. The values of the minimum wave velocities indicate that the resolution of the seismic experiments was not able to resolve the velocity structure of the upper few hundred meters. Thus, the simulations can not include scattering of waves in shallow layers which might be responsible for long and high-frequent codas in the data (see figure 2.2).

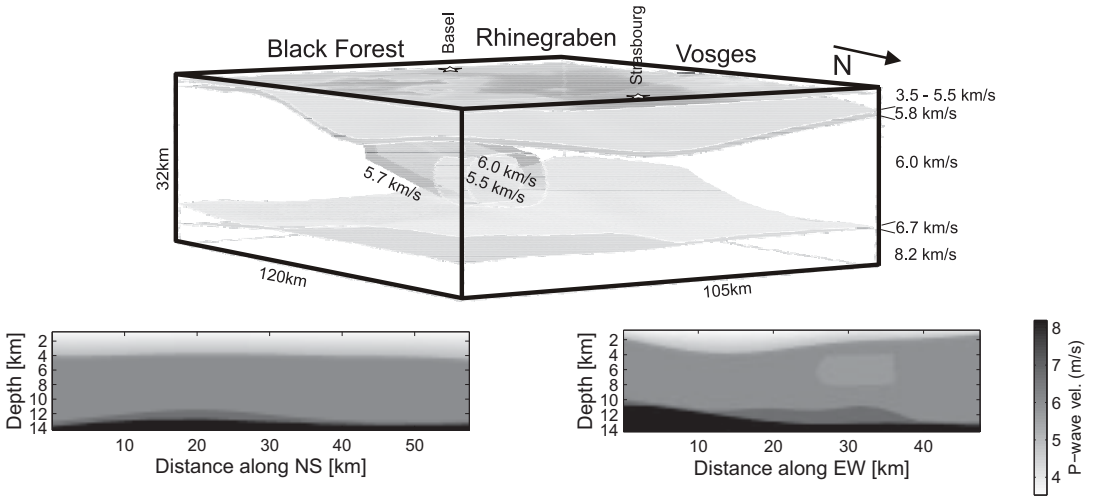


Figure 2.3: *Top: 3D compressional wave model used for the simulations. The model has been compiled using constraints from numerous seismic refraction and reflection profiles, borehole and geological data. Bottom: Two cross-sections through the center of the P-wave model.*

| | |
|---|---|
| Highest P-wave velocity (km/s) | 8.20 |
| Lowest P-wave velocity (km/s) | 3.54 |
| Highest S-wave velocity (km/s) | 4.73 |
| Lowest S-wave velocity (km/s) | 2.04 |
| Highest density (kg/m$^3$) | 2.2 |
| Lowest density (kg/m$^3$) | 3.5 |

Table 2.3: *Minimum and maximum P-wave velocity, S-wave velocity and density values in the 3D model.*

### 2.3.2 Computational Parameters

From the 3D model 2D cross-sections are extracted each connecting two stations with an epicenter. Event 1 from August 24, 1996 is simulated on two profiles. One profile crosses the graben and connects the epicenter with station MOF and station FBB. The second profile runs along the graben from station LIBD in the north via the epicenter to station BBS in the south. Event 2 is simulated on a profile close to the latter one, including station LIBD and station BBS. The third event is simulated on two profiles, of which the first one connects the epicenter with station FBB and station BBS. The second of those profiles extends from station FELD in the Black Forest via the epicenter to station BBS in Switzerland. Further information on the

profiles are compiled in table 2.4.
On each profile 30 seconds of 8 Hz wave-propagation are simulated. A Kostrov source-time function with a rise time of 0.02 seconds [58] was inserted in the 2D models. The seismic moment of 1 $\cdot 10^{14}$ Nm for the $M_L = 3.5$ events and $2.8 \cdot 10^{14}$ Nm for the $M_L = 3.6$ event was computed by the scaling relation [69] assuming that the local magnitudes scale as the moment magnitude [6]. Additional modeling parameters can be found in table 2.5. An amplitude correction (see chapter 1) is applied to the time-histories in order to account for differences between simulations in 2D and 3D [133].

| | **Event** | **Stations** | **Length (km)** |
|---|---|---|---|
| **Profile 1** | 24 Aug 96 | MOF-FBB | 56.85 |
| **Profile 2** | 24 Aug 96 | LIBD-BBS | 82.25 |
| **Profile 3** | 01 Feb 97 | LIBD-BBS | 81.80 |
| **Profile 4** | 17 Nov 97 | FBB-BBS | 69.75 |
| **Profile 5** | 17 Nov 97 | FELD-BBS | 64.95 |

Table 2.4: *Profiles on which 2D wave-propagation simulations have been carried out.*

| | |
|---|---|
| Spatial discretization (m) | 50 |
| Temporal discretization (s) | 0.002 |
| Number of timesteps | 15000 |
| Simulation time (s) | 30 |

Table 2.5: *Geometrical modeling parameters used in the Rhinegraben earthquake simulations.*

## 2.4 Numerical Results

The synthetic velocity seismograms along profile 1 connecting site FBB and site MOF are shown in figure 2.4. In the top subplot the horizontal transverse component, and at the bottom subplot the vertical component are displayed. The scaling of the time-histories is not distant-dependent but constant along the profile. The plot shows distinct P-waves in the vertical component close to the source while the shear wave energy dominates the time-histories on the horizontal component.

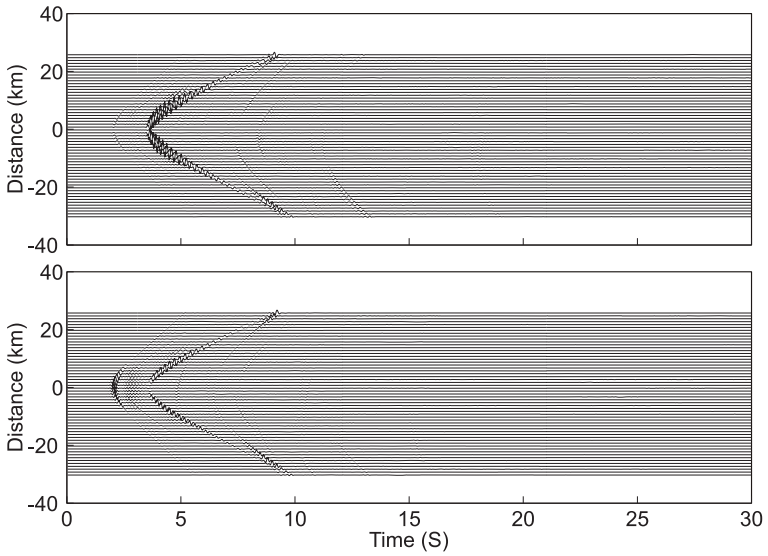


Figure 2.4: *True amplitude representation of the horizontal in-plane (top) and vertical (bottom) component velocity seismograms computed along profile 1 connecting station FBB in the Rhinegraben (top line of the plot) with station MOF in the Vosges mountains (bottom line of the seismograms).*

From the synthetics, the traces corresponding to the Rhinegraben stations are extracted and compared to the data (figures 2.5 – 2.7). In the further analysis I show the comparison of arrival times of P-waves, peak velocities, amplitude ratios between P- and S-waves within different frequency bands, the duration of shaking, and response spectra at selected stations.

### 2.4.1 Arrival Times of P-Waves

A first test of the elastic subsurface model is carried out by checking the P-wave arrival times of the synthetics. Exact arrival times are obtained if the model is right on average while small-scale features do not necessarily have to comply with reality. The arrival times of the first arrivals can be modeled within an accuracy of $\pm$ 0.1 seconds for stations LIBD, BBS and FBB and event 1. At station MOF the synthetic P-wave arrives approximately 0.5 seconds before the recorded P-wave for this event. Larger differences occur for event 2: At both stations, LIBD and BBS, the synthetics arrive approximately one second too late. A similar result is found for event 3. The first onset in the data appears earlier than modeled by the synthetics at all three stations (FBB, FELD, and BBS). The largest overall difference happens to appear

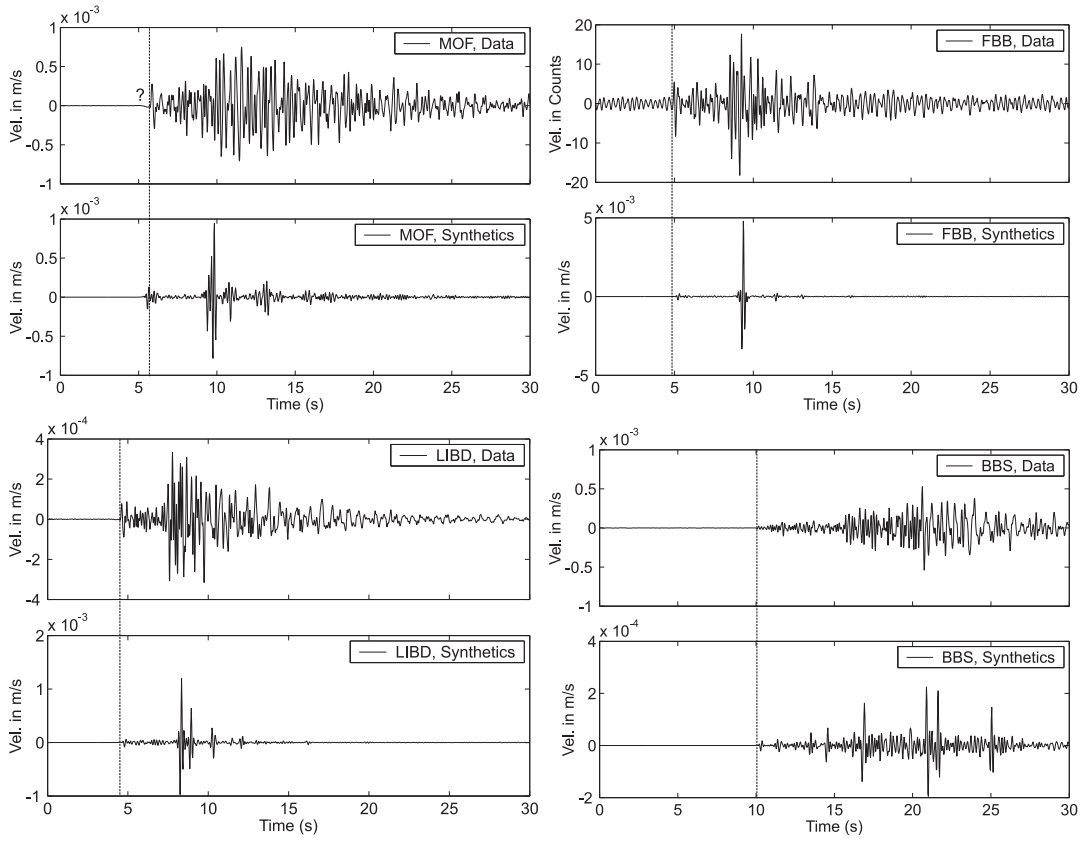


Figure 2.5: *Data and synthetics for a $M_L = 3.5$ earthquake on August 24, 1996 recorded and computed at station MOF (top left), FBB (top right), LIBD (bottom left) and BBS (bottom right). Note that the data at station FBB is displayed in counts while all other seismograms are shown in m/s.*

at station FELD and amounts to 1.2 seconds. Arrival times of the data are indicated as dashed lines in figures 2.5 – 2.7.

### 2.4.2 Peak Ground Velocities

Peak ground velocities for compressional and shear waves (tables 2.6 and 2.7) are determined for all stations. Note that for station FBB the amplitude could only be determined in counts. Peak ground velocities are a good measure for seismic hazard assessment as they correlate with the damage pattern. For the determination of the peak values the maximum amplitude in the wave-train is taken into account.
In some cases, the peak amplitudes of the synthetics match those of the data well. In other cases, however, the agreement between data and synthetics is rather poor:

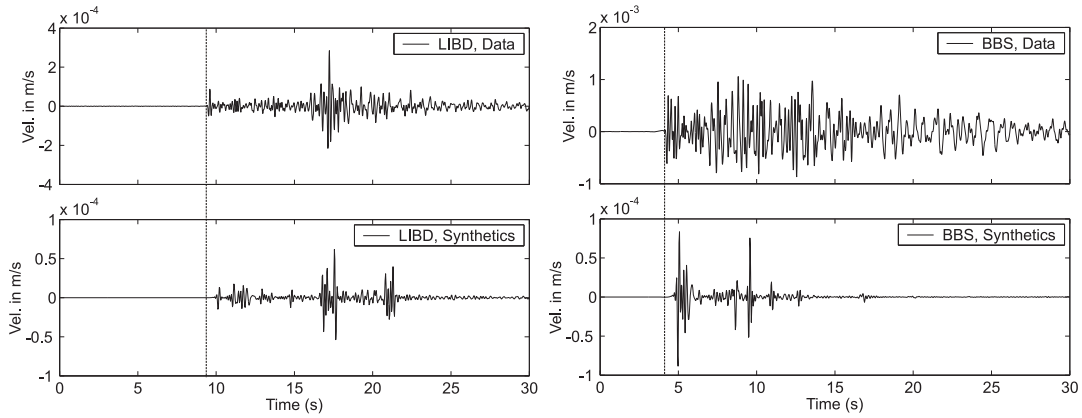


Figure 2.6: *Data and synthetics for a $M_L = 3.6$ earthquake on February 1, 1997 recorded and computed at station LIBD (left) and BBS (right).*

| | **LIBD** | **FBB** | **MOF** | **FELD** | **BBS** |
|---|---|---|---|---|---|
| **Event 1, Data** | $1.0 \cdot 10^{-4}$ | 8.5 counts | $2.9 \cdot 10^{-4}$ | not mod. | $0.5 \cdot 10^{-4}$ |
| **Event 1, Synt.** | $1.0 \cdot 10^{-4}$ | $4.0 \cdot 10^{-4}$ | $2.0 \cdot 10^{-4}$ | not mod. | $0.2 \cdot 10^{-4}$ |
| **Event 2, Data** | $1.2 \cdot 10^{-4}$ | not mod. | not mod. | not mod. | $7.0 \cdot 10^{-4}$ |
| **Event 2, Synt.** | $0.2 \cdot 10^{-4}$ | not mod. | not mod. | not mod. | $0.8 \cdot 10^{-4}$ |
| **Event 3, Data** | not mod. | 22 counts | not mod. | $5.0 \cdot 10^{-4}$ | $4.0 \cdot 10^{-4}$ |
| **Event 3, Synt.** | not mod. | $1.1 \cdot 10^{-4}$ | not mod. | $0.5 \cdot 10^{-4}$ | $4.0 \cdot 10^{-4}$ |

Table 2.6: *Peak ground velocities (m/s) for compressional waves. The values for station FBB are displayed in counts. Only selected event-station pairs have been modeled in this study.*

For event 1 (figure 2.5) the maximum variation amounts to a factor of 2.5 (station BBS) for compressional waves and 3.75 (station LIBD) for shear waves. While the discrepancy in the peak values of the compressional waves at station BBS replicates in the shear waves and could thus be due to a local site effect, the synthetic peak value of the compressional wave at station LIBD matches the peak value of the data precisely. At station MOF the velocities for the compressional waves are underestimated while the peak velocities of the shear waves are overestimated. Both differences are below 50%. The synthetics for event 2 (figure 2.6) generally underestimate the peak values of the data by more than a factor of 4 to a factor of 13. This largest discrepancy occurs at station BBS for the shear wave. Event 3 is simulated at three stations (figure 2.7). A perfect match of the peak values is obtained at station BBS for the compressional wave. The shear wave shows a difference of below 17%

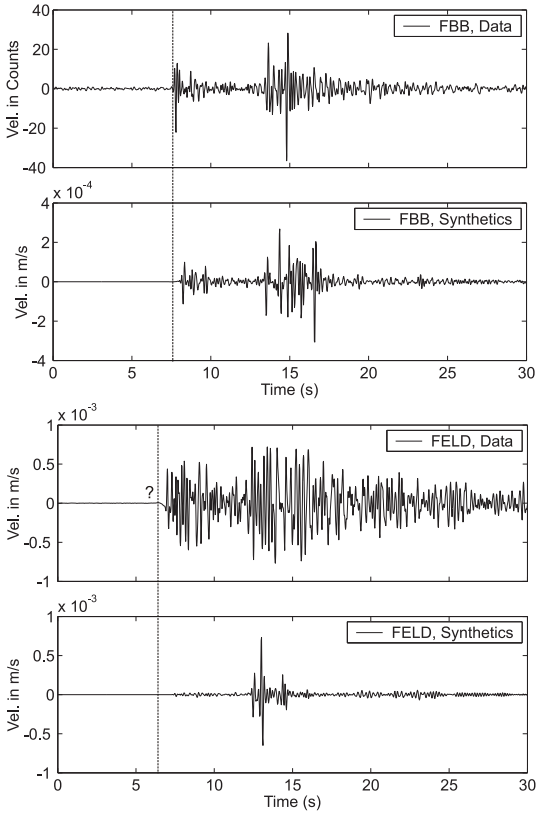


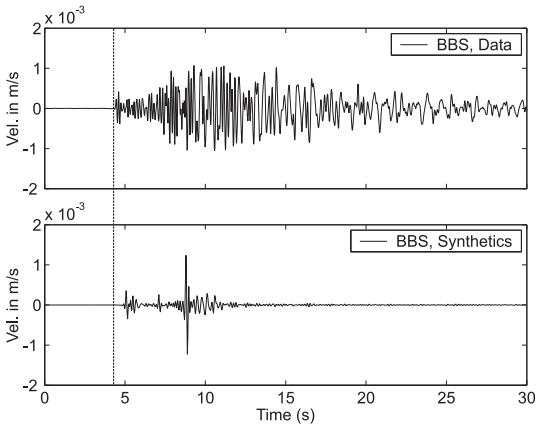


Figure 2.7: *Data and synthetics for a $M_L$ = 3.5 earthquake on November 17, 1997 recorded and computed at station FBB (top left), BBS (top right) and FELD (bottom left). Note that the data at station FBB is displayed in counts while all other seismograms are shown in m/s.*

at this station. At station FELD the compressional wave is underestimated by a factor of 10 by the synthetics while the peak velocities of the shear wave is matched precisely.

I also tested the comparison of peak velocities after the application of different bandpass filters from 1 – 2 Hz, 2 – 4 Hz, and 4 – 8 Hz. The fits could not be improved significantly.

### 2.4.3 Amplitude Ratios

A low degree of agreement in peak ground velocities of data and synthetics could be caused by the fact that local site conditions are missing in the elastic model. In order to test this hypothesis I compare amplitude ratios of P-waves to S-waves. Under the assumption that the site effect is similar for both wave types, P/S amplitude ratios of data and synthetics for the same station and event should give the same values. The amplitude ratios (table 2.8) computed from data and synthetics vary over a wide range and include both, values below 0.1 and values larger than 1. In the latter case the amplitudes of the shear wave are smaller than those of the P-wave.

| | LIBD | FBB | MOF | FELD | BBS |
|---|---|---|---|---|---|
| **Event 1, Data** | $0.3 \cdot 10^{-3}$ | 18.5 counts | $0.7 \cdot 10^{-3}$ | not mod. | $0.5 \cdot 10^{-3}$ |
| **Event 1, Synt.** | $1.2 \cdot 10^{-3}$ | $4.8 \cdot 10^{-3}$ | $0.8 \cdot 10^{-3}$ | not mod. | $0.2 \cdot 10^{-3}$ |
| **Event 2, Data** | $3.0 \cdot 10^{-4}$ | not mod. | not mod. | not mod. | $1.0 \cdot 10^{-3}$ |
| **Event 2, Synt.** | $0.7 \cdot 10^{-4}$ | not mod. | not mod. | not mod. | $7.5 \cdot 10^{-5}$ |
| **Event 3, Data** | not mod. | 37 counts | not mod. | $7.5 \cdot 10^{-4}$ | $1.0 \cdot 10^{-3}$ |
| **Event 3, Synt.** | not mod. | $3.0 \cdot 10^{-4}$ | not mod. | $7.5 \cdot 10^{-4}$ | $1.2 \cdot 10^{-3}$ |

Table 2.7: *Peak ground velocities (m/s) for shear waves. The values for station FBB are displayed in counts. Several event-station pairs have not been modeled in this study.*

| | LIBD | FBB | MOF | FELD | BBS |
|---|---|---|---|---|---|
| **Event 1, Data** | 0.31 | 0.46 | 0.27 | not mod. | 0.10 |
| **Event 1, Synt.** | 0.08 | 0.08 | 0.22 | not mod. | 0.10 |
| **Event 2, Data** | 0.40 | not mod. | not mod. | not mod. | 0.70 |
| **Event 2, Synt.** | 0.29 | not mod. | not mod. | not mod. | 1.07 |
| **Event 3, Data** | not mod. | 0.59 | not mod. | 0.67 | 0.40 |
| **Event 3, Synt.** | not mod. | 0.37 | not mod. | 0.67 | 0.33 |

Table 2.8: *Same as table 2.7, but for shear waves.*

The best fits are obtained at station FELD for event 3 and at station BBS for event 1.

If the site effect at a certain station played a significant role, the ratios of data and synthetics should be similar for all events. At station FELD this hypothesis can not be checked since event 3 was the only one simulated at this station. Station BBS shows a significant difference of 35% for event 2, and a better fit (17.5% difference) for event 3. It is remarkable that the large P/S amplitude ratio of 0.7 which has been found in the data for event 2 finds equivalence in the synthetics with a ratio larger than 1. This large value could be due to the radiation pattern of the earthquake (see table 2.1). Poor results are found at station LIBD and station FBB for event 1 where the synthetics have extremely small P/S amplitude ratios with values below 0.1. A better fit with 27.5% and 37.3% difference is found at those stations for event 2 (station LIBD) and event 3 (station FBB). The amplitude ratio at station MOF differs by 19% for event 1, the only one modeled at this station. A comparison of amplitude ratios carried out after the application of different bandpass filters (1 – 2 Hz, 2 – 4 Hz, 4 – 8 Hz) shows no improvement of the fit.

### 2.4.4 Duration of Shaking

The duration of a seismic signal is a crucial parameter for seismic hazard evaluation. Prolonged exposure to shaking can lead to fatigue of material and, subsequently, failure. Duration is defined as the time between 5 % and 75 % of the cumulative squared ground acceleration [130]. It is influenced by the site condition, and can also vary due to resonances in shallow layers. For recordings in the vicinity of large earthquakes, the duration of shaking is dependent on rupture directivity. In the simulations of this study rupture directivity does not play a role since the three earthquakes are modeled as point sources. The durations for the events analyzed are compiled in table 2.9. The accelerations have been computed from the 1 – 8 Hz band-pass filtered velocity seismograms.
The durations for the three events in the Rhinegraben vary between 1.89 seconds (event 1 at station LIBD) and 9.41 seconds (event 3 at station FELD). The durations computed for the synthetics show an even larger variability. In some cases (e.g. event 3 at station FBB) the durations calculated for both, data and synthetics, are similar. In this case the duration of the synthetics amounts to 96.2 % of the duration of the recorded seismogram. For event 1 modeled at the same station, this value amounts only to 5.2 % which is the overall poorest agreement.

| | **LIBD** | **FBB** | **MOF** | **FELD** | **BBS** |
|---|---|---|---|---|---|
| **Event 1, Data** | 1.89 | 4.02 | 7.52 | not mod. | 5.92 |
| **Event 1, Synt.** | 0.60 | 0.21 | 0.48 | not mod. | 7.14 |
| **Event 2, Data** | 6.66 | not mod. | not mod. | not mod. | 8.22 |
| **Event 2, Synt.** | 9.24 | not mod. | not mod. | not mod. | 4.59 |
| **Event 3, Data** | not mod. | 7.30 | not mod. | 9.41 | 4.91 |
| **Event 3, Synt.** | not mod. | 7.02 | not mod. | 0.69 | 3.75 |

Table 2.9: *Duration of shaking for data and synthetics in seconds. Duration is defined as the time between 5 % and 75% of the cumulative squared acceleration.*

### 2.4.5 Response Spectra

A common method in the determination of seismic hazard is the computation of seismic response spectra. For each frequency, the spectral values are defined as the maximum response of an oscillator with a given eigenfrequency taking the seismic acceleration signal as external force. The amplification is dependent on the subsur-

face structure, the site conditions, and the frequency content of the seismic signal. Buildings having eigenfrequencies like the frequencies that show large amplifications in the spectra are most likely to be affected by the event. Response spectra are computed for spectral accelerations, velocities, and displacements. Only one example per event is shown.

Figure 2.8 (left) displays response spectra for event 1 recorded at station BBS. Response spectra for data and synthetics are depicted by the solid and dashed lines, respectively. The top plot shows the spectra for spectral displacements. Up to frequencies of 4 Hz the two spectra fit very well (misfit below 20 %). For larger frequencies the synthetics overestimate the values of the data by approximately a factor of 2. A similar situation is found for the spectral velocities which are shown in the second subplot. Up to 4 Hz the spectrum computed with the FD simulations matches the data within the scope of hazard assessment quite well with deviations below 25 % while the simulations predict larger values for higher frequencies. The spectral accelerations are underestimated significantly by the simulations (factor of approximately 50 %) for frequencies below 4 Hz and overestimated by the same dimension for frequencies above 4 Hz.

Event 2 for which response spectra are shown for station LIBD in figure 2.8 (middle) shows similar results. However, the response spectra computed for the modeling results underestimate those of the data for frequencies below 4 Hz for all three, displacements, velocities, and accelerations. Peaks that appear in the spectral acceleration of the data around 1 and 1.6 Hz could not be modeled.

Figure 2.8 (right) shows the results for event 3 recorded and computed at station FELD. Here, the discrepancy between data and synthetics is most obvious. The spectral accelerations are underestimated by a factor of up to 10 for certain frequencies below 3 Hz (e.g. 0.9 Hz, 2 Hz) which has significant impacts on the determination of seismic hazard. Only 30% of the amplitude of spectral velocities and displacements can be explained by the FD model.

## 2.5 Discussion

Key paramemeters for seismic hazard assessment are peak ground acceleration, duration of shaking, and spectral response values in the frequency band of the eigenfrequencies of most buildings. As a rule of thumb, an eigenfrequency $f$ in Hz of a building can be computed as

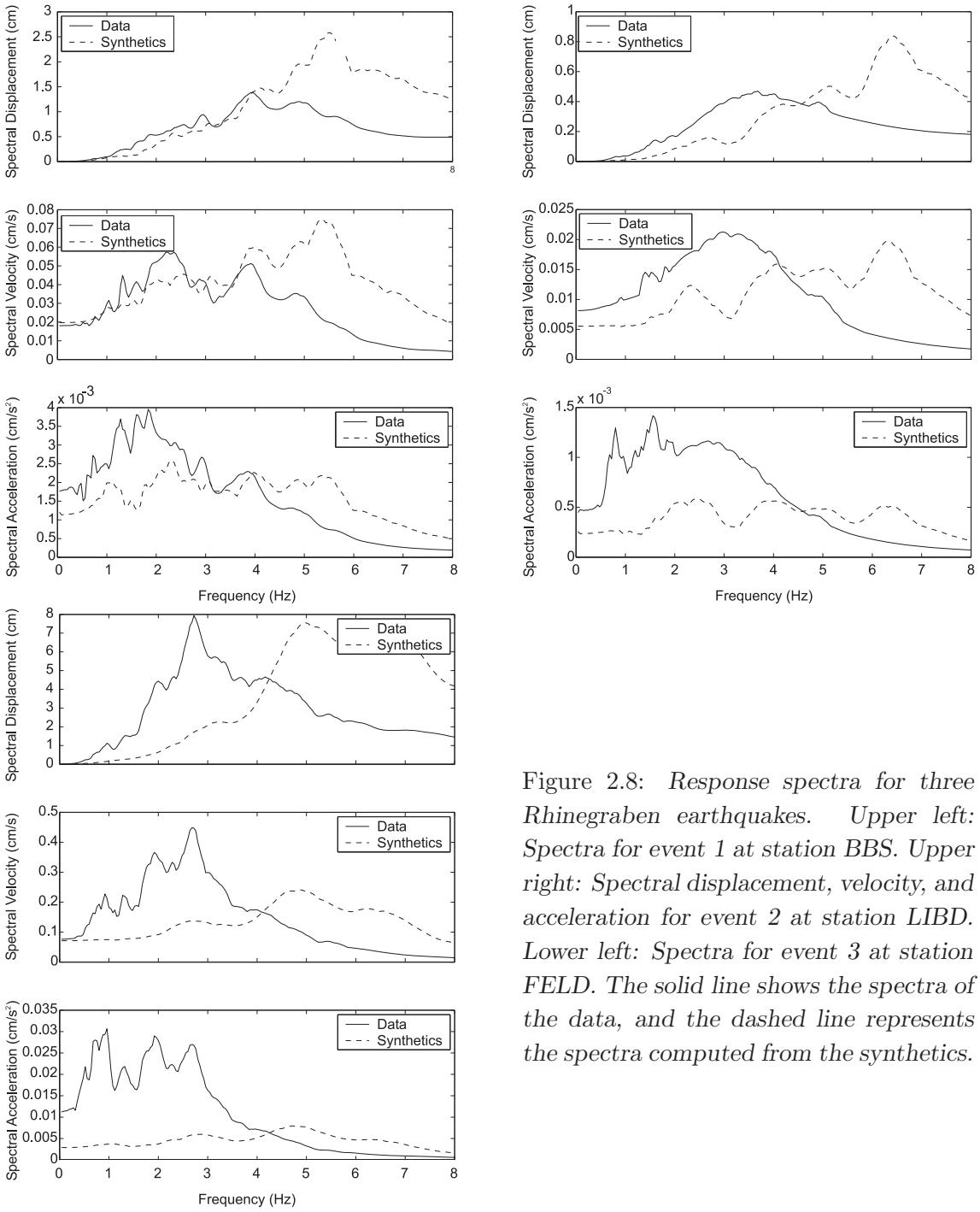


Figure 2.8: *Response spectra for three Rhinegraben earthquakes. Upper left: Spectra for event 1 at station BBS. Upper right: Spectral displacement, velocity, and acceleration for event 2 at station LIBD. Lower left: Spectra for event 3 at station FELD. The solid line shows the spectra of the data, and the dashed line represents the spectra computed from the synthetics.*

$$f = \frac{10}{n}, \tag{2.1}$$

where $n$ is the number of stories in the building. Accordingly, a house with two stories has an eigenfrequency of 5 Hz, and smaller buildings have higher eigenfrequencies. Low eigenfrequencies around 1 Hz can not only be observed for houses with many stories but are also found for large bridges. Since the architectural landscape in southern Germany, Switzerland and northeastern France is mainly determined by houses not exceeding a few stories, the frequency range between 1 and 8 Hz seems most important for hazard assessment of the Rhinegraben. In this section I will, exemplified by the peak velocities, discuss the differences between data and synthetics and give several possible explanations for the discrepancies before I address the issue of the usefulness of the results for hazard assessment purposes.

Peak velocities of the vertical component (PVV's) and averaged peak velocities of the horizontal components (PHV's) correlate with the damage pattern of an earthquake. Of those two, peak velocities of the horizontal components play a larger role for the determination of the seismic hazard since they (a) show generally larger values and (b) hit buildings in a direction where they are most vulnerable. In this study only peak values of the vertical component could be checked since the five stations are deployed with 1-component sensors only. This, however, gives already an estimate of the usefulness of the elastic model and shows to which extend the data can be approximated by the FD-simulations.

For local distances, peak amplitudes in the time-histories are usually part of the shear wave train. As shown above, both, over- and underestimation of the data by the simulations is found. The largest differences occur at station BBS for event 2 where both, compressional wave and shear wave amplitudes of the data exceed those of the synthetics by approximately a factor of 10. The same event shows large offsets for station LIBD. In most of the other cases the ratios are in the order of amplification factors of 2 – 3.

Several explanations are possible for the differences between data and synthetics: The fact that for frequencies below 4 Hz the spectral responses of the synthetics are smaller than those of the data and that the contrary is found for frequencies above 4 Hz could be an indication that the error results from the neglection of material attenuation. A pilot study for the Rhinegraben with basin velocities of $v_p = 4.5$ km/s and $v_s = 2.6$ km/s, and elastic quality factors of $Q_P = 1500$ and $Q_S = 1000$ showed that the P-wave amplitudes would be affected by less than 5 % for distances below 60 km and frequencies below 5 Hz when material attenuation was included while the

S-wave amplitudes suffer more from the neglection of material attenuation and are decreased by about 17.8 % for distances below 20 km, 20.0 % for distances below 40 km, and 22.2 % for distances below 60 km [46]. On cristalline rock ($v_p = 6$ km/s, $v_s = 3.5$ km/s) the shear wave amplitudes are decreased only 10 % for distances above 65 km. Thus if material attenuation was included, the simulated peak values would also be decreased. In some cases this would lead to a better estimate. In other cases, however, where the synthetics underestimate the data the fit would get worse by including attenuation.

The consideration of topography could influence the results as well. A longer travel-path leads to decreased amplitudes due to geometrical spreading. The effect should be largest for station FELD situated in the Black Forest at an altitude of approximately 1500 m. At this station, however, the peak compressional wave amplitude of the synthetics is already a factor 10 smaller than the peak value of the data, while the maximum shear wave amplitude fits the amplitude of the data very well. When topography is included, not only the amplitudes but also the arrival times of the synthetics would be affected. The waves would arrive later due to the increased distance. At station FELD the waves do already arrive more than one second too late compared to the data. The neglection of topography seems therefore a lower-order effect and not the appropriate explanation for the differences between data and synthetics.

Another explanation for incorrect amplitude values could be the inaccurate determination of the hypocentral depth of an event [131]. Peak particle accelerations depend strongly on the hypocentral depth [47]. In the vicinity of the source (distances closer than 20 km), peak accelerations are higher for the shallow source. Away from the epicenter, increasing hypocentral depth tends to generate increased peak accelerations. An increase of 100% can be observed when the hypocenter is moved from a depth of 15 km to a depth of 10 km. Qualitatively the observation is valid for velocities as well. For the three events studied the epicentral distances exceed 20 km at all stations. If the explanation was satisfactory, for one event the synthetics should either be too large or too small at all stations. The fact that a clear pattern can not be seen makes it less likely that the depth is determined incorrectly.

An explanation which seems most likely is the inaccuracy of the velocity- and density- model. Here again, several sources for the discrepancies can be accounted for: The elastic model could be erroneous on a large scale. An average increase of the compressional waves of approximately 1 km/s could explain the 1.2 seconds late arrival of the P-wave at station LIBD for event 3. Even though this increase

seems rather large, it is to emphasize that the later arrival of a phase has no immediate impact on the seismic hazard of the Rhinegraben. Small-scale features which are not included in the elastic model could also enhance the fit between data and synthetics. Possible meachanisms that could change waveforms and augment amplitudes are seismic scattering, focusing/defocusing effects, or resonances in shallow layers. Finally, the soil where the seismometer is located has an impact on the wave-amplitudes. In the simulation all stations are located on hard rock with S-wave velocities between 2.04 km/s and 2.2 km/s whereas in reality some stations might have different site conditions. Under the assumption that the site effect is constant for compressional and shear waves, the P/S peak amplitude ratio for both, data and synthetics, should show the same values. As mentioned above and summarized in table 2.8, for some instances this is the case whereas for some other examples the P/S peak amplitude ratio is very different between data and synthetics. Large site-effects in the data might also influence the duration of shaking. The duration of the synthetics would be expected either too long, too short or well reproduced for all events at one site which is not the case. For the peak values in the three events analyzed in this study both, over- and underestimation is found. The spectral responses show synthetic values smaller than those of the data for frequencies below 4 Hz and larger for frequencies above 4 Hz.

In most cases, the differences between data and synthetics amount to a factor of 2 or 3. Here, the synthetics are regarded as still being valuable for hazard assessment since the uncertainty in magnitude determination of historic events has the same dimension. When the seismic hazard of an area is assessed the magnitude of the maximum earthquake which is likely to occur in that region has to be taken into consideration. Since large earthquakes in intraplate regions occur irregulary, and the last devasting event in the Rhinegraben dates back more than 600 years, magnitude estimation is full of uncertainties. The ground velocities computed in the simulations for a point source would be a factor of 2 larger if the seismic moment was increased by this factor and all other parameters were kept constant and when material attenuation is neglected. An increase of the seismic moment of a factor of 2 increases the moment magnitude by 0.2. A difference in magnitude of 0.2 lies within the limits of accuracy of the magnitude determination. A difference in peak velocities of a factor of 10, however, as found in the case of event 2 at station BBS requires a difference in magnitude of almost 0.7. Even for historic events magnitude determination can be done more precisely than this value. Discrepancies of this dimension have also been found for the spectral accelerations. At station FELD for

event 3 this overestimation is as large as a factor of 10 for 0.9 and 2 Hz.
For seismic hazard estimation it is necessary that all values can be predicted within reasonable limits. Therefore I conclude that the model of elastic parameters, especially the sedimentary structure in the upper few hundred meters has to be known to a better extent and on a smaller scale if it shall in future be used for prediction of peak velocities and spectral values. A refinement of the subsurface model requires high-resolution experiments to resolve the 3D geological structures at least down to the scale of several hundred meters. Furthermore, for a more realistic comparison I consider it to be necessary to record the seismic events in the Rhinegraben by three-component stations.

# Chapter 3

# Case Study II: Modeling the 1927 Jericho Earthquake in the Dead Sea Basin

## 3.1 Motivation

The Dead Sea Rift (DSR) transform fault is a site of major historical seismic activity. Earthquakes in the DSR occur irregularly but with maximum magnitudes between 6.5 and 7.0. The Dead Sea Basin (DSB), a sediment-filled pull-apart basin, is situated at the center of the Dead Sea Rift. Despite of the large magnitudes, the level of ground motion is generally low south of the Dead Sea Basin, while large ground motion amplitudes have been observed to the north of the basin [127, 141]. The elongated structure of the basin with its deep (more than 10 km) sedimentary fill [41] suggests that it acts as a wave-guide, contributing to an anisotropic radiation pattern of seismic energy [140]. Recent 3D modeling of ground motion in deep basins [48, 103, 104, 118] clearly shows that focusing and defocussing effects can be significant.

The objective of this study is (a) to assess potential 3D variations in ground motion caused by the Dead Sea Basin substructure and (b) to consider its implications for seismic hazard assessment purposes. This issue is addressed by 3D modeling of 75 seconds of 1.5 Hz wave-propagation of the 1927 Jericho Earthquake ($M_L = 6.2$) for which reasonably precise information on location, magnitude, and damage is available [96, 123, 127]. From the time histories peak ground velocities ($< 1.5$ Hz) and spectral acceleration responses at 1 Hz are computed in a 3D model including the Dead Sea Basin substructure. The accelerations are then compared to values

computed (a) for a halfspace model with elastic parameters as in the bedrock of the Dead Sea Basin model, and (b) using an attenuation relation similar to the one integrated in the building code 413 of Israel.

## 3.2 Dead Sea Rift Transform Fault

### 3.2.1 Tectonics and Geology

In the mid-Cenozoic, the Arabian plate broke away from the African plate, forming the Dead Sea Rift transform at the boundary between the Arabian and an appendage of the African plate, the Sinai sub-plate. The transform is some 1000 km long and joins the divergent plate boundary along the Red Sea in the south with the converging orogenic belt in Turkey (figure 3.1). The Dead Sea Basin, being one of the largest pull-apart basins in the world, formed along the left-lateral DSR transform fault. Subsidence of the basin occured in large parts about 15 Ma or earlier with the site of fastest subsidence having shifted northward. By the end of the Miocene about half of the present length was reached [37]. Note that the Dead Sea Basin is located further north than the Dead Sea with which it overlaps only in the southern part of the basin.

### 3.2.2 Seismicity

The DSR transform is well known as a source region for earthquakes with magnitudes between 6.5 and 7.5. Since the region has been settled for many centuries, first reports of earthquakes date back to more than 4000 years. Several catalogues are available for major events [7, 8, 9, 16, 17, 127]. The largest of those are compiled in table 3.1.

### 3.2.3 The 1927 Jericho Earthquake

On July 11, 1927, a $M_L = 6.2$ earthquake occured under the town of Jericho where it destroyed several buildings and caused ground fissures. In many cities and villages in Judea, Samaria and Galilee the earthquake had even worse effects: More than 340 people were killed and almost 1000 were injured due to the collapse of buildings. The flow of the river Jordan stopped for 22 hours due to landslides. Shaking has been reported from regions 900 km away from the epicenter. The event could be recorded at several seismic stations then available in Europe, South-Africa, North-America,

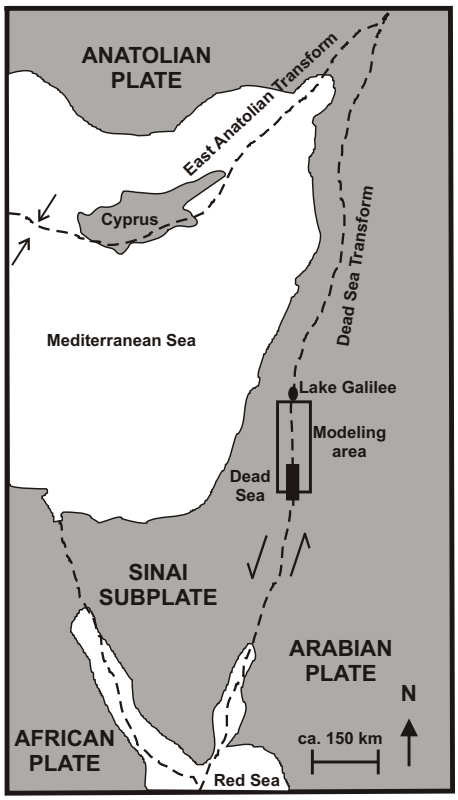


Figure 3.1: *Map of the Dead Sea Rift transform and the Dead Sea Basin (after [17]). Plate boundaries are indicated as dashed lines. The location of the Dead Sea and the Lake Galilee are sketched. The approximate location of the modeling area is indicated as a black dashed rectangle.*

and even Australia, thus extending the microseismic coverage to more than 14000 km [96, 127].

Figure 3.2 shows the distribution of the macroseismic intensity for this event. The intensity pattern shows a distinct extension to the north: The area where the largest damage is found (intensity = X) is situated approximately 50 km north of the epicenter on the eastern side of the Ephraim mountains and is embedded in a kidney-shaped elongated zone of intensity > VIII. Even further to the north, in a distance of approximately 100 km from the epicenter, two patches with intensity level VIII – IX are situated. The deviation from a more radially-shaped intensity distribution has been reported for several other events [127] and is suggested to be related to the elongated structure of the Dead Sea Basin which acts like a wave-guide [141].

| **Year** | $M_L$ **(est.)** | **Details** |
|---|---|---|
| 2100 BC | 6.8 | Upheaval in southern Dead Sea, destruction of Jericho. |
| 759 BC | 7.3 | King Solomon's temple in Jerusalem damaged. |
| 746 AD | 7.3 | Destruction of the Omayad Hesham palace. near Jericho. |
| 1170 AD | 7.5 | King herod's obelisk at Ceasaria thrown down. |
| 1202 AD | 7.5 | Great damage and many victims in Baalbek and Tiberias. Felt in a distance of 1200 km. |
| 1546 AD | 7.0 | Seiches in the Dead Sea. Waters of river Jordan cut for 2 days. |
| 1759 AD | 7.4 | Destruction in Baalbek. Parts of Damaskus destroyed. |
| 1837 AD | 6.7 | Destruction of Safed and Tiberias, 3000 victims. |
| 1927 AD | 6.2 | Epicenter in Jericho. First event instrumentally recorded. |

Table 3.1: *Large historic earthquakes connected to the Dead Sea Rift transform fault.* $M_L$ *(est.) stands for the estimated local magnitude.*

## 3.3 Modeling Parameters

### 3.3.1 Elastic Model and Geometry

A simplified 3D elastic model as proposed for the DSB area [5, 37] is used for the simulation (figure 3.3). It consists of a basin, $15 \cdot 100$ km$^2$ in size, with three layers that are embedded in crystalline bedrock ($v_p = 5.5$ km/s, $v_s = 3.2$ km/s, $\rho = 2.7$ g/cm$^3$). The upper layer with $v_p = 4$ km/s, $v_s = 2.3$ km/s and $\rho = 2.1$ g/cm$^3$ corresponding to shales and clastics extends to a maximum depth of 5 km. The two underlying layers extend in the center of the basin to a depth of 9 km and are composed of salt and quartzrose sandstones ($v_p = 4.5 - 5$ km/s, $v_s = 2.6 - 2.9$ km/s and $\rho = 2.4 - 2.6$ g/cm$^3$). Small-scale features in the geometry of the basin have been deliberately ignored in order to keep the model as simple as possible. The relatively low frequencies ($< 1.5$ Hz) correspond to a minimum wavelength for shear waves of 1.5 to 2.0 km. Thus, model features below this scale are considered as unimportant. Changes in the model of this scale size would not affect the results significantly. For the same reason no mountain topography has been included in the model. The simulations comprise no material attenuation since the effect is not

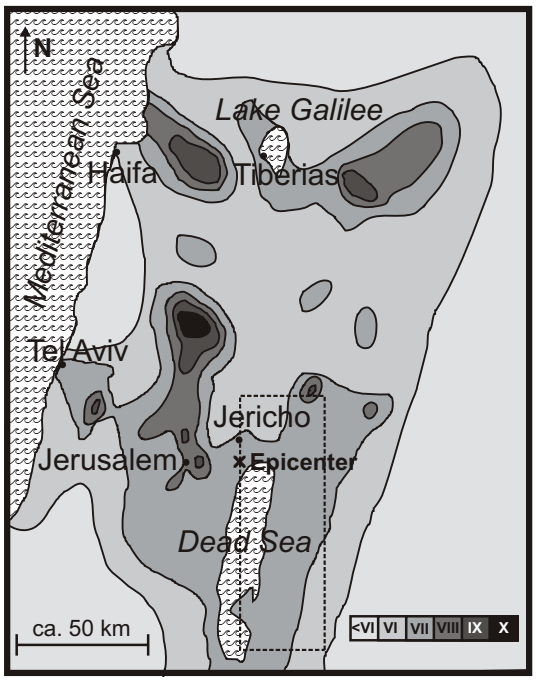


Figure 3.2: *Distribution of macroseismic intensity for the 1927 Jericho earthquake (after [127]). The maximum intensity amounts to X and is found approximately 50 km north of the epicenter. Two further patches with large (IX) intensities are found to the east and to the west of Lake Galilee. The approximate locations of the epicenter and the outline of the basin are indicated by a star and a dashed rectangle, respectively.*

important at the frequencies and distances considered.
The observed ground motion in and outside the basin will be influenced by both the basin structure and the site effects in the valley. However, I only address the first effect so that variations in ground motion distribution will be aggravated if site effects are included.

### 3.3.2 Computational Parameters

A triangular-shaped slip rate with a rise time of 0.48 seconds [58] was used. The seismic moment $M_0$ was computed by a scaling relation [57, 69], assuming the local magnitude $M_L = 6.2$ to scale like the moment magnitude $M_W$ [6]. Empirical relations for strike-slip events [138] were used to compute the size of the rupture area ($12 \cdot 12$ km$^2$). The hypocenter is located at a depth of 7 km at the southern edge of the fault. The rupture front propagates with 70% of the local basin shear wave speed [38]. Further modeling parameters are compiled in table 3.2.

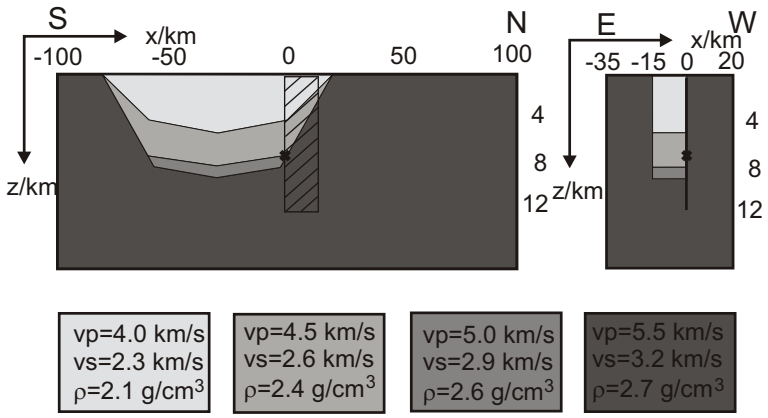


Figure 3.3: *Two cross-sections of the model of elastic parameters used for the simulation of the Jericho earthquake. Note that the vertical axis is exaggerated by a factor of 4. The square fault plane is thus indicated as black dashed rectangle (left) and black line (right). The hypocenter, located at a depth of 7 km at the southern end of the fault, is displayed as a black cross.*

## 3.4 Numerical Results

In this section snapshots of ground velocity at the surface, seismograms, peak ground velocities, and the averaged horizontal spectral acceleration response (1 Hz) are shown, and 75 seconds of 1.5 Hz elastic wave-propagation in the DSB model are analyzed. Accelerations have further been computed (a) for a model that contains constant elastic parameters equivalent to the bedrock parameters of the DSB model (hereafter called homogeneous model), and (b) using an attenuation relation [22] that is similar to the one integrated in the building code 413 of Israel, but allows additionally frequency-dependent analysis. Those will be compared to the spectral accelerations computed for the DSB model.

### 3.4.1 Snapshots of the Wavefield

Snapshots of ground-velocity are shown in figure 3.4. The figure displays the horizontal component parallel to the strike of the fault. Large positive values are indicated by dark colors. After approximately 2 seconds the waves reach the surface. Five seconds after the initiation of the rupture, due to rupture directivity, north of the fault wave amplitudes are larger than south of it. A superposition of reflections from the eastern edge with later arrivals causes large amplitudes due to positive interference 10 seconds after the first breaking of the fault. On this horizontal component,

| | |
|---|---|
| Spatial discretization (m) | 200 |
| Temporal discretization (s) | 0.015 |
| Number of timesteps | 5000 |
| Simulation time (s) | 75 |
| Number of E-W grid points | 1000 |
| Number of N-S grid points | 275 |
| Number of vertical grid points | 87 |
| Hypocentral depth (km) | 7 |
| Width of fault along dip (km) | 12 |
| Length of fault along strike (km) | 12 |
| Strike (°) | 0 |
| Dip (°) | 90 |
| Rake (°) | 0 |

Table 3.2: *Geometrical modeling parameters used for the simulation of the Jericho earthquake.*

due to the location of the rupture and the geometry of the basin, a large amount of seismic energy leaves the basin at its northeastern corner. This effect is reversed on the horizontal component perpendicular to the strike of the fault leading to overall larger wave-amplitudes at the corners of the basin than in between.

### 3.4.2 Seismograms

Three-component seismograms from six locations are shown in figure 3.5. Three sites are located 60 km north of the epicenter (D – F) and three others (A – C) 60 km south. Site B is located within the basin while the other five sites are based on bedrock. Generally, as an effect of rupture directivity, south of the epicenter (sites A – C) the duration of shaking is larger than north of it (sites D – F). For the same reason amplitudes on the stations north of the epicenter are larger than the amplitudes to the south. This amplification reaches a factor of approximately 35 for the horizontal component perpendicular to the strike of the fault on the westernmost stations (A, D). The horizontal components perpendicular to the strike of the fault show larger amplitudes than those parallel to the fault. This effect can be seen in forward as well as backward rupture directions [130]. Further, two to three times larger amplitudes at the station located within the basin (B) are found compared to the stations to the east (C) and west (A).

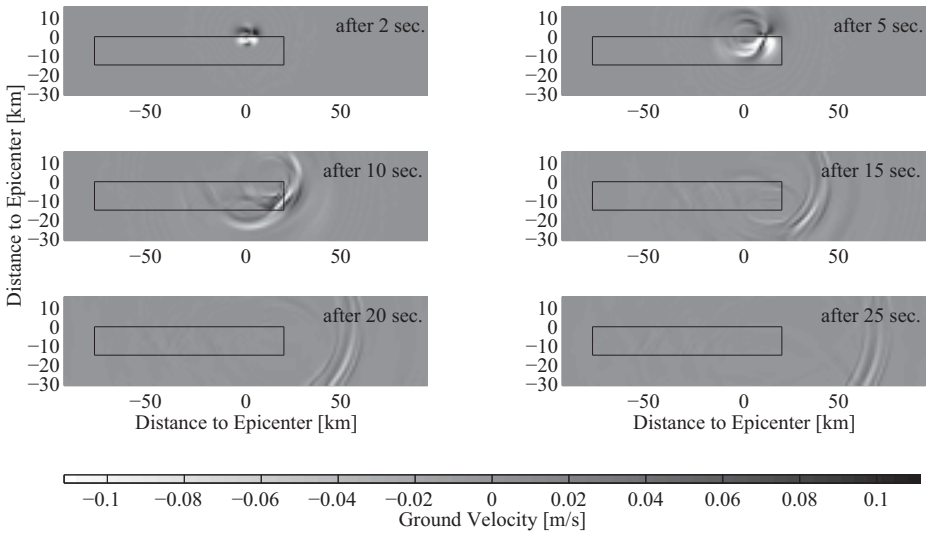


Figure 3.4: *Snapshots of the wavefield at the surface (horizontal component parallel to the fault). Large positive values are depicted by dark colors, and large negative values by bright colors. The basin outline is indicated by a black rectangle. South is at the left, and north at the right side of each image.*

### 3.4.3 Peak Ground Velocities

The spatial distribution of peak ground velocities is shown in figure 3.6. The horizontal component parallel to the fault shows the largest values. The maximum value (black) of 8.06 m/s is found within the basin close to the southern end of the rupture on this component, 300 m northeast of the epicenter. Along the rupture, radiation takes place mainly within the basin causing the peak values within the basin to be more than three times as large as symmetrically outside of it. The displacement amplitude of a seismic point source scales with the inverse third power of the shear wave velocity. Thus, an event produces higher ground motion if the source is located in a low-velocity medium. Reflections from the northern basin edge produce large amplitudes just south of the northern edge of the basin and at its eastern edge. Two lobes of large amplitudes that are also reflected in the intensity pattern (compare figure 3.2) are visible north of the basin. They develop within the basin due to positive interference of the reflected waves with later arrivals. Those waves leave the basin at its corners leading to large amplitudes northeast and northwest of the basin.

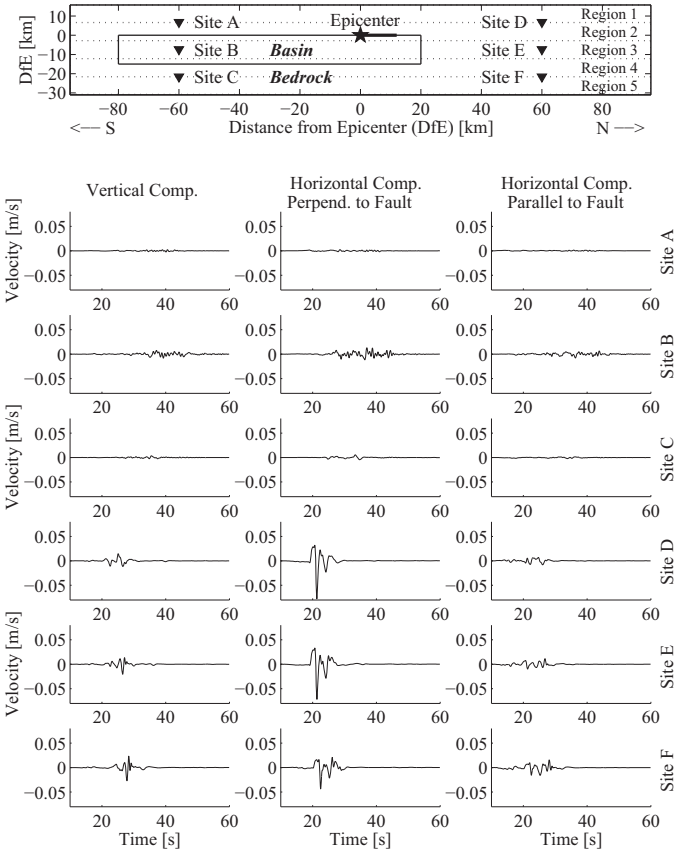


Figure 3.5: *Top: Location of sites A – F and division of the surface into five regions (compare to figure 3.7). Epicenter and rupture are indicated by a star and a fat solid line. Below: Velocity seismograms calculated at the surface. Sites A – C are located 60 km south of the epicenter, and sites D – F lie 60 km to the north. The three columns show seismograms of the vertical component, and the two Horizontals perpendicular and parallel to the strike of the fault.*

### 3.4.4 Spectral Accelerations

The distribution of ground motion is influenced by different effects which can be divided into two groups. The first group contains effects due to rupture propagation, includes directivity effects, and effects due to the radiation pattern. The second type of effects has to do with the subsurface distribution of elastic parameters. It comprises amplification of ground motion that is caused by reflection and focusing, and includes local site effects related to the low velocities of the sediments.
Computing spectral accelerations with the attenuation relation that does not include directivity effects can isolate the first group of effects. The computation is carried out for an average of the two horizontal components and consequently excludes the differences that are due to the radiation pattern.
The averaged horizontal spectral accelerations $Y$ are computed by the following equation for each single source point, and added accordingly to the rupture velocity and the distance to the hypocenter:

$$\ln Y = b_1 + b_2(M_W - 6) + b_3(M_W - 6)^2 + b_4 \ln r + b_5 \ln \frac{v_{s30}}{v_a}. \qquad (3.1)$$

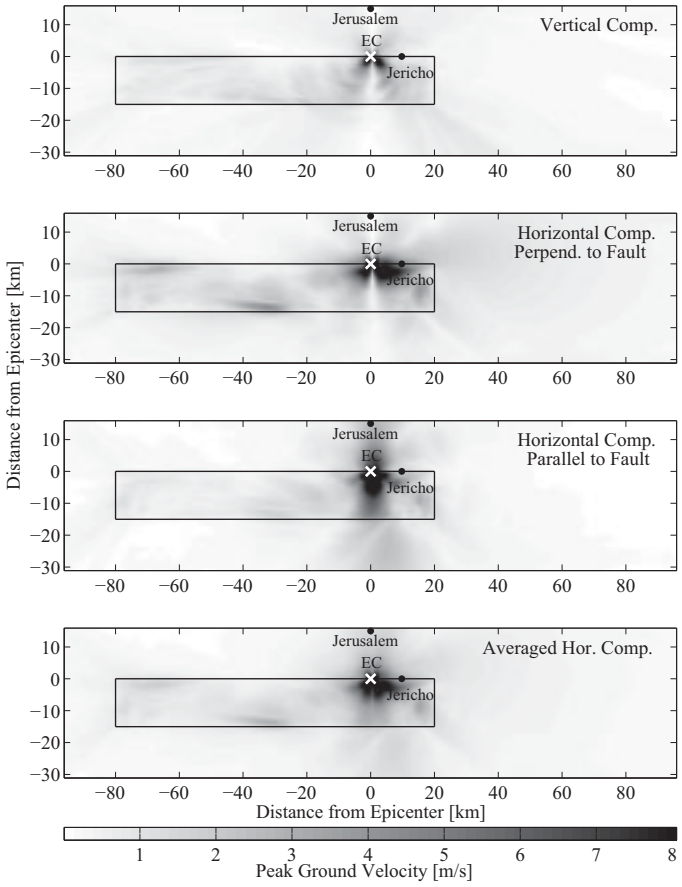


Figure 3.6: *Spatial distribution of vertical and horizontal components of peak ground velocities. The outline of the basin is indicated by a black rectangle. South is at the left, and north at the right side of each image. The largest value of ground motion (8.06 m/s) is found on the horizontal component parallel to the fault. The locations of the cities Jerusalem and Jericho are indicated by dots. The epicenter is displayed as a white cross and marked by the letters* EC.

The coefficients $b_1$ to $b_5$ and $v_a$ were determined for shallow earthquakes in western North-America by regression analysis in dependence on frequencies and source mechanisms [22]. It is similar to the attenuation relation used in the building code 413 of Israel [21], but allows frequency-dependent analysis. Here, I use the values for $f = 1$ Hz and strike-slip mechanism. $M_W$ denotes the moment magnitude of the event, $r$ is a distance dependent parameter, and $v_{s30}$ stands for the average shear wave velocity of the top 30 m.

Since both FD-simulations use the same rupture parameters, a comparison between accelerations from both simulations isolates the effects caused by the second group, namely the elastic parameters of the DSB substructure model.

A comparison of 1-Hz spectral acceleration response can be found in figure 3.7. The figure displays accelerations along N-S lines for five different regions (see figure 1). Within these regions the values have been averaged by adding the accelerations with the same N-S extension and dividing the value by the number of summands. The solid line represents the results for the values computed in the DSB model ($Y_{FD1}$),

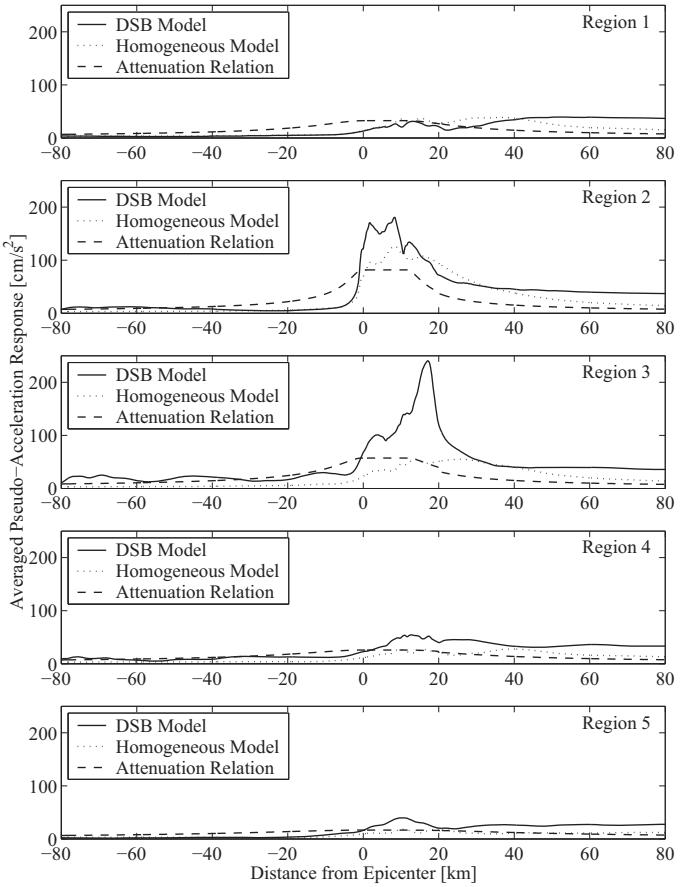


Figure 3.7: *Averaged spectral acceleration response. The solid line depicts the values for the DSB model. The results for the homogeneous model are indicated by the dotted line. The dashed line shows the results for the computation using the attenuation relation utilized in Israel's building code. The average is computed for five regions (see figure 3.5).*

the dashed and dotted lines show accelerations predicted by the homogeneous model ($Y_{FD2}$) and the attenuation relation ($Y_{AR}$), respectively. For a better comparison, I compute the ratios $R_{FD} = Y_{FD1}/Y_{FD2}$ and $R_{AR} = Y_{FD1}/Y_{AR}$.

$R_{AR}$ is on average small south of the epicenter (with values below 2) and gradually increases from the northern basin edge towards north up to a value of just below 5. The acceleration of the computed data exceeds the 84% percentile of the attenuation relation estimate by a factor of 2. The largest ratio can be found just south of the northern end of the basin (region 3, km 17.5). At this point the amplification caused by reflections at the edge of the basin reaches 5.1. Remarkable differences can also be observed close to the source (region 2). The area from the epicenter (km 0) to the end of the basin (km 20) is characterized by average ratios of 2.0 to 2.5. As possible explanation I consider rupture dynamics. Adding one $\sigma$ can explain more than 80% of the FD result.

$R_{FD}$ is generally smaller than $R_{AR}$. North of the basin, the ratio is on average on the order of 2 – 2.5. At the northern end of the basin an amplification factor of 5.1 is found. In its southern and northern part the $R_{FD}$ values are similar, being larger

in regions comprising the basin (region 2 – 4, $R_{FD}$ on average 4), and smaller in the two remaining ones ($R_{FD}$ 1.5 – 2).

## 3.5 Discussion

Using a simplified large-scale model of the Dead Sea Basin substructure, the FD-simulation can explain the increased amplitudes north of the basin. Two possible causes are discussed: Rupture dynamics causes the amplitudes north of the epicenter to be larger than south of it. Additional contributions the heterogeneous ground motion distribution are due to the geological structure of the DSB which contributes more to ground motion amplification potential than the rupture propagation. Consequently, the effect of the sedimentary structure of the DSB should be accounted for while assessing the seismic hazard of the region.

The pattern of increased intensities can however only partly be reconstructed with the modeling. A comparison of the intensity map (figure 3.2 to the areal plot of peak ground velocities (figure 3.6) shows that the modeling predicts the largest peak ground velocities (8.06 m/s) in the vicinity of the epicenter, a region with intensity VII. Approximately 50 km northwest of the epicenter where the maximum intensity was observed, peak ground velocities are in fact larger than south of the epicenter, but still considerably smaller than around the epicenter. Here, the peak ground velocity amounts to only 0.2 m/s on the horizontal component parallel to the strike of the fault. This value is rather small compared to the maximum peak ground velocity computed in the vicinity of the epicenter. However, it seems not too small to be responsible for the damage observed. The large value of peak ground velocity computed near the epicenter though, is unrealistically high compared to observations. This might be due to the fact that the area containing peak ground velocities $> 5$ m/s is limited to epicentral distances of less than 1 kilometer within the basin. For the bedrock the maximum value computed amounts to 2.5 km/s and is located just 200 meters from the epicenter. The isoline for a peak ground velocity of 1 m/s is located in a maximum epicentral distance of five kilometers within the basin and one kilometer on the bedrock. Observations for small epicentral distances are very rare, and it is not clear from the reports by Sieberg how many near-source observations he included in the compilation of his intensity map.

A change in the rupture velocity of the Finite Difference model can increase the agreement between the intensity map and the distribution of peak ground velocities [50]. In a second simulation, the rupture velocity amounts to 90% of the local shear

wave speed. All other parameters are kept constant. Figure 3.8 shows the averaged horizontal component of the peak ground velocity for this scenario. Here, extremly large values of peak ground velocities as observed for the first simulation are missing. The maximum value amounts to 1.78 m/s and is found 1 km north of the epicenter and 400 meters east of the fault within the basin on the horizontal component parallel to the strike of the fault. In the area where the maximum intensities were observed, the peak ground velocity on the horizontal component perpendicular to the fault takes a value of 0.1 m/s. Just north of the basin, peak ground velocities of 0.4 m/s and 0.5 m/s are computed on the horizontal component parallel and perpendicular to the strike of the fault, respectively. This corresponds to an increase of factors of 15.5 and 8.6 compared to the location symmetrically south of the epicenter.

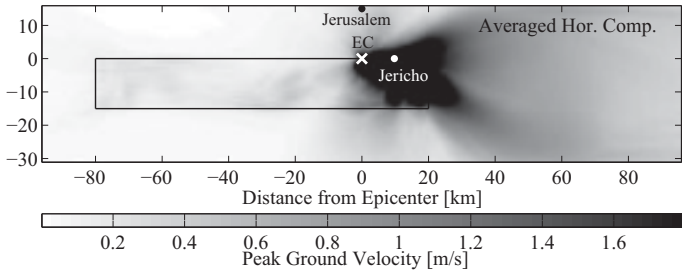


Figure 3.8: *Spatial distribution of the averaged horizontal component of peak ground velocities for a simulation where the rupture velocity $v_r$ amounts to 90% of the local shear wave speed $v_s$. The outline of the basin is indicated by a black rectangle. South is at the left, and north at the right side of each image.*

Even though qualitatively the fit could be observed with the second simulation, in both simulations the maximum peak ground motions are located in the epicentral region while the maximum intensity has been reported from approximately 50 kilometers northwest of the epicenter. The consideration of local site conditions could influence the results significantly. This might play a crucial role for the area where Sieberg found the maximum intensity, which is located just to the east of the Ephraim mountains.

# Chapter 4

# Case Study III: Modeling Ground Motion on Dipping Faults

## 4.1 Motivation

Near-source ground motion caused by dipping faults is independently of the radiation pattern significantly asymmetric [82]. This fact has been observed in seismic data recorded during recent large events as for example the 1994 Northridge (USA) or the 1999 Chi-Chi earthquake (Taiwan) [28]. The asymmetry could be verified from field evidence [24] and modeled by 2D and 3D simulations of ground motion [2, 14, 97]. In some cases, the near-field ground motion on the hanging wall can be increased by a factor of 3 due to normal-stress interaction effects [1]. Larger ground motion on the hanging wall is caused by time-dependent normal-stress interaction between the fault and the free surface (figure 4.1)[98]. Significant effects on the ground motion, including the asymmetry between the foot- and hanging walls, is caused by break-out phases and trapping of seismic energy between the fault and free surface [99]. This could also be seen in a dynamic model of the Northridge earthquake, where negligible free-surface effects on the rupture propagation for the fault buried 5 km were found [93]. The presence of a low-velocity zone can significantly affect the rupture velocities, slip-velocity functions and normal stress on the fault. These effects include slowing or increases in rupture velocity, in some cases transitions to super-shear velocities [36, 56].

Recently, analytical solutions for the 2D ground motion for a dip-slip fault in a halfspace could be derived [81]. The different waves generated when the fault breaks the surface could be identified. In a halfspace, the strongest ground motions are caused by a Rayleigh wave radiated in the forward direction. The rupture front wave

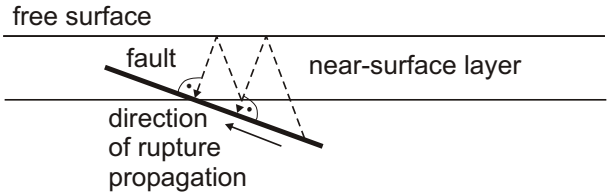


Figure 4.1: *Illustration of the time-dependent normal-stress effects. The dashed arrows indicate the direction of normal-stress interaction. Waves radiated from the fault that are reflected at the free surface take different travel paths before arriving at different parts of the fault. The normal stresses that are affected by the free-surface thus lead to varying normal-stress values on the fault. This effect is time-dependent: The dynamic rupture front propagates with an unconstrained rupture velocity determined by local stress and friction conditions. Such an interaction is not present when the rupture is inserted kinematically by a predetermined slip distribution.*

is cancelled by the stopping phase [81] and therefore disappears in the footwall.
Scenario earthquake simulations, generally using kinematic (prescribed) rupture parameters are becoming increasingly popular and attain an important role in hazard analysis [49, 59, 88, 89, 108]. However, the results discussed above suggest that these prescribed ruptures generally do not include near-surface effects from normal-stress interactions. While dynamics already has been included in the fault descriptions of the scenario simulations instead of the kinematic descriptions [107, 111], a widespread use of spontaneous rupture description is likely not going to be the case in the near future due to numerical and computational difficulties.
It is therefore imperative to quantify and include any lessons learned from dynamic rupture simulations that may lead to more accurate kinematic rupture implementations, which typically do not include the bias caused by normal-stress interactions between the fault and the free surface. In this study, dynamic normal-stress interactions on the near-field ground motions will be quantified. This is done by comparing the ground motion from dynamic simulations to that from kinematic ruptures with prescribed rupture parameters at different depths of the burial of the fault ($0 - 5$ km). An important incentive of this analysis is to estimate a threshold depth for the top of the fault above which the normal-stress effects leave considerable signature in the ground motion. Such estimate may be used as guidance to improve the ground motions in simulations of scenario earthquakes on dipping faults, typically carried out using prescribed ruptures where normal-stress effects are not included. The physics of the rupture propagation leading to the differences will be analyzed.

Finally the influence of shallow low-velocity layers on the normal-stress effects will be examined.

## 4.2 Modeling Parameters

### 4.2.1 Elastic Model and Geometry

The model dimensions and geometry are inspired by the 1994 $M_W$ 6.7 Northridge earthquake which occurred on a blind thrust fault below the San Fernando Valley. A planar, 20 km by 20 km fault plane, with the top at 0 km, 0.5 km, 1 km, 3 km, and 5 km below the surface is used. The latter represents the situation for the Northridge earthquake, and the remaining scenarios depict the cases had the fault ruptured to shallower depths.
Most of the simulations are carried out in a uniform halfspace model (UHS) in order to isolate the dynamic normal-stress effects. However, the halfspace model is later replaced by a model with including one (1LOH) and two (2LOH) layers over the same halfspace. The values for the elastic parameters for all three models are compiled in table 4.1. The synthetics contain frequencies up to 1 Hz.

| | **UHS** | **1LOH** | | **2LOH** | | |
|---|---|---|---|---|---|---|
| $\mathbf{v}_p$ **(km/s)** | 5.0 | 2.0 | 5.0 | 1.5 | 2.0 | 5.0 |
| $\mathbf{v}_s$ **(km/s)** | 3.2 | 1.0 | 3.2 | 0.5 | 1.0 | 3.2 |
| $\rho$ **(g/cm$^3$)** | 2.7 | 2.1 | 2.7 | 1.8 | 2.1 | 2.7 |
| **Depth (km)** | 0.0 | 0.0 | 1.0 | 0.0 | 0.4 | 1.0 |

Table 4.1: *Model of elastic parameters used for the simulation of ground motion from dipping faults.*

Figure 4.2 shows the modeling area with the projection of the fault and the location of two profiles along which synthetic seismograms for kinematic and dynamic simulations will be compared. The location of the profiles were chosen in order to highlight some of the largest differences between the two sets of simulations. Geometrical modeling parameters are summarized in table 4.2.

### 4.2.2 Dynamic Computational Parameters

In the dynamic simulations of the study mixed boundary condition and friction parameters were used. The method which is in more detail explained in section 1.6.1

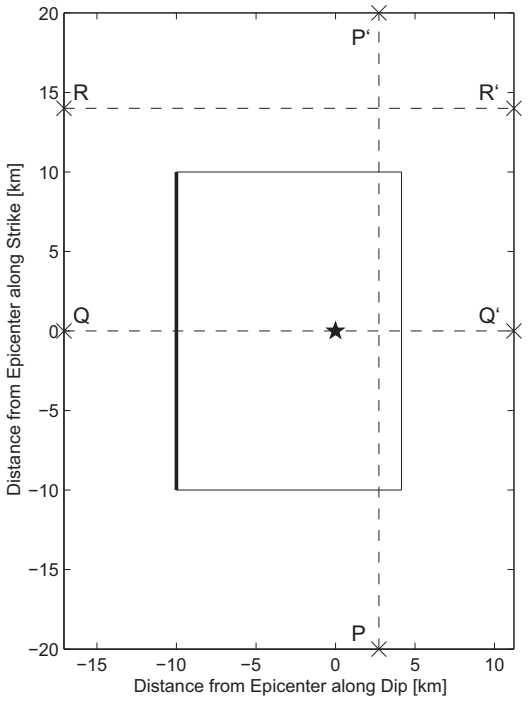


Figure 4.2: *Surface projection of model geometry. The fat solid line represents the projection of the fault tip (surface break for faults that come up to the top). The rectangle depicts the projection of the fault plane. The epicenter is indicated by a star. Dashed lines show the location of the profiles in figures 4.7 and 4.13 to 4.16.*

was successfully applied to dynamically model the 1994 Northridge earthquake and generated synthetics with a good fit to selected strong motion records in the San Fernando Valley [93]. While the previously mentioned investigation used a heterogeneous initial stress field computed from slip inversion results, here a homogeneous initial stress field is used in order to isolate the effects of the normal-stress interaction in the presence of the free surface. Moreover, all dynamic simulations in this study use values of the parameters $D_c, V_c$, and the yield stress which are constant across the fault. These values are selected as those for the preferred model of the above mentioned study [93], listed in table 4.3. The heterogeneity generated in the dynamic rupture is therefore due to normal-stress interactions between the fault and the free surface or near the unbreakable boundaries of the fault for the halfspace model, or the geological stratification in the uppermost part of layered models.
Figure 4.3 shows the slip distributions obtained for the fault buried to a depth of 5 km, using only slip weakening (left) and with a combination of slip and sliprate weakening (right). The slip distributions are scaled with a constant so that the left image corresponds to the magnitude of the $M_W$ 6.7 Northridge earthquake.

| | |
|---|---|
| Spatial discretization (m) | 200 |
| Temporal discretization (s) | 0.0015 |
| Number of timesteps | 2000 |
| Simulation time (s) | 30 |
| Number grid points perpendicular to strike | 200 |
| Number of grid points parallel to strike | 300 |
| Number of vertical grid points | 400 |
| Width of fault along dip (km) | 20 |
| Length of fault along strike (km) | 20 |
| Hypocentral depth (km from top of fault plane) | 14.14 |
| Strike (°) | 0 |

Table 4.2: *Geometrical modeling parameters used for the simulations of ground motion on dipping faults.*

| | |
|---|---|
| Slip weakening distance $D_c$ (m) | 0.15 |
| Rate weakening distance $V_c$ (m/s) | 0.092 |
| Yield stress (MPa) | 24 |
| Initial stress on fault (MPa) | 17.5 |

Table 4.3: *Dynamic modeling parameters.*

### 4.2.3 Kinematic Computational Parameters

Prescribed rupture propagation is simulated by kinematically adding the sliprate that has been computed on the fault from the dynamic simulation for a fault burial of 5 km. This procedure is explained in section 1.6.1. It assumes that the dynamic free-surface effects are negligible at this depth, which has been verified. Variations in rupture velocity arising from dynamic rupture propagation from the nucleation towards the free surface are present in both dynamic and kinematic ruptures and affect the ground motion equally. Thus, the results reflect the time-dependent dynamic (normal-stress) interaction with the free surface/geological layering for various depths of burial of the fault.

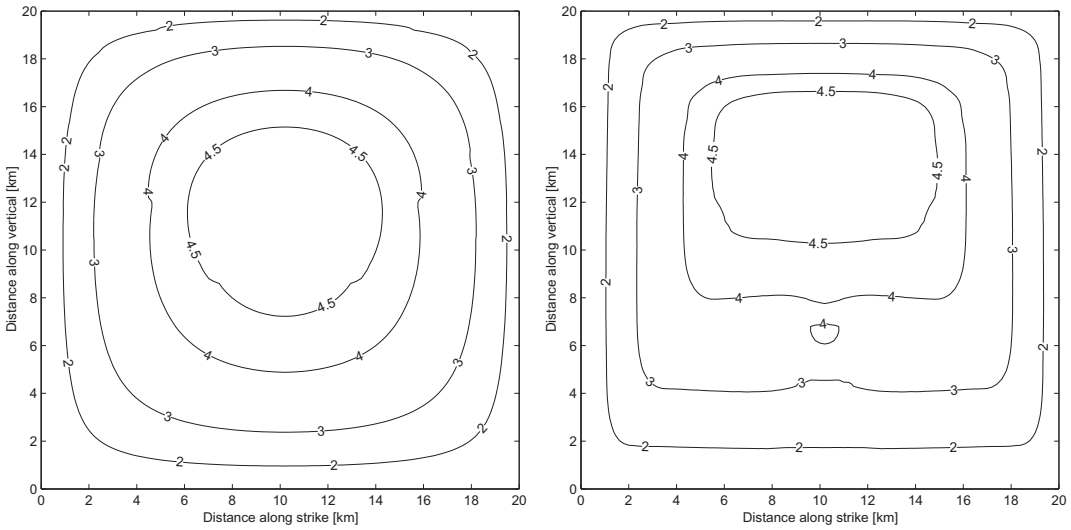


Figure 4.3: *Final slip distribution for a 45$^o$ dipping fault buried at 5 km using (a) only slip-weakening and (b) a combination of slip- and sliprate- weakening. The image displays the fault plane.*

## 4.3 Numerical Results

### 4.3.1 Uniform Halfspace (UHS) Model

In the following I will compare the dynamic and prescribed ruptures as well as the resulting ground motion in the UHS model. It is possible to compare the two sets of simulations scaled to a certain magnitude or moment for a specific depth of burial of the fault. Such scaling is often done for scenario simulations [104]. Another possibility is to scale the series of dynamic ruptures by a constant to match the moment of the prescribed rupture at depth, i.e. where the effects of the normal-stress effects from the free-surface are negligible for the frequencies considered. This scaling retains the normal-stress effects in the rupture propagation and therefore increases the moment additionally. Here, the latter scaling is chosen to isolate the normal-stress effects while the increase in moment caused by the normal-stress effects is listed in tables 4.4 and 4.5. The main analysis is carried out for a 45$^o$-dipping fault, compared to results from 30$^o$- and 60$^o$-dipping fault scenarios, to examine the influence of dynamic effects at the free surface by the dip of the fault plane.

A key parameter for the comparisons is the ratio of dynamic and kinematic peak ground displacements and velocities above and surrounding the surface projection of the fault. Spatially-variable root-mean-square (rms) ratios of dynamic and kinematic

| **Dip Angle** | $45^o$ | $30^o$ | $60^o$ | $45^o$ |
|---|---|---|---|---|
| **$D_c$ (cm)** | 15 | 15 | 15 | 15 |
| **$V_c$ (cm/s)** | 0 | 0 | 0 | 9.2 |
| **Depth (km)** | | | | |
| 0 | 1.57 | 1.57 | 1.71 | 1.36 |
| 1 | 1.13 | 1.12 | 1.21 | 1.11 |
| 3 | 1.04 | 1.03 | 1.04 | 1.04 |
| 5 | 1.00 | 1.00 | 1.00 | 1.00 |

Table 4.4: *Seismic dynamic/prescribed moment ratios in a halfspace model.*

| | |
|---|---|
| 1LOH, uniform prestress | 1.72 |
| 2LOH, uniform prestress | 1.82 |
| UHS, square-root tapered prestress | 1.44 |
| UHS, prestress = 0 in upper 2 km | 1.28 |
| UHS, heterogeneous prestress in upper 1 km | 1.55 |

Table 4.5: *Seismic dynamic/prescribed moment ratios for $45^o$-dipping fault: Effects of near-surface layers and near-surface stress. 1LOH and 2LOH stand for one and two layers over a halfspace (see section 4.3.2), respectively, and UHS stands for uniform halfspace. For the models with varying prestress see section 4.3.3.*

peak displacement (RD) and velocity (RV) are computed as

$$RD = \frac{PD_{dyn}(x,y)^{\mathrm{RMS}}}{PD_{kin}(x,y)^{\mathrm{RMS}}} \quad \text{and} \quad RV = \frac{PV_{dyn}(x,y)^{\mathrm{RMS}}}{PV_{kin}(x,y)^{\mathrm{RMS}}}, \tag{4.1}$$

where $PD(x,y)^{\mathrm{RMS}}$ and $PV(x,y)^{\mathrm{RMS}}$ denote rms-values of the peak displacements and velocities, and *dyn* and *kin* stand for dynamic and kinematic (prescribed) rupture implementation.

### $45^o$ Dipping Thrust Fault

Snapshots of the velocity wavefield on a plane vertical to the rupture plane and the surface are shown in figure 4.4 for a $45^o$-dipping thrust fault. The fault is located in the UHS model and intersects the free surface. The comparison shows that (a) ground velocities on the vertical component and the strike-perpendicular component are 1 – 2 orders of magnitude larger than those on the strike-parallel component, and (b) illustrates the difference between kinematic (columns 1, 3, and

5) and dynamic (columns 2, 4, and 6) rupture simulations. The time-dependent normal-stress interference of the waves with the free surface causes the amplitudes in the dynamic simulations to be larger, especially for times larger than 6 seconds. Figures 4.5 (including both slip- and sliprate-weakening friction) and 4.6 (no sliprate weakening friction) show RD (top) and RV (bottom) ratios above and surrounding the surface projection of the fault. As expected from the pure thrust rupture mechanism, the vertical and strike-perpendicular components show the largest ratios. Figure 4.5 also depicts ratios for ruptures breaking the surface and buried 1 and 3 km. Note the increase in peak motions around the fault trace for the fault breaking the surface. The largest displacement ratio (3.4) is obtained within a band around the fault tip for the fault with surface rupture, outlined by the contour line for a ratio of 2.5. For faults buried deeper than 1 km the ratios are close to 1, indicating negligible time-dependent free-surface effects.

The discrepancies between prescribed and dynamic rupture are further illustrated by comparisons of the radiated waves. Figure 4.7 shows time-histories for prescribed (thin line) and dynamic simulations (thick line) along the profiles shown in figure 4.2 for a rupture breaking the surface and including slip-weakening but no rate-weakening friction. The dynamic simulation generally generates slightly larger amplitudes. The differences become most obvious on the strike-parallel profile on all traces and components for times larger than 10 seconds, and above the fault (second trace in down-dip profile).

When a small amount of rate-weakening friction (9.2 cm/s) is added, the seismic moments of simulations for all depths decrease (table 3), but the overall pattern of peak displacement ratios and peak velocity ratios show little change as seen from a comparison between figure 4.5 (no rate-weakening friction) and figure 4.6 (including rate-weakening friction). The maximum peak velocity and displacement ratios amount to 1.5 and 3.1, respectively, for the simulation including rate weakening, compared to 1.7 and 3.4, respectively, for the simulation without rate-weakening friction. This change, however, affects only a small area close to the fault edges and does not change the overall pattern significantly. In the following I will therefore only discuss the scenario including slip-weakening friction, but not rate-weakening friction.

Figure 4.8 shows snapshots of the normal stress on the fault plane for a $45^o$-degree dipping thrust fault rupturing the surface (a,b), and buried 1 (c) and 3 km (d) in the UHS model. Simulation (a) has been carried out for a prescribed rupture, simulations (b – d) for a dynamic rupture. Note that for faults buried 1 km and

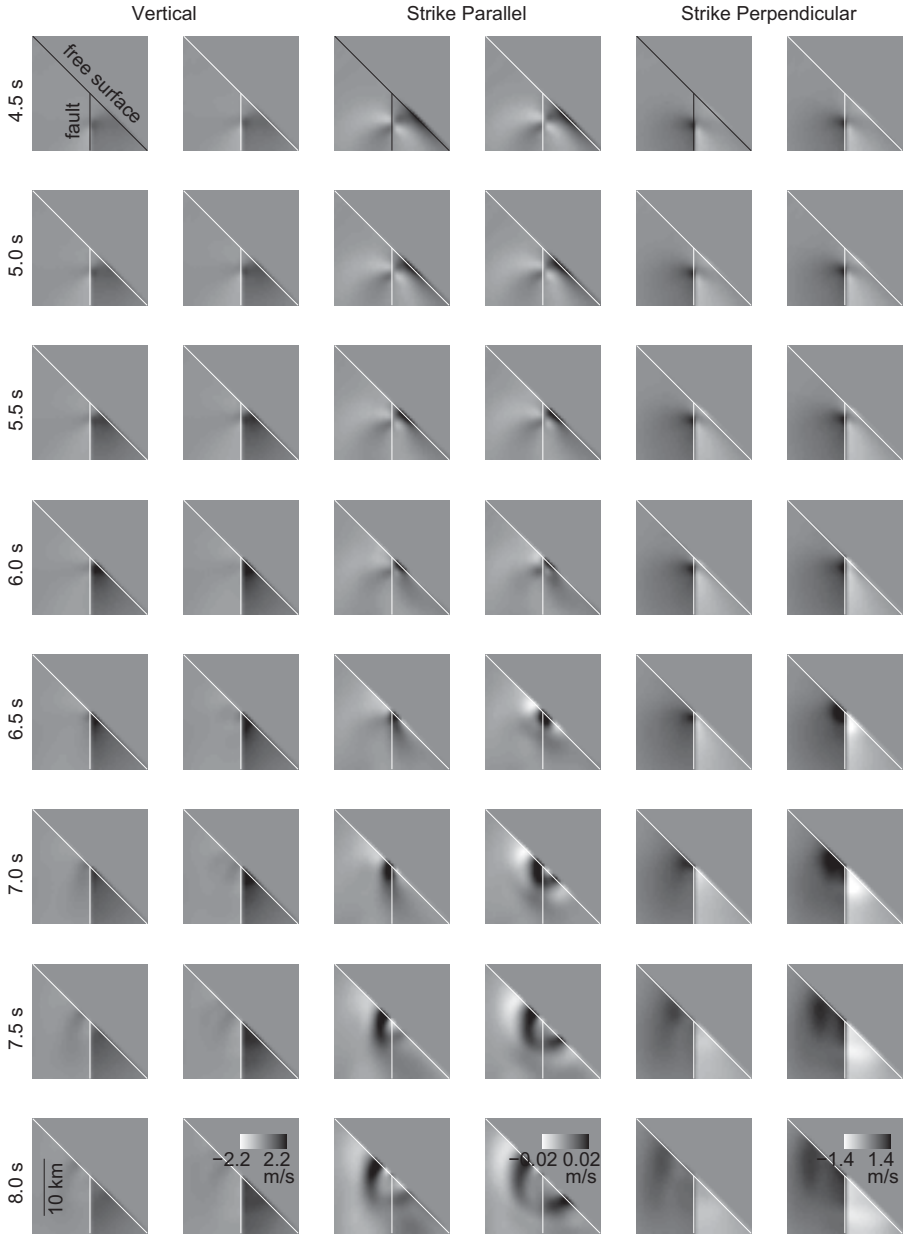


Figure 4.4: *Snapshots of the wavefield vertical to the strike and the free surface for a $45^o$-dipping thrust fault with surface rupture in the UHS model. Columns from left to right: Vertical component of kinematic simulation, vertical component of dynamic simulation, strike parallel component of kinematic simulation, strike parallel component of dynamic simulation, strike perpendicular component of kinematic simulation, strike perpendicular component of dynamic simulation. The dipping black line indicates the free surface. The vertical black line displays the fault. Large positive and negative values are denoted by dark and bright colors, respectively. The scaling of the ground motion amplitudes is done independently for the three components of the wavefield.*

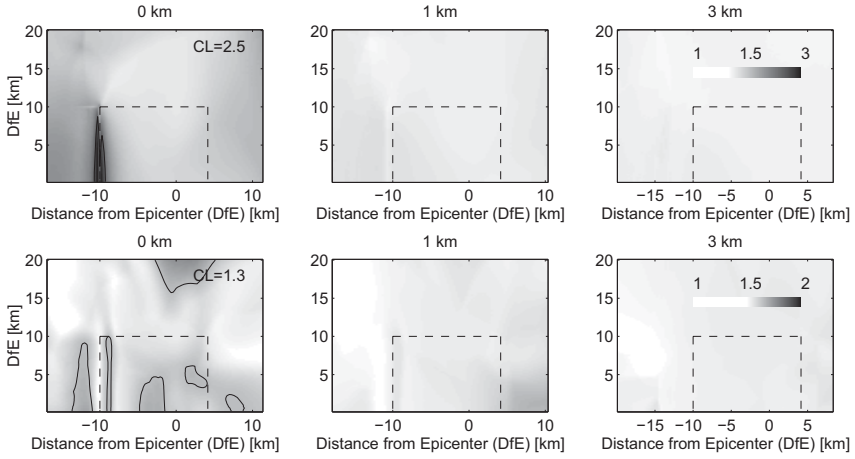


Figure 4.5: *Ratios between peak displacements (top) and peak velocities (bottom) for dynamic and kinematic rupture simulations on a $45^o$-dipping fault with surface rupture, and buried 1 and 3 km. Due to symmetry reasons only the upper half of the area (figure 4.2) is shown. The computations include slip- and sliprate-weakening friction. The projection of the fault onto the surface is shown by the dashed line. Large (small) ratios are depicted by dark (light) colors.*

deeper the stress values approach the surface with constant velocity. Reflected normal stresses do not interfere significantly with the normal stresses on the rupture plane because the faults are buried too deep in the UHS model. For simulations (a) and (b) which both rupture the surface, the reflections of the normal stresses can be seen on the rupture plane. However, significant changes to the circular distribution of normal stresses are only found for the dynamic simulation of the fault rupturing the surface where the reflected normal stresses interfere with the ongoing rupture. The two points moving from the center to the sides are the free surface manifestations of the normal-stress reflections, although in a realistic simulation with variation of the initial stress, these would likely be much less significant.

Figure 4.9 shows the sliprate for dynamic simulations, rupturing the surface (a) and buried 0.5 (b) and 1 km (c). Note the break-out phase for (a) and (b), which disappears for faults buried 1 km and deeper. This phase consists of a transition to super-shear rupture velocity due to decreased rupture resistance in the presence of the free surface. It causes a significant increase in ground motion above the fault [97, 98, 99].

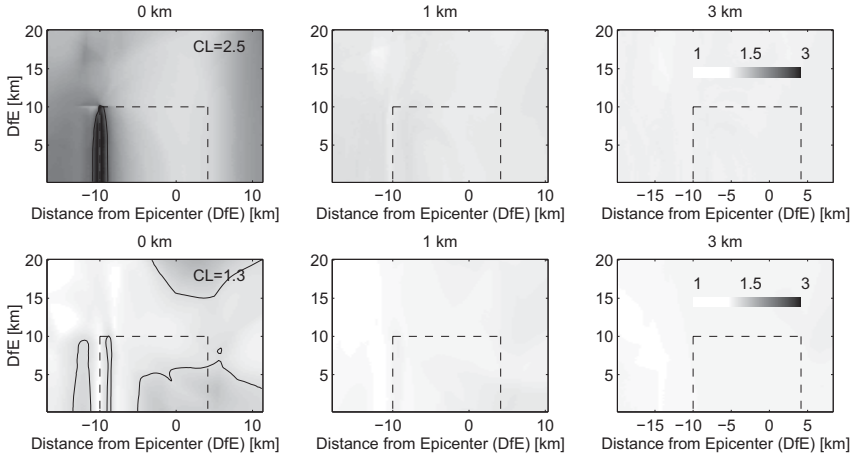


Figure 4.6: *Same as figure 4.5, except the dynamic simulations include only slip-weakening friction.*

### $30^o$ and $60^o$ Dipping Thrust Faults

Figures 4.10 and 4.11 depict peak displacement and peak velocity ratios for $30^o$- and $60^o$-dipping thrust faults, respectively. As for the $45^o$-degree dipping fault plane, the peak ratios are increased around the fault trace. The ratio reaches factors of 3.3 and 4.7 for the $30^o$- and $60^o$-dipping faults. The influence of the different dip angles is further illustrated in figure 4.12 (left) which shows the sliprate on the fault for three dynamic simulations, with a dip angle of $45^o$, $30^o$, and $60^o$. For a $30^o$-dipping fault the interaction with the free surface occurs earlier and for the $60^o$ dip later than for the $45^o$ simulation. The average final slip value and therefore the moments are similar for the $30^o$- and $45^o$-dipping faults (table 4.4). For depths less than 5 km, the final slip is on average larger for the $60^o$-dipping fault which is reflected in increased seismic moments compared to those on the $45^o$-dipping thrust fault (table 4.4).

## 4.3.2 Layered Model, $45^o$ Dipping Thrust Fault

Figure 4.12 (right) shows the sliprate for a $45^o$-dipping dynamic fault model with surface rupture and one (1LOH) and two (2LOH) near-surface layers added to the UHS model described above (see table 4.1). Note how the layers promote an earlier transition to super-shear rupture, which causes an additional increase in peak motion compared to the equivalent kinematic case.

A comparison of time-histories from dynamic and prescribed ruptures along the

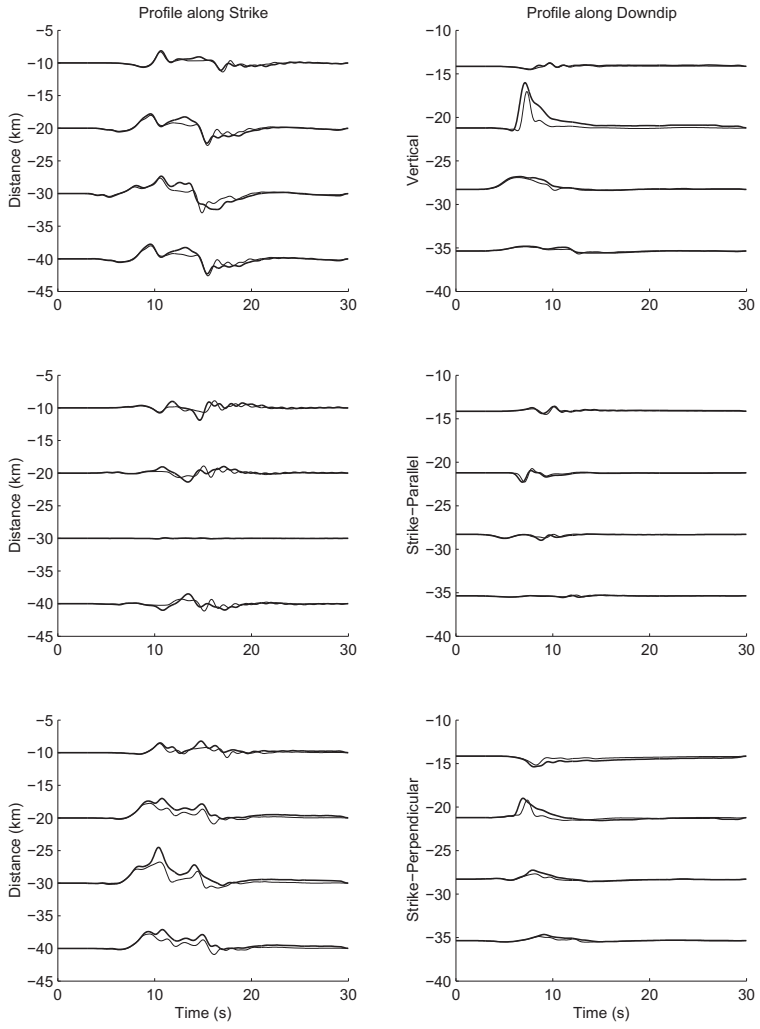


Figure 4.7: *Velocity seismograms for a $45^o$-dipping thrust fault with surface rupture in the UHS model along profiles P – P' and Q – Q' (figure 4.2). The thick and thin traces depict synthetics from dynamic and kinematic simulations, respectively. Note the large differences for times larger than 10 seconds, in particular on the profile along strike (P – P' in figure 4.2)*

profiles P – P' and Q – Q' in figure 4.2 is shown in figures 4.13 to 4.16 for models 1LOH and 2LOH, respectively. Between 20 and 30 seconds, the strike-perpendicular component of the dynamic simulations generate peak motions 2 – 3 times larger than those for the prescribed rupture along the strike-parallel profile for the 1LOH model. This is likely caused by reverberations of the waves in the 1-km thick surface layer with a resonance period of 4 seconds, in agreement with the predominant period of the waves in the records, enhanced significantly by dynamic normal-stress effects between the free surface/layer interfaces and the fault plane. Note also the factor of 9 and 5 increase of the vertical-component peak motion for the 1LOH and 2LOH models, respectively, at the fault tip along the down-dip profile (-21 km). For the UHS, 1LOH and 2LOH models (figure 4.7) the peak kinematic velocity reaches 80%, 22% and 12% of the dynamic peak value.

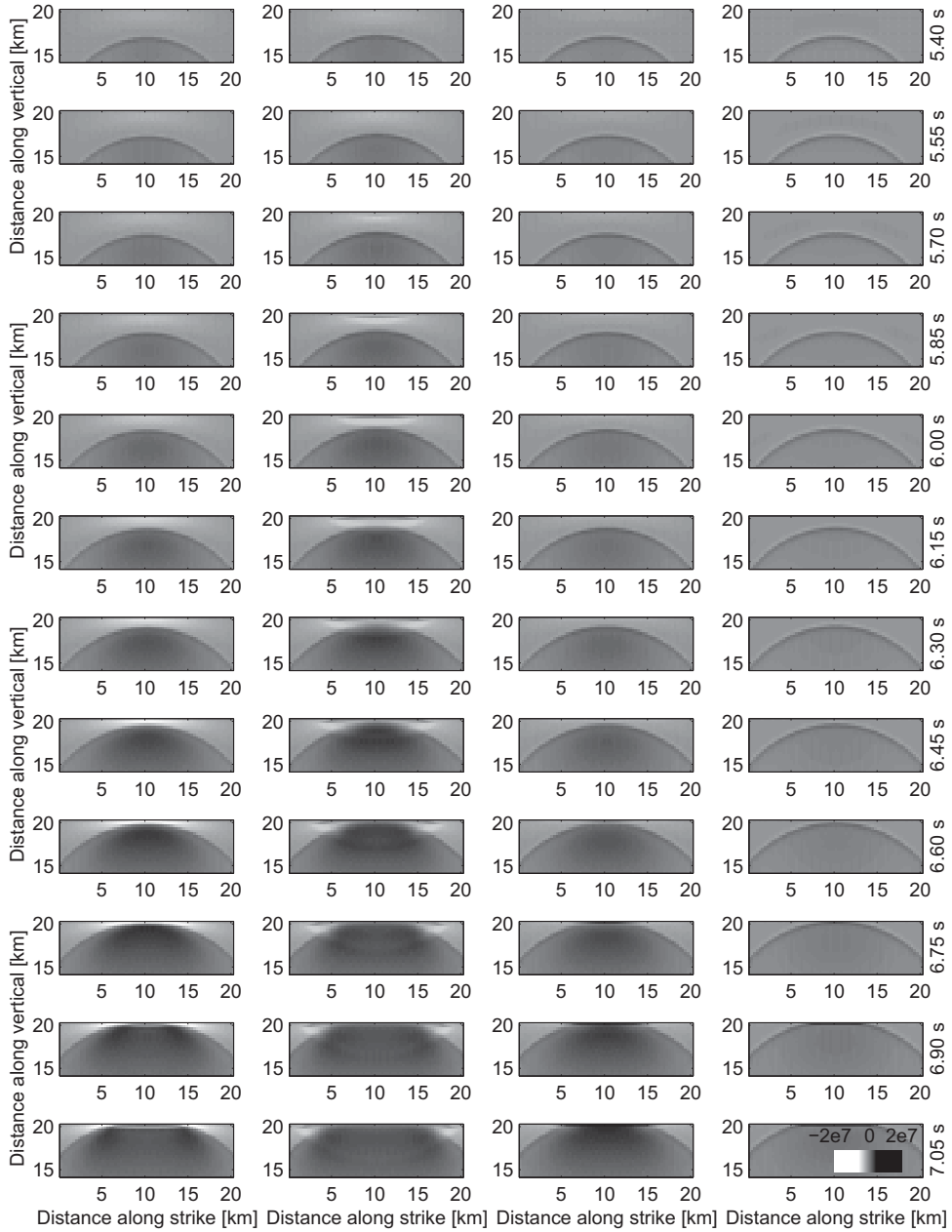


Figure 4.8: *Snapshots of normal stress on the fault plane for a* $45^o$*-degree dipping thrust fault with surface rupture (column* a and b), and buried 1 and 3 km in the UHS model (column c and d). Simulation a is obtained from a prescribed rupture, simulations b – d from dynamic simulations. Note the significant disruption of the circular distribution of normal stresses for prescribed rupture a compared to that for dynamic rupture b. For faults buried 1 km or deeper the free surface has negligible effect on the distribution of normal stresses for the frequencies considered in this simulation.

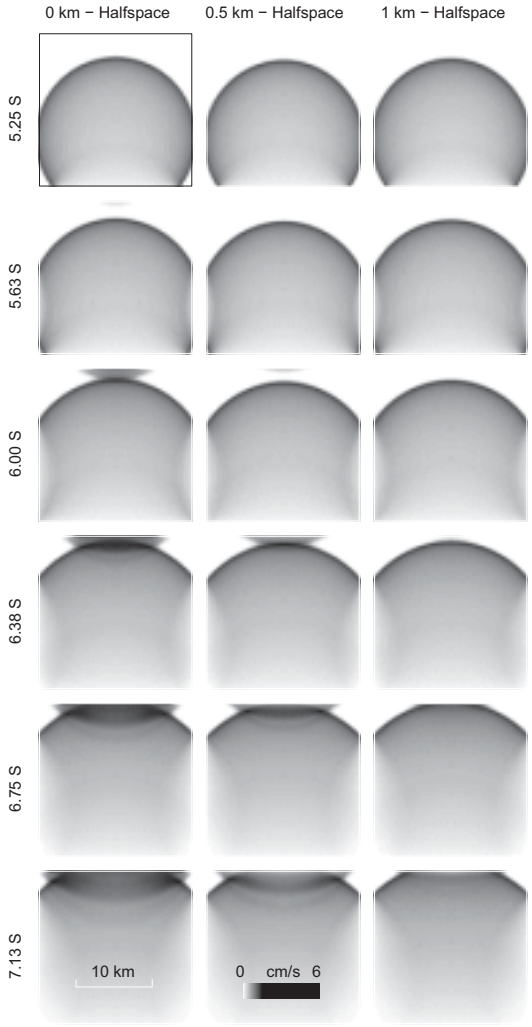


Figure 4.9: *Snapshots of the sliprate on a $45^o$-dipping fault with surface rupture in the UHS model (left column), buried 0.5 (middle column) and 1 km (right column). Note the break-out phase which first appears at 5.63 seconds after the rupture initiation in the simulation where the fault breaks the surface (left column). Here, the rupture jumps to the surface. The fault plane is then ruptured from the surface downwards. The break-out phase is less significant on a rupture plane buried 0.5 km deep and disappears when the fault is buried at least 1 km for the frequency content considered.*

Figures 4.15 and 4.16 show similar comparisons between time-histories from dynamic and prescribed ruptures for the UHS, 1LOH (left) and 2LOH (right) models. The peak displacement and velocity ratios are considerably larger in the layered models (figure 4.17). As for the UHS model, the largest ratios are observed close to the fault tip. Here, the maximum displacements and velocities reach 5.6 and 9.7, respectively, in the two-layer model and 4.3 and 10.3, respectively, in the three-layer model, on the strike-perpendicular and vertical components. The increased peak displacement and peak velocity ratios are additionally observed by the increase of the seismic moment (table 4.5). The time-dependent normal-stress interaction generates an increase in slip on the fault and seismic moments exceeding that of the equivalent simulation in the UHS model by 10% (1LOH) and 16% (2LOH).

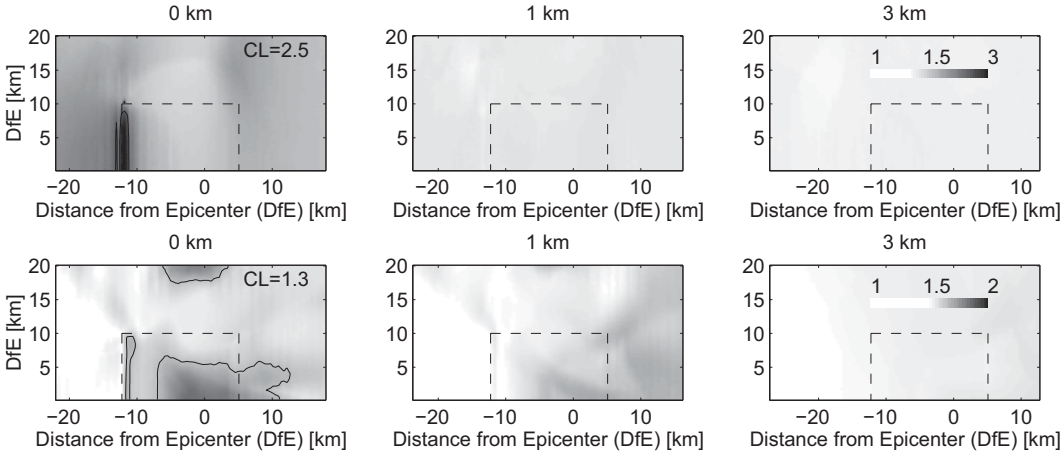


Figure 4.10: *Same as figure 4.6, except the dip of the fault is* $30^o$.

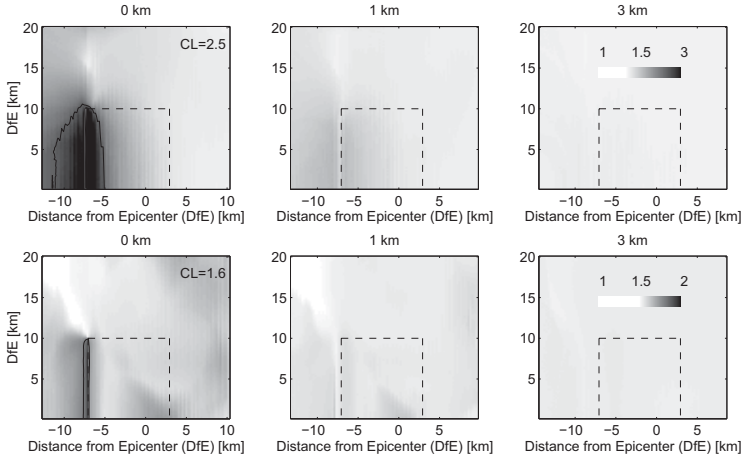


Figure 4.11: *Same as figure 4.6, except the dip of the fault is* $60^o$.

### 4.3.3 Variation of Initial Stress Distribution

As seen above, dynamically computed ground motion from dipping faults rupturing the surface shows remarkable differences to ground motion computed for prescribed ruptures. The differences get smaller for faults buried one kilometer and deeper. In the following I will investigate which part of the rupture plane of the surface rupture is responsible for the increase in peak motion in the dynamic case.

Three different stress distributions are implemented on a $45^o$ dipping thrust fault that breaks the surface. Figure 4.18 (a) shows the initial stress distribution on the fault for the first scenario. In contrast to the previous computations where the initial stress was constant at 17.5 MPa on the fault, here the stress values are tapered to

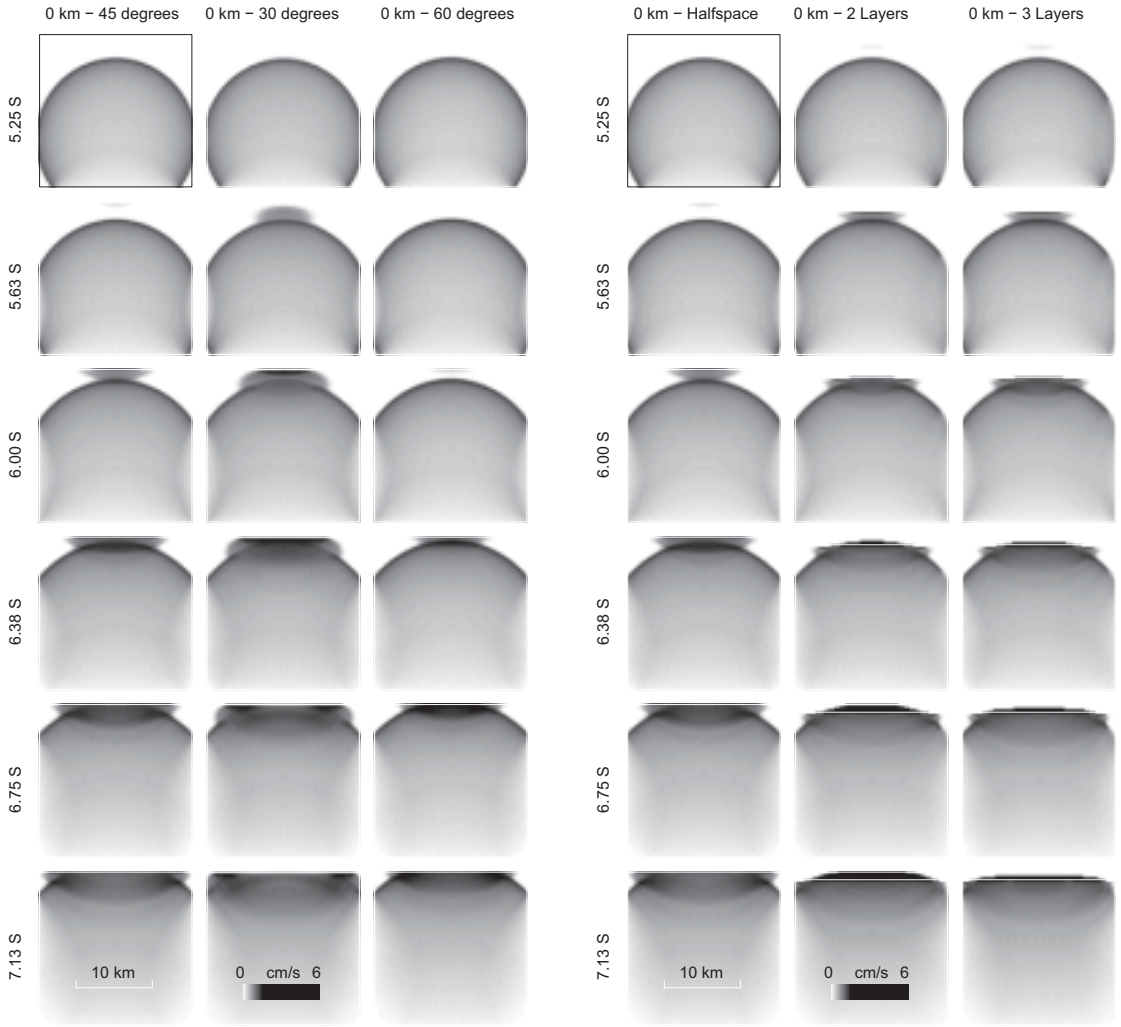


Figure 4.12: *Left: Snapshots of the sliprate in the UHS model on faults with surface rupture and dips of* $45^o$ *(left column),* $30^o$ *(middle column) and* $60^o$ *(right column). Note the earlier normal-stress effects for the shallower compared to those for the deeper fault plane. Right: Snapshots of the sliprate on a* $45^o$*-dipping fault with surface rupture in the UHS (left column), 1LOH (middle column) and the 2LOH (right column) models. Note that the break-out phase is initiated earlier in the 1LOH and 2LOH models compared to the UHS model.*

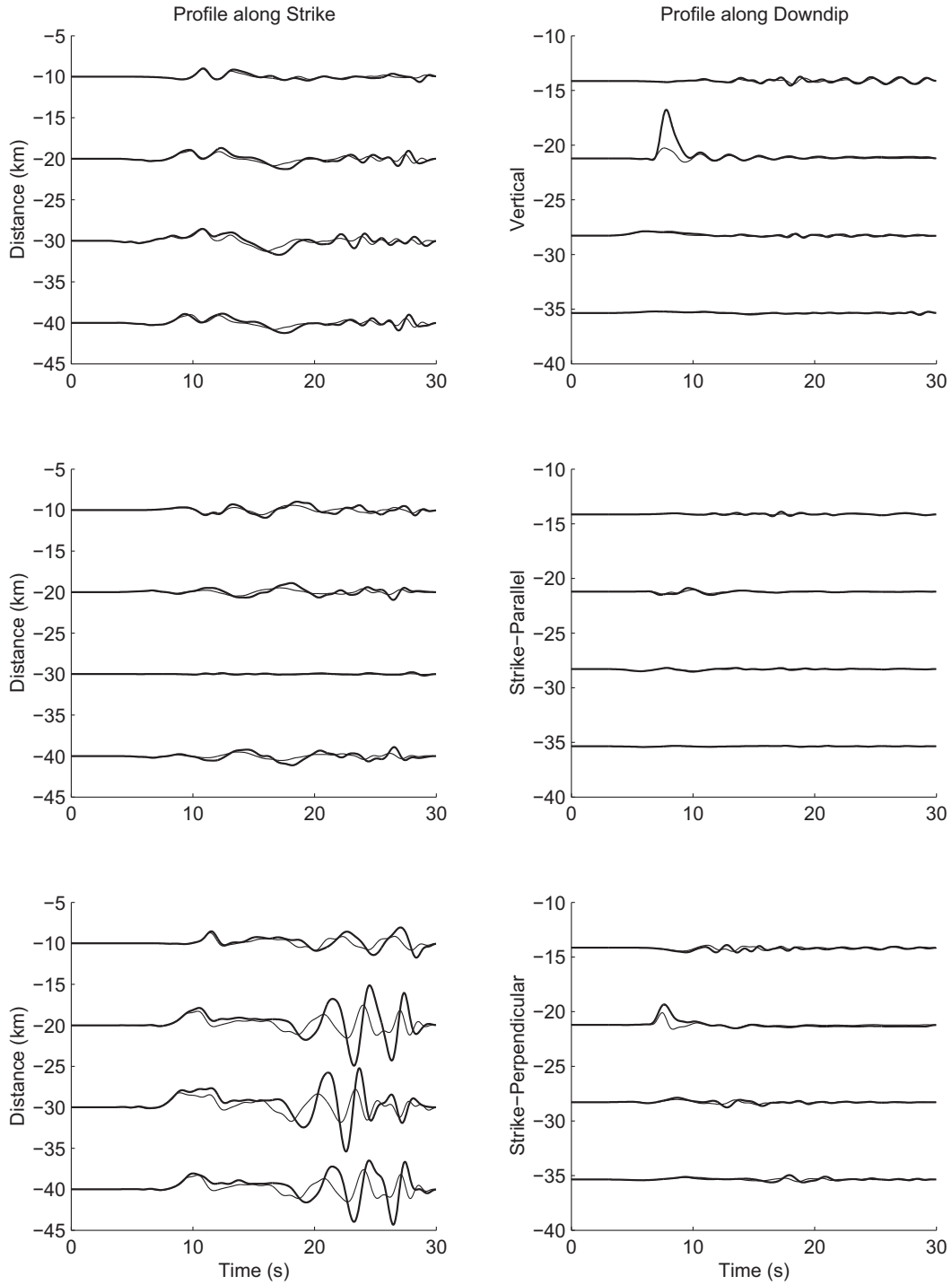


Figure 4.13: *Velocity seismograms along profiles P – P' and Q – Q' (figure 4.2) for a 45$^o$-dipping thrust fault with surface rupture in the 1LOH model. The thick and thin traces depict dynamic and prescribed rupture results, respectively. The largest differences occur for times larger than 20 seconds on the profile along strike along profile P – P' (figure 4.2).*

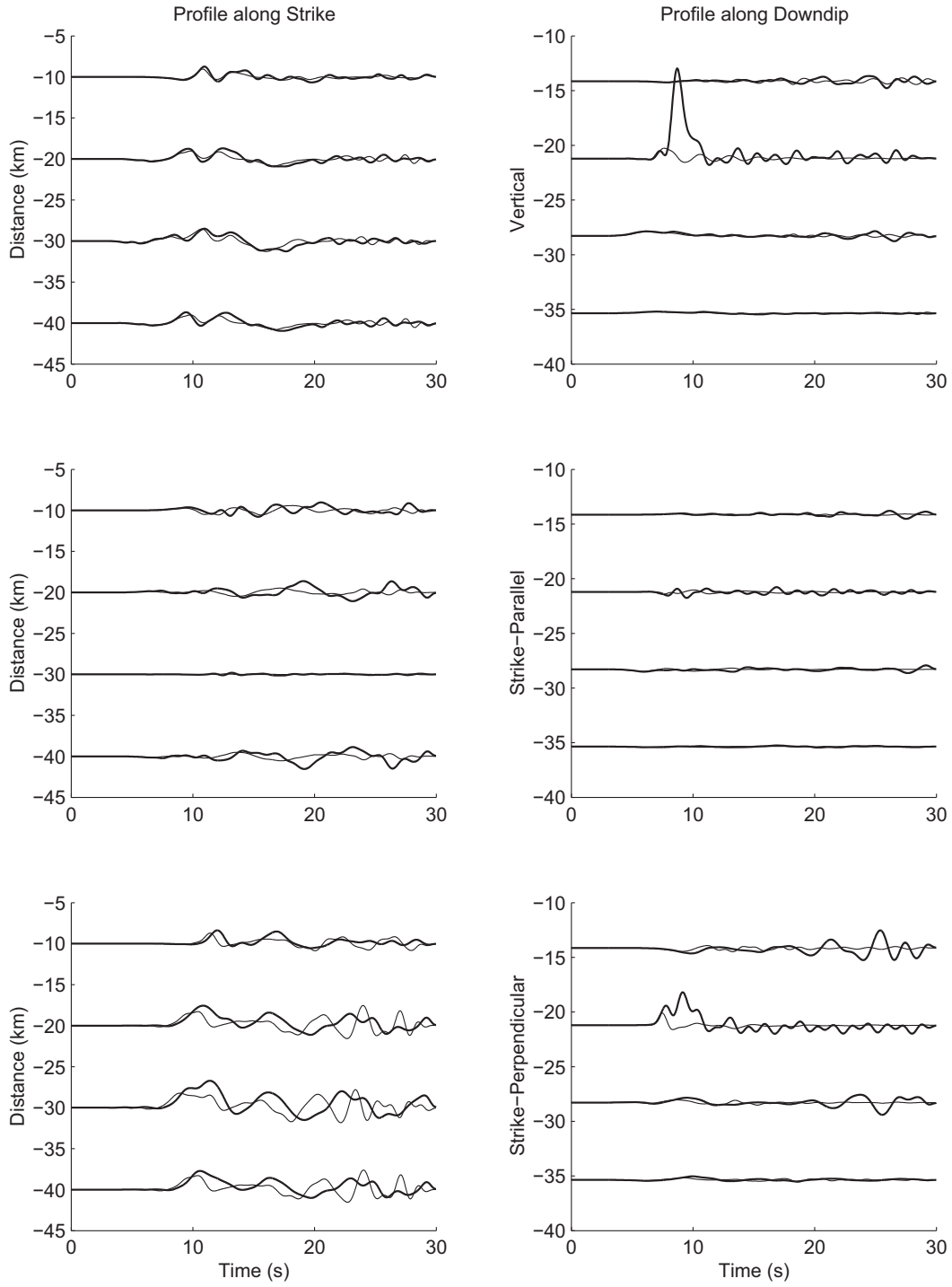


Figure 4.14: *Same as figure 4.13, except that the seismograms are computed for the 2LOH model.*

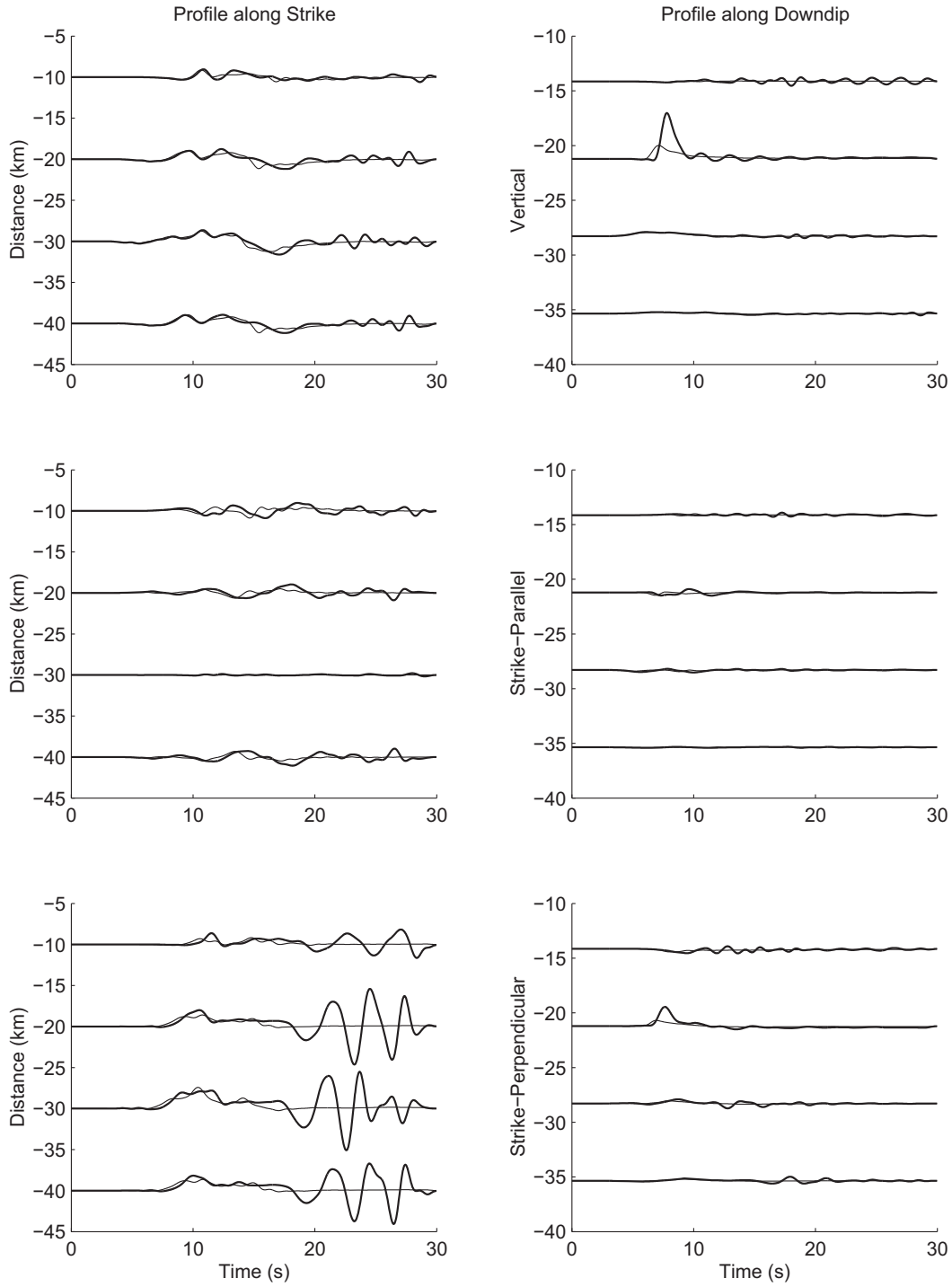


Figure 4.15: *Same as figure 4.13, except the thin line depicts the results from dynamic simulation in the UHS model. Note the lack of significant reverberations for times larger than 20 sec in the UHS model.*

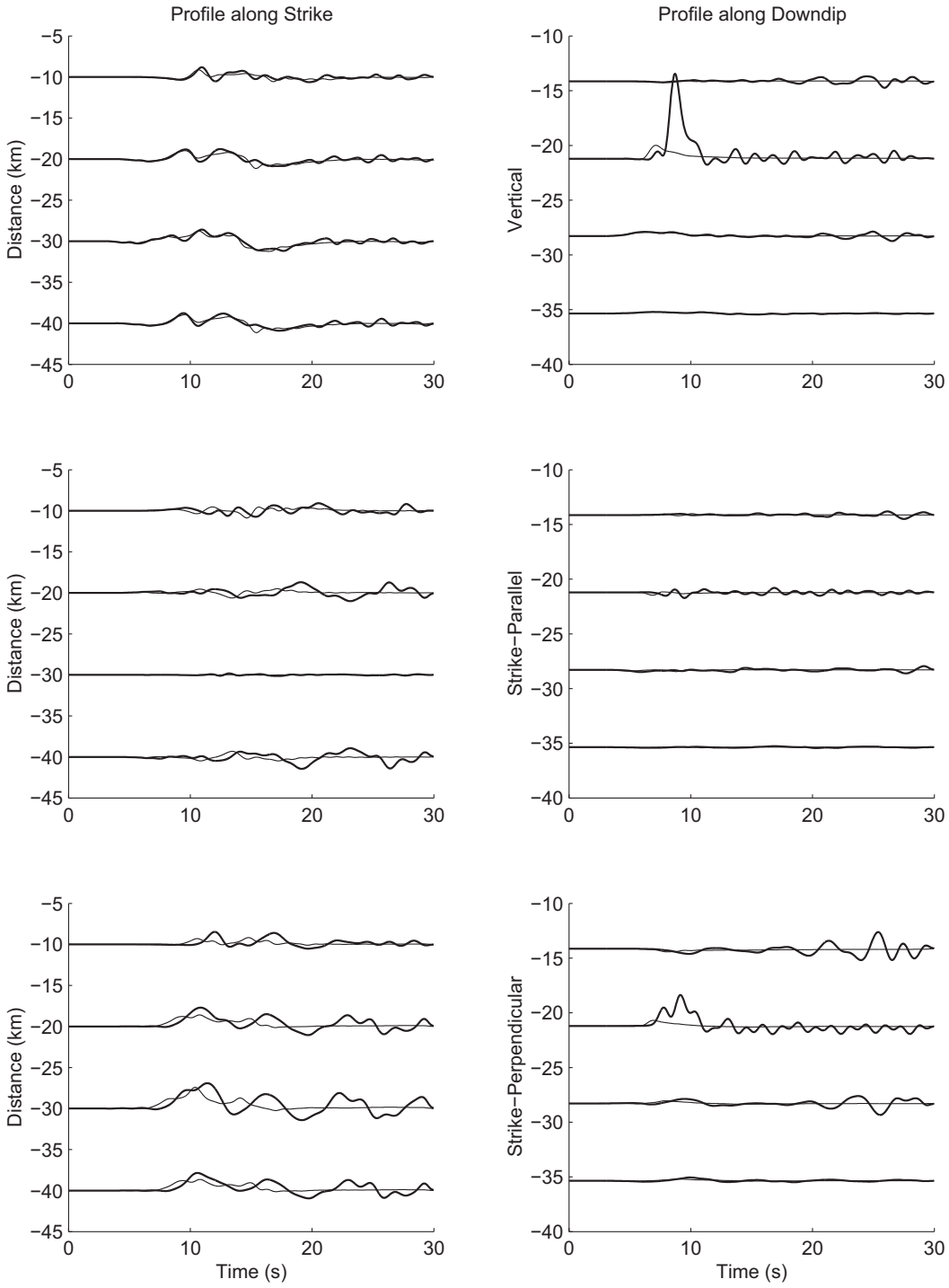


Figure 4.16: *Same as figure 4.14, except the thin line depicts the results from dynamic simulation in the UHS model.*

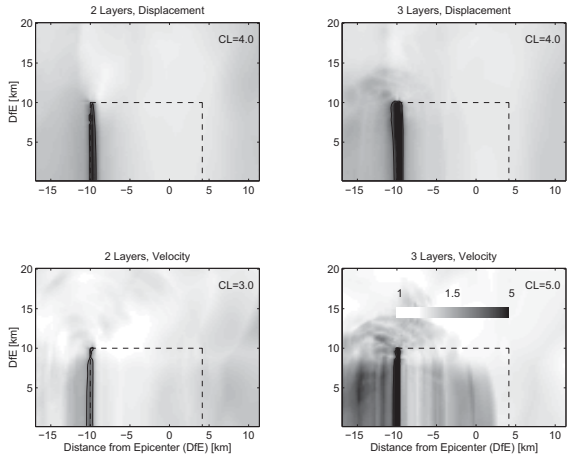


Figure 4.17: *Ratios between peak displacements (top) and peak velocities (bottom) from dynamic and prescribed rupture on a 45$^o$-dipping fault with surface rupture for the 1LOH (left column) and 2LOH models (right column). Due to symmetry reasons only the upper half of the area in figure 4.2 is shown. The dynamic simulations include no velocity-weakening friction. The projection of the fault onto the surface is indicated by the dashed line.*

zero with a square-root law in the outer two kilometers of the fault on all four sides. This results in an average prestress value of 15.4 MPa or almost 88 % of the constant stress model. For the second test, the stress values are tapered on the sides and the bottom of the fault, but set constantly to zero in the upper two kilometers of the fault plane (figure 4.18 (b)). Like that the average initial stress on the fault plane amounts to 14.3 MPa or 81.5% of the constant stress model. The third test (figure 4.18 (c)) shows a checker-board pattern in the upper kilometer where 1 km long patches with initial stress equals zero alternate with patches with constant stress of 17.5 MPa as on the rest of the fault. This pattern results in an average initial stress on the fault of 17.1 MPa or 97.6 % of the constant stress model.

The seismic moments obtained from dynamic simulations for these scenarios amount to 4.88 $\cdot 10^{19}$ Nm for scenario (a), 4.35 $\cdot 10^{19}$ Nm for scenario (b) and 5.24 $\cdot 10^{19}$ Nm for (c) (see also table 4.5). With only 81.8 % of the seismic moment of the constant stress model described above ($M_0 = 5.32 \cdot 10^{19}$ Nm), scenario (b) shows the largest decrease of the seismic moment. This decrease is however of the same order as the decrease in the initial stress. Scenario (a) where the areas of decreased stress are equally distributed on all sides of the rupture plane results in a moment of 91.7 % and thus a larger moment as expected with an average prestress of only less than 88 %. For the checker-board model the seismic moment amounts to 98.5 % of the

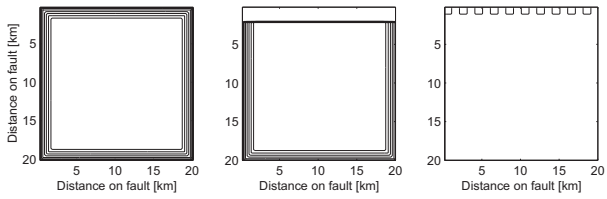


Figure 4.18: *Initial stress distributions on the fault for a simulation (a) where the prestress is tapered to zero in the outer two kilometers of the fault, (b) same as (a) but where the prestress in the upper two kilometers is zero, and (c) with a checker-board distribution of the prestress in the upper kilometer.*

moment from the model with the constant initial stress. Here, as in model (b) the main changes have been applied on the upper edge of the rupture plane. I therefore conclude that the stress distribution in the uppermost 1 or 2 kilometers has the largest effect on the dynamics, and that heterogeneous stress distributions in deeper parts of the fault would not change the results significantly.

### 4.3.4 Deeper Versus Shallower Events

Recently, a systematic difference in the level of earthquake ground motions for three $M_W$ 7.2 – 7.6 earthquakes with large surface ruptures, and three $M_W$ 6.7 – 7.0 earthquakes on buried faults was found [129]. Acceleration spectra of the smaller events were in those cases much larger than the 1994 Uniform Building Code (UBC) spectrum for soil site conditions in the intermediate period range of 0.5 – 2.5 seconds, but similar to the UCB code spectrum at longer periods. This is in contrast to all current models of earthquake source and ground motion spectral scaling with magnitude. I use the dynamic results for different depths to test the results.
Figure 4.19 shows acceleration response spectra for three sites along profile R – R' in figure 4.2. I compare a $45^o$-dipping 5 km buried thrust fault (dashed lines) to a $30^o$-dipping fault that breaks the surface (solid lines). The seismic moments of the two dynamic simulations amount to $3.4{\cdot}10^{19}$ Nm in the first, and $5.3{\cdot}10^{19}$ Nm in the latter case. The increased seismic moment in the latter case is due to the interaction of the wavefield with the free surface as mentioned above, and is reflected in an increased moment magnitude from $M_W$ 7.0 for the buried fault to $M_W$ 7.1 in the fault with the surface rupture. The spectra show larger amplitudes for all periods between 0.33 and 5 seconds for the rupture breaking the surface (solid line) in comparison to the buried rupture (dashed line). Thus, the dynamic simulations can not confirm

the observations. The increased spectral accelerations [129] are not a first-order dynamic effect from the depth of burial of the fault. Instead, the effect may be caused by a shift in frequency content for the two scenarios, with a larger amount of long-period energy generated from the larger Chi-Chi earthquake. A contributing cause could be the change of rake angle during the Chi-Chi earthquake, deviating from the pure thrust mechanism used here. Finally, variation in crustal structure for the two events, e.g., the presence of the San Fernando Valley sedimentary basin above the Northridge earthquake, may have generated some of the discrepancies.

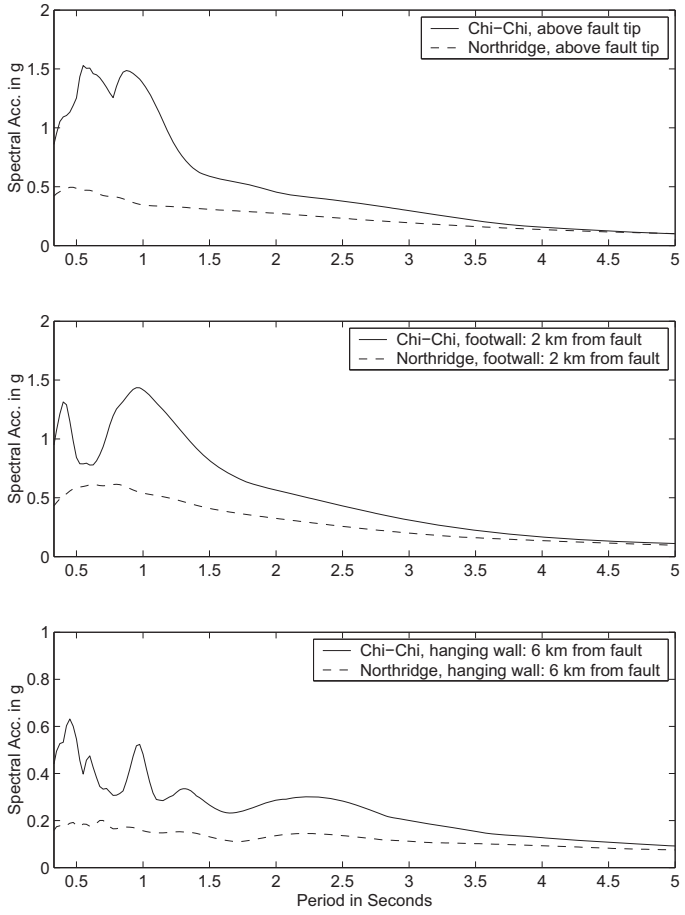


Figure 4.19: *Acceleration response spectra for a $M_W$ 7.0 event on a $45^o$-dipping fault buried at 5 km depth (dashed line) and for a $M_W$ 7.1 event on a $30^o$ fault with surface rupture (solid line) at 3 sites (see figure 4.2)*

## 4.4 Discussion

A primary incentive to outline the first-order effects of dynamic time-dependent normal-stress effects on ground motions is to define possible recommendations to improve ground motion computed from prescribed rupture simulations. This issue is

addressed using halfspace and layered models with simple initial stress distributions and friction laws uniform across the fault plane. The results indicate that such effects almost entirely originate in the 1 – 2 km of the fault plane closest to the surface. However, the frictional and stress conditions in this region are probably more uncertain than in any other region of the fault. For example, it is possible that the slip/sliprate weakening friction assumed in this study may really be frictional strengthening in the near-surface region of the fault. Unfortunately, practically no evidence exists to support any specific alternative frictional model. Future research should focus on estimating the nature of the friction and stress conditions in the near-surface low-impedance material.

A potentially important practical application of this study is the inclusion of the results in conventional ground motion estimates for hazard assessment. For example, although dynamic simulations may be more physically correct, it is always possible to implement a prescribed rupture generating similar ground motion. A viable method would be to include a parametric model of the normal-stress effects on the ground motions in attenuation relations. For example, such an improvement of existing attenuation relations was proposed for including rupture directivity effect [130]. Before such a model can be generated, the results need to be verified against observational data. However, few historical thrust earthquakes on dipping faults with surface rupture have provided a distribution of seismic data with a quality and density around the tip of the fault sufficient for such a validation. Probably the best candidate for such a test is the 1999 $M_W$ 7.6 Chi-Chi, Taiwan, earthquake. Future work should use this kind of data to verify the results obtained in this study.

# Summary

In this thesis, three approaches for a better estimation of the seismic hazard imposed by earthquakes are presented. Seismic hazard estimation is a very promising field of research and gained increasing public and scientific interest in recent years. The quantification of seismic hazard is a necessity for defining building codes and a first and most essential step for saving lifes during future large earthquakes. The three approaches in this thesis are presented as case studies, all making use of a Finite Difference (FD) method, a tool very popular and widely used for forward modeling the seismic wavefield (e.g. [44, 49, 52, 66, 73, 84, 103, 132, 134, 135]).

The first case study, presented in chapter 2, examines the usability of a first-order subsurface model of elastic parameters for high-frequency (1 Hz $\leq$ f $\leq$ 8 Hz) hazard assessment investigations for the Rhinegraben (Germany). The frequency range from 1–8 Hz is considered to be most significant for the estimation of the seismic hazard of south-west Germany as most buildings in this region have eigenfrequencies in this range. So far, 3D FD simulations have been restricted to frequencies below 1–1.5 Hz due to both, the limited knowledge of the subsurface geological structure and computational drawbacks. While the latter will presumably be solved in the near future, the refinement of existing geological models is considered to be a long-term process. For an exact simulation of the seismic wavefield, the subsurface structure needs to be known down to the scale of at least one wavelength. In an isotropic medium, FD methods require the knowledge of two elastic moduli (e.g. the two Lamé constants $\mu$ and $\lambda$ or the seismic velocities $v_p$ and $v_s$) and the rock density $\rho$ at every point of the computational grid in order to solve the wave-equation numerically. Presuming a minimum shear wave velocity of 2 km/s as proposed for the Rhinegraben by recent refraction and reflection studies [61, 112, 143], the minimum wavelength included in the simulation amounts to 250 meters. From borehole and surface measurements [55, 142] even lower shear wave velocities are reported for the upper several hundred meters. The model of elastic parameters available for the Rhinegraben is not accurate enough to resolve such small-scale features. For

seismic hazard assessment, however, a wiggle-by-wiggle simulation of the wavefield is not needed. Instead, it is considered to be sufficient when peak amplitudes of ground motions or response spectral values are simulated as they are responsible for a major part of the destruction. The investigation in chapter 2 tests whether these parameters can be simulated within reasonable limits in order to be used for the estimation of the seismic hazard of the Rhinegraben. This is done by a comparison of ground-motion derived from 2D simulations of three $M_L$ 3.5–3.6 Rhinegraben earthquakes and data recorded at three seismic stations in the Rhinegraben (stations FBB, LIBD, and BBS), one station in the Vosges mountains (MOF), and one station in the Black Forest (FBB). Five comparisons are performed: First, the arrival times of the compressional waves are compared in order to get a general idea about the quality of the elastic model for the purpose of hazard assessment. The comparsions show a large variability of the results, from only $\pm$ 0.1 seconds deviation at three stations (LIBD, BBS and FBB) for event 1, a $M_L$ 3.5 earthquake originating from Dessenheim (France) on August 24, 1996, to a maximum difference of 1.2 seconds at station FELD for event 3, a $M_L$ 3.5 event that occured close to Weil am Rhein (Germany) on November 17, 1997. Furthermore, a comparison of peak ground velocities (PGV's) is performed. PGV's are a crucial parameter for seismic hazard assessment as they give an estimate of the maximum load during an earthquake. Both, over- and underestimation of the data by the synthetics is found. In most cases, the deviations amount to not more than a factor of 2–3. In these cases the simulations are considered to be usable for hazard assessment. The precision of magnitude estimations for historic earthquakes that enter hazard computations as well leads to ground motion uncertainties in the same order of magnitude. Some of the seismograms analyzed in chapter 2, however, show differences of a factor of 10 between peak velocities of data and synthetics. This discrepancy is too large and signifies that it is critical to use the time-histories computed by the FD method for hazard assessment of the area. The same observation is made for the other comparisons carried out in chapter 2. Both, the duration of shaking during an earthquake, defined as the time between 5 % and 75 % of the cumulative squared ground acceleration [130], and the amplitudes of spectral responses can be simulated in most cases within a factor of 2–3, a value still acceptable for seismic hazard assessment. The exceedance of this factor in several other examples however, leads to errors too large for a reliable estimation of seismic hazard. Possible explanations for the deviations between data and synthetics are then discussed in chapter 2: In order to test the influence of local site effects on the ground motion amplitudes,

P/S wave amplitude ratios are compared. The local ground composition at the five seismometer sites which in many conditions affects compressional and shear wave amplitudes in the same way is not taken into account in the elastic model used for the FD simulations. A comparison of compressional wave to shear wave amplitudes for data and synthetics should give the same values if the site conditions were similar for both wave types and if they were responsible for the differences in ground motion amplitudes. This is not the case. Another possible explanation could be the neglection of material attenuation in the FD simulations. In a similar study [46] for epicentral distances between 40 and 60 kilometers material attenuation could account for a maximum decrease of 22% of the amplitudes. In some cases this would lead to a better estimate, in other cases, where the amplitudes of the synthetics take values below those of the data, the fits would get worse. The disregarding of topography in the FD simulations can not explain the poor fit in some of the simulations either. Both, arrival times and wave amplitudes would be affected when topography is taken into account. Another possibility for the discrepancies could be an inaccurate determination of source parameters of the three earthquakes. The source parameter with the smallest fidelity [131] is the hypocentral depth. The values determined by the Federal Geological Survey have error margins of up to 5 kilometers. Ground motion amplitudes from earthquakes with hypocenters at 10 and 15 kilometers differed by a factor of 2 in a pilot study [47]. While all those possibilities can only account for a small portion of the misfit, the most satisfactory explanation seems to be that the model of elastic parameters is not precise enough to simulate ground motion amplitudes with the accuracy required for the purpose of hazard assessment. It is therefore suggested to conduct high-resolution seismic experiments in the area in order to refine the elastic model, and to deploy three-component permanent seismometers in the Rhinegraben for better data quality.

Effects of rupture physics and the influence of a sedimentary basin structure on ground motion amplitudes are studied in a second case study, shown in chapter 3. Both these two effects are not taken into account in simple radial attenuation laws [3, 6, 21, 22, 68, 117] as generally used for the prediction of ground motion for seismic hazard estimations. The simulations in chapter 3 quantify both effects and show that for large earthquakes (e.g. $M_L > 6.0$) and for heterogeneous subsurface structures the two effects play a crucial role for the distribution ground motion amplitudes. The issue is addressed by simulating ground motion for a $M_L$ 6.2 earthquake in a simple basin model [5, 37]. The simulations reconstruct a historic event that happened on July 11, 1927, close to the city of Jericho (Israel) at the northern

edge of the Dead Sea Basin. This event is the youngest in a history of large ($M_L >$ 6.0) earthquakes connected to the seismicity of the Dead Sea Rift that dates back more than 4000 years, and the only one for which precise information on source parameters and damage distribution are available [96, 123, 127]. The macroseismic intensity map for this event shows a distinct extension of large intensities to the north with the largest intensity (X) observed approximately 50 kilometers north of the epicenter [127]. Two further areas with intensity level VIII–IX are located about 100 kilometers north of the epicenter. This deviation from a radial shaped damage ground motion distribution has also been reported for several other events in the area [127, 141]. As a possible explanation for this distribution it has been suggested that the Dead Sea Basin substructure might act as a wave-guide [140]. The simulations in chapter 3 verify this assumption but additionally point out the influence of rupture physics on the ground motion amplitudes. The investigation includes the analysis of snapshots of the wavefield at the surface, velocity seismograms at selected sites situated in the basin and on bedrock, the computation of peak ground velocities as well as 1-Hz pseudo-accelerations ($Y_{FD1}$). The latter are compared to pseudo-accelerations computed in an elastic halfspace model ($Y_{FD2}$), and from an attenuation relation ($Y_{AR}$) similar to the one that is integrated in the building code 413 of Israel, respectively. The analysis of the ratios $R_{FD} = Y_{FD1}/Y_{FD2}$ and $R_{AR} = Y_{FD1}/Y_{AR}$ explains the divergence from radially distributed ground motion amplitudes and divides the causes into two groups: $R_{FD}$ isolates ground motion amplification due to the subsurface model as the model of elastic parameters is the only difference between the two FD simulations. All other rupture parameters are kept constant. In contrast, the computation of $R_{AR}$ provides indications for ground motion amplification due to the rupture process. In the computation of $Y_{AR}$ rupture physics is not taken into account. The values of $R_{AR}$ can also be increased by reflections from the basin edges since the computation of reflections is not taken into consideration in the attenuation relation. $R_{AR}$ is generally small south of the epicenter (with amplifications below a factor of 2) and gradually increases towards the north. The largest ratio which is due to reflected waves that increase the amplitudes in the FD simulations are found at the edge of the basin ($R_{AR} = 5.1$). Rupture dynamics is considered as explanation for the increase of $R_{AR}$ taking values of 2.0–2.5 in the area close to the source. Increased values of $R_{FD}$ are found in areas comprising the basin where the amplification is on the order of 4. The largest amplification with $R_{FD} = 5.1$ is again due to reflected waves and can be found at the northern end of the basin. The simulations in chapter 3 show (a) the significant influence

of the basin substructure on the distribution of ground motions and (b) that this effect is larger than the effect due to source physics. This pattern, however, might be reversed when earthquakes with larger magnitudes and thus larger rupture areas [138] are taken into consideration.

Ground motion from earthquakes on dipping faults is analyzed in chapter 4 in a third case study. In the near-field of the earthquake, the ground motion distribution from faults dipping at angles $\neq 90^o$ is often found to be asymmetric, with larger values on the hanging wall, and smaller values on the footwall. This effect is due to the dynamic interaction of the stresses on the fault with the free surface and is not yet fully understood. It is most prominent for shallow faults, and depends on the dipping angle. Scenario earthquake simulations which are becoming more and more popular for seismic hazard assessment, generally do not include these dynamic effects but make use of a prescribed source implementation where the sliprate on the fault is defined a priori and can not develop during the rupture process due to dynamic interactions. For numerical and computational difficulties it is not very likely that a majority of FD simulations will make use of dynamic ruptures in the near future. It is therefore very instructive to investigate the dynamic effects for faults buried at different depths and dipping with different angles in order to find a threshold depth after which the dynamic effects become negligible. In chapter 4, ground motion from faults buried 0.5 km, 1 km, 3 km and 5 km deep in a halfspace model, and from a rupture breaking the surface is computed. Additional computations have been carried out in a model with one and two layers over the same halfspace. Ground motions and stress distributions at the surface and in vertical cross-sections of the model are visualized. As a verification of previous studies [2, 24, 28, 30, 54, 67, 82, 97] it is shown, that the heterogeneous distribution of ground motion amplitudes is due to dynamic interaction of the normal stresses with the free surface. The case study in chapter 4 shows that the most significant dynamic effects are found for faults rupturing within about 1 km of the free surface, including earlier arrival times caused by super-shear rupture velocities and an increase of peak horizontal motions by about a factor of three. The effects are most prominent in a band around the tip of the fault. The width of this band varies from about 3 km to about 13 km for fault dips from $30^o$ to $60^o$, respectively. For the peak velocities, this pattern includes a 1–3 km wide nodal zone along the fault tip as well as larger values above the deeper part of the fault. When surface rupture occurs, the normal-stress effects generate an increase of seismic moment of up to 71%, largest for the most steeply-dipping fault investigated ($60^o$). These results are obtained using

dynamic rupture in a simple slip-weakening friction model. When sliprate-weakening friction is included the peak motions are consistent, while increase of seismic moment is reduced by about 13%. The results also imply that time-dependent normal-stress effects cause larger ground motions for earthquakes on faults with surface rupture compared to those from buried events. The time-dependent normal-stress effects are enhanced in the presence of shallow low-velocity layers, which generate peak motions up to 9 times larger than that from the prescribed rupture on a $45^o$-degree dipping fault. The effect is largest for a model consisting of a single layer over a halfspace, where the reverberations are amplified by resonance. Moreover, the near-surface low-velocity layers tend to increase the rupture time as well as promote earlier transitions to super-shear velocities. The results suggest that time-dependent dynamic interaction significantly affects the ground motion for dipping thrust faults. Therefore I strongly recommend that the effects be incorporated into future kinematic rupture simulations or attenuation relations.

# Appendix A

# Free-Surface Boundary-Condition

In this appendix the accuracy of two implementations of the explicit free-surface boundary-condition for the 3D fourth-order velocity-stress staggered-grid Finite Difference scheme is computed. This is done by a comparison of time-histories computed with two different implementations to a reflectivity solution [23]. The accuracy of the implementations is estimated using the misfit between the seismograms from the Finite Difference solutions and those computed by the reflectivity method for a uniform halfspace model.

The two different possibilities for the implementation of the explicit free-surface boundary-condition in the staggered grid lie half a grid point apart vertically (see also figure 1.1). The implementation co-located with the normal stress positions ($\sigma_{xx}$, $\sigma_{yy}$,$\sigma_{zz}$) [51], is hereafter denoted FS1. The other possibility is to implement the free surface co-located with the $xz$ and $yz$ stresses, offset half a grid vertically from the FS1 implementation and will hereafter be denoted FS2.

The total misfit for all three components of the wavefield is generally found to be larger for the free surface co-located with the normal stresses, compared to that for the free surface co-located with the $xz$ and $yz$ stresses. However, this trend is reversed when compared to the reflectivity solution exactly at the free surface (the misfit encountered in staggered-grid modeling). When the wavefield is averaged across the free surface, thereby centering the staggered wavefield exactly on the free surface, the free-surface condition co-located with the $xz$ and $yz$ stresses generates the smallest total misfit for increasing epicentral distance. For an epicentral distance/hypocentral depth of 10 the total misfit of this condition is about 15% smaller than that for the condition co-located with the normal stresses, mainly controlled by the misfit on the Rayleigh wave.

## A.1 Explicit Free-Surface Boundary-Condition

At a free surface with normal vector (0,0,1), the following equation must be satisfied:

$$\sigma_{zz} = \sigma_{xz} = \sigma_{yz} = 0. \tag{A.1}$$

For implementation FS1, the horizontal velocities $v_x$ and $v_y$ are located exactly at the free surface, while the vertical velocity $v_z$ is located half a grid point below. For implementation FS2, the horizontal velocities $v_x$ and $v_y$ are positioned half a grid point below the free surface, while the vertical velocity $v_z$ is located exactly at the surface. The coordinate system is right-handed, with the z axis positive downward.

### A.1.1 Free-Surface Boundary-Condition FS1

Implementation FS1 is summarized in the following. Let the free surface be located at vertical index $k$. $\sigma_{zz}$ is located at the surface and is explicitly set to zero:

$$\sigma_{zz}^{k} = 0. \tag{A.2}$$

$\sigma_{zz}$, $\sigma_{xz}$ and $\sigma_{yz}$ above the free surface are obtained using anti-symmetry:

$$\sigma_{zz}^{k-1} = -\sigma_{zz}^{k+1}, \tag{A.3}$$

$$\sigma_{xz}^{k-\frac{1}{2}} = -\sigma_{xz}^{k+\frac{1}{2}} \quad \text{and} \quad \sigma_{xz}^{k-\frac{3}{2}} = -\sigma_{xz}^{k+\frac{3}{2}}, \tag{A.4}$$

$$\sigma_{yz}^{k-\frac{1}{2}} = -\sigma_{yz}^{k+\frac{1}{2}} \quad \text{and} \quad \sigma_{yz}^{k-\frac{3}{2}} = -\sigma_{yz}^{k+\frac{3}{2}}. \tag{A.5}$$

$\sigma_{xx}$, $\sigma_{yy}$ and $\sigma_{xy}$ are not used above the free surface. Using equations A.2 to A.5 the following difference equations for the velocity at and above the free surface can be derived:

$$D_z v_z^k = \frac{-\lambda}{\lambda + 2\mu}[D_x v_x^k + D_y v_y^k], \tag{A.6}$$

$$[D_z v_x + D_x v_z]^{k-\frac{1}{2}} = -[D_z v_x + D_x v_z]^{k+\frac{1}{2}}, \tag{A.7}$$

$$[D_z v_y + D_y v_z]^{k-\frac{1}{2}} = -[D_z v_y + D_y v_z]^{k+\frac{1}{2}}, \tag{A.8}$$

where $D_l^n$ represents a centered, 2nd-order Finite Difference approximation to the differential operator $\frac{\partial}{\partial l}$ in direction $l$ at vertical level $n$.
For implementation FS1 special attention must be given to the computation of the horizontal normal stresses ($\sigma_{xx}$ and $\sigma_{yy}$) at the surface, since they involve the vertical velocity at three half grid points above the surface. This value is usually not solved by the above second-order difference equations [51]. The most obvious choice is to use second-order accuracy in the computation of the vertical derivatives of the horizontal normal stresses at the free surface for FS1 which is the implementation that will be discussed in the following. I also tested the accuracy of using fourth-order accuracy and simply setting $v_z = 0$ at three half grid points above the surface. However, the accuracy of the latter implementation was worse than the former everywhere.

### A.1.2 Free-Surface Boundary-Condition FS2

Implementation FS2 is defined by locating the surface at $k-\frac{1}{2}$, i.e., half a grid point vertically apart from implementation FS1:

$$\sigma_{xz}^{k-\frac{1}{2}} = \sigma_{yz}^{k-\frac{1}{2}} = 0. \tag{A.9}$$

$\sigma_{zz}$, $\sigma_{xz}$ and $\sigma_{yz}$ above the free surface are obtained using anti-symmetry:

$$\sigma_{zz}^{k-1} = -\sigma_{zz}^{k}, \tag{A.10}$$

$$\sigma_{xz}^{k-\frac{3}{2}} = -\sigma_{xz}^{k+\frac{1}{2}}, \tag{A.11}$$

$$\sigma_{yz}^{k-\frac{3}{2}} = -\sigma_{yz}^{k+\frac{1}{2}}. \tag{A.12}$$

Again, $\sigma_{xx}$, $\sigma_{yy}$ and $\sigma_{xy}$ are not used above the free surface. Using equations A.9 to A.12 the following difference equations for the velocity at and above the free surface can be derived:

$$(\lambda+2\mu)[D_z v_z]^{k-1}+\lambda[D_y v_y+D_x v_x]^{k-1} = -(\lambda+2\mu)[D_z v_z]^{k}+\lambda[D_y v_y+D_x v_x]^{k}, \tag{A.13}$$

$$D_z v_x^{k-\frac{1}{2}} = -D_x v_z^{k-\frac{1}{2}}, \tag{A.14}$$

$$D_z v_y^{k-\frac{1}{2}} = -D_y v_z^{k-\frac{1}{2}}. \tag{A.15}$$

## A.2 Source and Receiver Configuration and Model Description

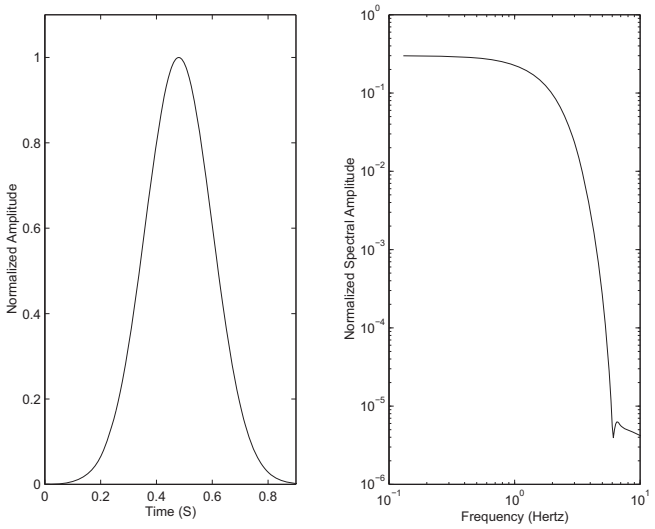


Figure A.1: *Source time function for the accuracy test.*

A double-couple point source with a rise time of 0.1 seconds is inserted at (0 m, 0 m, 2000 m) in a uniform halfspace model, with a compressional wave velocity of 6.0 km/s, a shear wave velocity of 3.464 km/s, and a density of 2.7 g/m$^3$. The only non-zero moment tensor component is $M_{xy}$ (equal to $M_{yx}$), which has the value $M_0 = 10^{18}$ Nm. The moment $M(t)$ and moment rate $\dot{M}(t)$ time histories are

$$M(t) = M_0 \cdot (1 - (1 + \frac{t}{\tau_r}) \cdot e^{-\frac{t}{\tau_r}}) \tag{A.16}$$

and

$$\dot{M}(t) = M_0 \cdot (\frac{t}{\tau_r^2}) \cdot e^{-\frac{t}{\tau_r}}, \tag{A.17}$$

respectively, where t is time and $\tau_r$ is the rise time. For FS1, the source is naturally located at 2 km depth, while for FS2 the source is approximated by the average between (0,0,2050 m) and (0,0,1950 m). The synthetic velocity time histories are computed at the surface point (i·600 m, i·800 m, 0 m), i=1,..,20, i.e., the receivers are located along a line oriented at angle 53.13$^o$ (i.e., $tan^{-1}(\frac{4}{3})$) to the x axis. The source-time function (figure A.1) is then deconvolved from the ground motion time histories and convolved with a Gaussian-shaped function corresponding to approximately six

points per shear wavelength with $v_s = 3.464$ km/s and $dx = 100$ m. No attenuation is included in the simulations. The modeling parameters are summarized in table A.1.

| | |
|---|---|
| Spatial discretization (m) | 100 |
| Temporal discretization (s) | 0.0075 |
| Number of E-W grid points | 750 |
| Number of N-S grid points | 750 |
| Number of vertical grid points | 297 |
| Number of timesteps | 1112 |
| Simulation time (s) | 8.34 |

Table A.1: *Geometrical modeling parameters for the accuracy test.*

## A.3 Numerical Results

### A.3.1 Comparison Between FS1 and FS2

Two sets of comparisons are of relevance in order to measure the accuracy of the FD free-surface boundary-conditions. The first is to address the "true misfit" of the conditions, where the FD solutions are compared to reflectivity solutions computed at the positions of the staggered wavefield components. These positions are half a grid point below the actual free surface for some components because of the staggered grid. The other is to measure the "actual misfit", where the FD solutions are always compared to the reflectivity solutions at the free-surface position. The "actual misfit" is what is generally encountered in reality and includes the "true misfit" and the misfit introduced by the fact that some parameters are located half a grid point below the surface.

Figure A.2 shows the misfit for the two FD free-surface boundary-conditions compared to the reflectivity solution. The misfit is measured as

$$\frac{\sqrt{\sum_t \left(S(t)_{REFL} - S(t)_{FD}\right)^2}}{\sqrt{\sum_t S(t)_{REFL}{}^2}} \tag{A.18}$$

for the radial, transverse, and vertical components, and for the three components combined. The "true misfit" is shown in the left column of figure A.2. The misfit

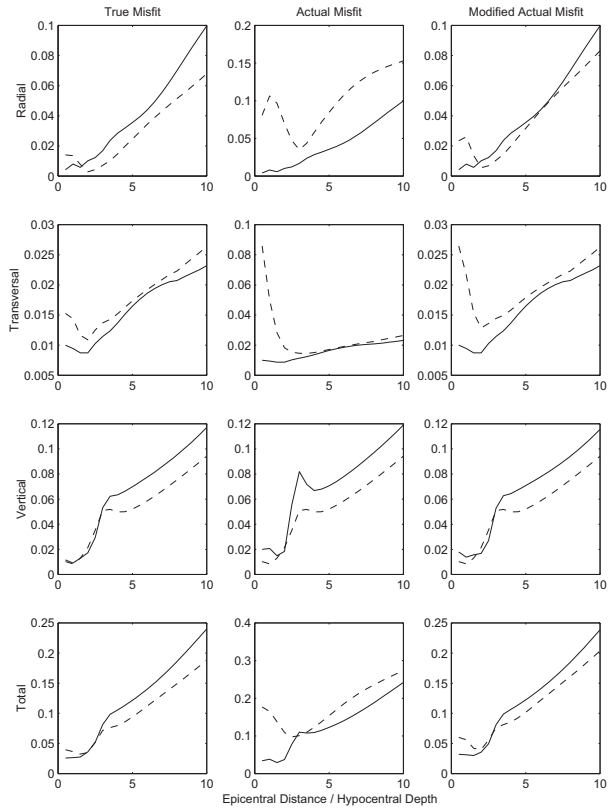


Figure A.2: *Accuracy of the two implementations of the free-surface boundary-condition. Misfit for (left column) reflectivity solution at staggered positions ("True Misfit", see section A.3.1), (middle column) reflectivity solution at the free surface ("Actual Misfit", see section A.3.1), and (right column) reflectivity solution at the free surface and averaged FD results ("Modified Actual Misfit", see section A.3.2). Solid and dashed lines depict the misfit for FS1 and FS2, respectively (see text).*

is similar and small for the transverse component (below 0.03 at an epicentral distance divided by the hypocentral depth (EDHD) of 10), while the appearance of the Rayleigh wave causes that for the radial (32%) and vertical (20%) components as well as the total misfit (22%) here to be about smaller for FS2 compared to that for FS1.

The "actual misfit" is shown in the middle column of figure A.2. At 10 EDHD FS1 (misfit below 0.15) is superior to FS2 (misfit below 0.1) for the horizontal components (located at the surface for FS1, half a grid point below for FS2), while FS2 (misfit 0.093) is more accurate than FS1 (misfit 0.12) for the vertical component (positioned at the surface for FS2, half a grid point below for FS1). The misfit for FS2 is much larger than that for FS1 close to the epicenter. FS1 is generally more

accurate than FS2 when all components are considered. The computation of the "modified actual misfit" will be described in section A.3.2.

Figure A.3 shows comparisons of the reflectivity solution to the FD solutions and the misfit for the two implementations of the free-surface boundary-condition. The residuals are enhanced by a factor of 5 for site 1 for clarity, while the actual residuals are displayed for site 20. The largest (actual) misfit at site 1 (below 0.1, see figure A.2) appears on the horizontal components for FS2. Figure A.3 reveals that this misfit is mainly due to a slightly early arrival of the P and S waves. This timing misfit is in part due to the necessity of averaging the source across grid lines between 1950 m and 2050 m, which transfers energy toward earlier (and later) times. However, the fact that the horizontal components here are positioned half a grid point below the surface is by far the largest reason for the slightly early arrival for the FS2 horizontal motions at site 1. The vertical component for FS2 is positioned at the free surface and shows much smaller misfit. At site 20, by far the largest part of the total misfit is due to the Rayleigh wave (about 0.27 "actual misfit" for FS2). The largest misfit is indeed expected to be related to the surface waves, which are generated at and propagating close to the free surface. While FS2 is overall more accurate than FS1 (0.18 versus 0.24 "true misfit") the staggered positions increase the "actual misfit" for FS2 at site 20.

As mentioned above, FS1 requires the use of second-order accuracy in the computation of the vertical derivatives of the horizontal normal stresses at the free surface. Here, no significant improvement in the error is found, whether 2nd-order or 4th-order accuracy is used for the horizontal derivatives of these parameters.

### A.3.2 Refinement of FS1 and FS2

Finally, I attempt to improve the accuracy of the two boundary-conditions compared to the "actual misfit". The obvious suggestion is to average the components which are positioned half a grid point below the free surface with those located half a grid point above the free surface. However, the validity of this procedure is not clear, as it involves non-physical parameters positioned virtually above the surface. On the other hand, the conditions for FS1 and FS2 imply symmetry of the particle velocities across the free surface. The misfit of the averaged parameters is shown in the right column of figure A.2 ("modified actual misfit").

The misfit obtained is up to three times smaller for the averaged seismograms compared to that at locations half a grid point below the surface. When averaged, the

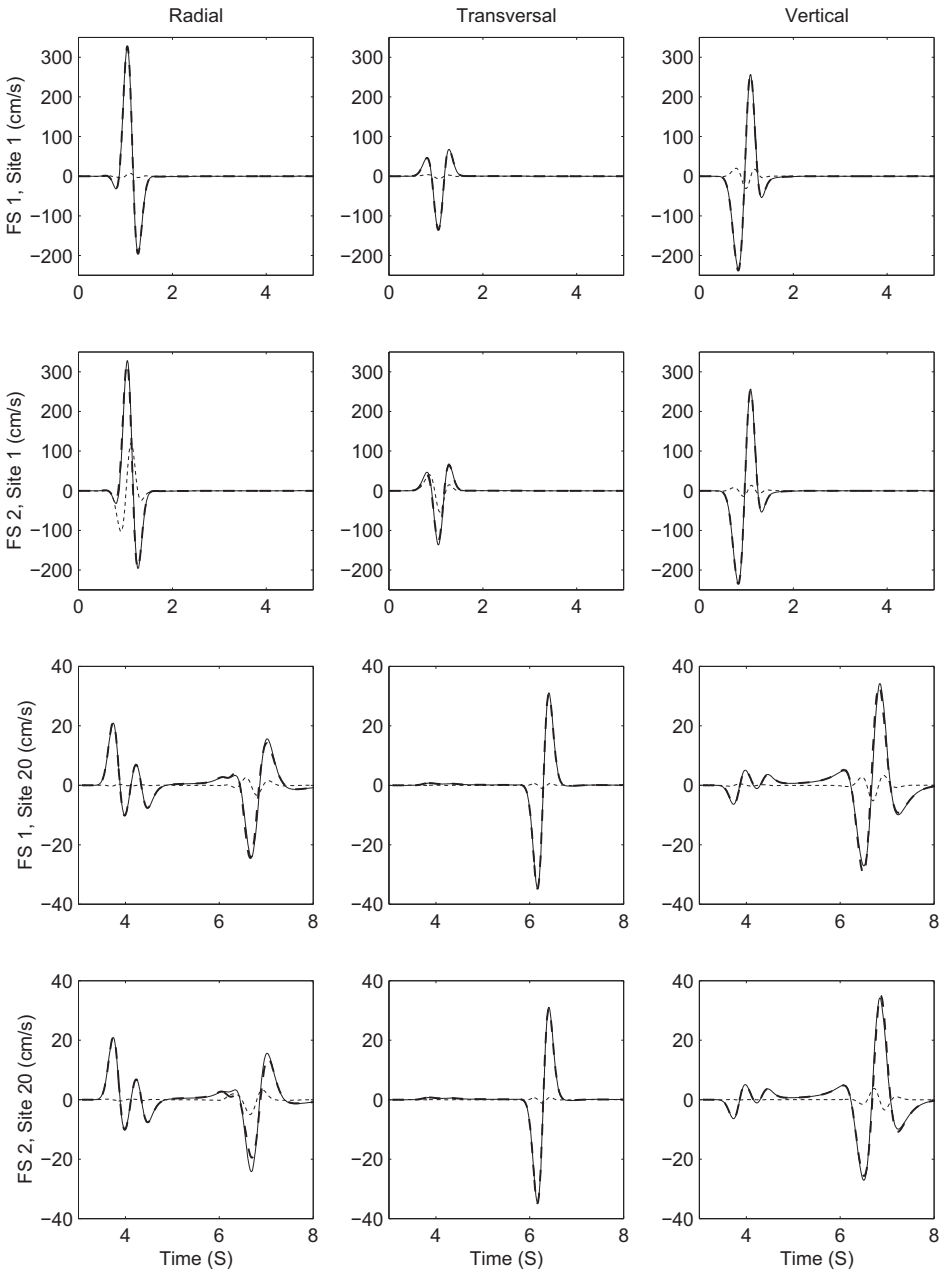


Figure A.3: *Comparison of surface velocity time-histories for the two implementations of the FD free-surface condition discussed in this appendix (FS1 and FS2, long-dashed traces) to the reflectivity solution (solid traces, "actual misfit"). The short-dashed line shows the difference between the reflectivity and FD solutions. The difference is multiplied by 5 for site 1, while the actual difference is shown for site 20.*

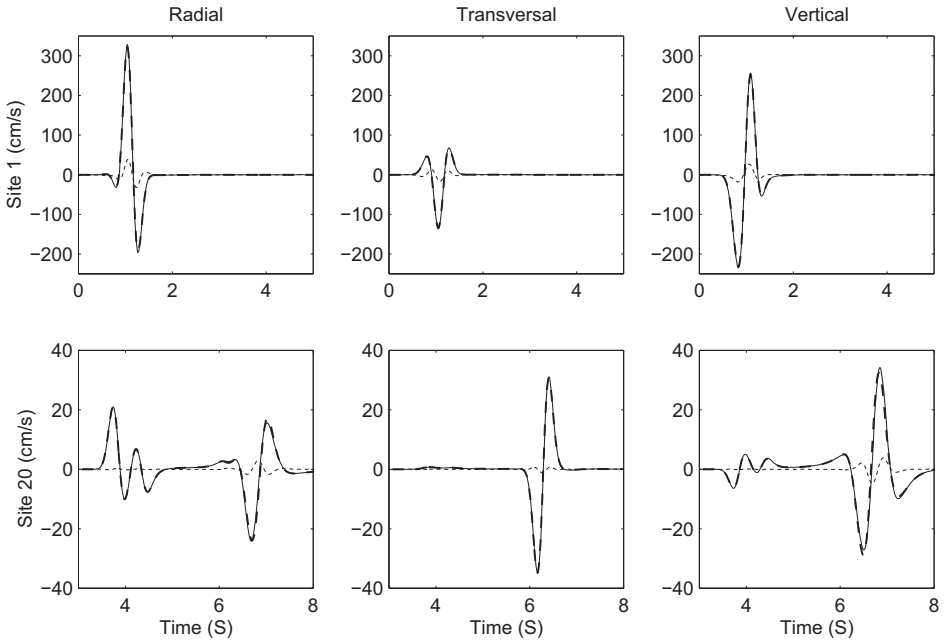


Figure A.4: *Same as figure A.3, but averaged seismograms are shown when applicable.*

total misfit is similar (below 0.07) for FS1 and FS2 less than 3 EDHD, while the total misfit at 10 EDHD is about 15% smaller for FS2 than that for FS1. This is mainly due to a more accurately modeled Rayleigh wave for FS2 than for FS1 (see below).

Figure A.4 shows comparisons of the reflectivity solution to the FD averaged (where applicable) solutions and the differences between the two different free-surface boundary-conditions at sites 1 (0.5 EDHD) and 20 (10 EDHD). The averaged seismograms clearly show an improved fit compared to the reflectivity solution.

# Bibliography


[1] Aagaard, B.T., J.F. Hall, and T.H. Heaton, Characterization of Near-Source Ground Motions with Earthquake Simulations, *Earthquake Spectra, 17*, 177 – 207, 2001.

[2] Aagaard, B.T., T.H. Heaton, and J.F. Hall, Dynamic Earthquake Ruptures in the Presence of Lithostatic Normal Stresses: Implications for Friction Models and Heat Production, *Bull. Seis. Soc. Am., 91*, 1765 – 1796, 2001.

[3] Abrahamson, N.A. and W.J. Silva, Empirical Response Spectral Attenuation Relations for Shallow Crustal Earthquakes, *Seismol. Res. Lett., 68*, 94 – 128, 1997.

[4] Aki, K. and P.G, Richards, *Quantitative Seismology,* W.H. Freeman and Company, New York, 1980.

[5] Al-Zoubi, A., H. Shulman, and Z. Ben-Avraham, Seismic Reflection Profiles Across the Southern Dead Sea Basin, *Tectonophysics, 346,* 61 – 69, 2002.

[6] Ambraseys, N.N., Uniform Magnitude Re-Evaluation of European Strong-Motion Records, *Earthq. Eng. Struc. Dyn., 19,* 1 – 20, 1990.

[7] Ambraseys, N.N., C.P. Melville, and R.D. Adams, *The Seismicity of Egypt, Arabia, and the Dead Sea: A Historical Review*, Cambridge University Press, Cambridge, 1994.

[8] Ambraseys, N.N., Reassessment of Earthquakes, 1900 – 1999, in the Eastern Mediterranean and Middle East, *Geophys. J. Int., 145,* 471 – 485, 2001.

[9] Amiran, D.H.K., E. Arieh, and T. Turcotte, Earthquakes in Israel and Adjacent Areas: Macroseismic Observations Since 100 B.C.E., *Isr. Exploration J., 44,* 260 – 305, 1994.

[10] Andrews, J., Rupture Propagation with Finite Stress in Antiplane Strain, *J. Geophys. Res., 81*, 3575 – 3582, 1976.

[11] Andrews, J., Rupture Velocity of Plane Strain Shear Cracks, *J. Geophys. Res., 81*, 5679 – 5687, 1976.

[12] Anonymous, *Seismisches Bulletin,* Landesamt für Geologie, Rohstoffe und Bergbau, Baden-Württemberg, 1996.

[13] Anonymous, *Seismisches Bulletin,* Landesamt für Geologie, Rohstoffe und Bergbau, Baden-Württemberg, 1997.

[14] Aochi, H., R. Madariaga, and E. Fukuyama, Effect of Normal Stress During Rupture Propagation Along Non-Planar Faults, *J. Geophys. Res., 107*, ESE5-1 – ESE5-10, 2002.

[15] Aoudia, A., F. Vaccari, P. Suhadolc, and M. Megrhaoui, Seismogenic Potential and Earthquake Hazard Assessment in the Tell Atlas of Algeria, *J. Seismol., 4,* 79 – 98, 2000.

[16] Ben-Menahem, A., Earthquake Catalogue for the Middle East (92 BC - 1980 AD), *Boll. Geofis. Teor. Appl., 21*, 245 – 310, 1979.

[17] Ben-Menahem, A., Four Thousand Years of Seismicity Along the Dead Sea Rift, *J. Geophys. Res., 96,* 20195 – 20216, 1991.

[18] Beroza, G.C., Near-Source Modeling of the Loma Prieta Earthquake: Evidence for Heterogeneous Slip and Implications for Earthquake Hazard, *Bull. Seis. Soc. Am., 81*, 1603 – 1621, 1991.

[19] Bodin, P. and J.N. Brune, On the Scaling of Slip with Rupture Length for Shallow Strike-Slip Earthquakes: Quasi-Static Models and Rupture Propagation, *Bull. Seis. Soc. Am., 86*, 1292 – 1299, 1996.

[20] Bolt, B.A., Modern Recording of Seismic Strong Motion for Hazard Reduction, in: F. Wenzel, D. Lungu, O. Novak (Editors): *Vrancea Earthquakes: Tectonics, Hazard and Risk Mitigation,* 1 – 13, Kluwer Academic Publishers, Dordrecht, 1999.

[21] Boore, D.M., and W.B. Joyner, Peak Horizontal Acceleration and Velocity from Strong-Ground Motion Recordings Including Records from the 1979 Imperial Valley, Caifornia, Earthquake, *Bull. Seis. Soc. Am., 71,* 2011 – 2038, 1981.

[22] Boore, D.M., W.B. Joyner, and T.E. Fumal, Equations for Estimating Horizontal Response Spectra and Peak Acceleration from Western North American Earthquakes: A Summary of Recent Work, *Seismol. Res. Lett., 68,* 128 – 153, 1997.

[23] Bouchon, M., A Simple Method to Calculate Green's Functions for Layered Media, *Bull. Seis. Soc. Am., 71*, 959 – 971, 1981.

[24] Brune, J.N., Shattered Rock and Precarious Rock Evidence for Strong Asymmetry in Ground Motions During Thrust Faulting, *Bull. Seis. Soc. Am., 91*, 441 – 447, 2001.

[25] Camelbeeck, T. and M. Meghraoui, Large Earthquakes in Northern Europe More Likely Than Once Thought, *Eos Trans. AGU, 77*, 405 – 409, 1996.

[26] Cerjan, C., D. Kosloff, R. Kosloff, and M. Reshew, A Nonreflecting Boundary Condition for Discrete Acoustic and Elastic Wave-Equations, *Geophysics, 50*, 705 – 708, 1985.

[27] Clayton, R. and B. Engquist, Absorbing Boundary Conditions for Acoustic and Elastic Wave Equations, *Bull. Seis. Soc. Am., 67*, 1529 – 1540, 1977.

[28] Dalguer, L.A., K. Irikura, R.D. Riera, and H.C. Chiu, The Importance of the Dynamic Source Effects During the 1999 Chi-Chi, Taiwan, Earthquake: Brief Interpretation of the Damage Distribution on Buildings, *Bull. Seis. Soc. Am., 91*, 1112 – 1127, 2001.

[29] Day, S.M., Three-Dimensional Simulation of Spontaneous Rupture: The Effect of Non-Uniform Prestress, *Bull. Seis. Soc. Am., 72*, 1881 – 1902, 1982.

[30] Day, S.M., G. Yu, and D. Wald, Dynamic Stress Changes During Earthquake Rupture, *Bull. Seis. Soc. Am., 88*, 512 – 522, 1998.

[31] Dieterich, J., Time-Dependent Friction and the Mechanics of Stick-Slip, *Pure Appl. Geophys., 116*, 790 – 806, 1978.

[32] Dieterich, J., Modeling of Rock Friction: 1. Experimental Results and Constitutive Equations, *J. Geophys. Res., 84*, 2161 – 2168, 1979.

[33] Durran, D.R., *Numerical Methods for Wave Equations in Geophysical Fluid Dynamics,* Springer, Berlin, 1999.

[34] Erdik, M., Y.A. Biro, T. Onur, K. Sesetyan, and G. Birgoren, Assessment of Earthquake Hazard in Turkey and Neighboring Regions, *Annali di Geofisica, 42*, 1125 – 1138, 1999.

[35] Field, E.H., J.G. Anderson, T.L. Henyey, D.D. Jackson, W.B. Joyner, Y. Lee, H. Magistrale, B. Minster, K.B. Olsen, M.D. Petersen, J.H. Steidl, L.A. Wald, and C.J. Wills, Accounting for Site Effects in Probablilistic Seismic Hazard Analyses of Southern California: Overview of the SCEC Phase III Report, *Bull. Seis. Soc. Am., 90*, S1 – S31, 2000.

[36] Fukuyama, E. and K.B. Olsen, A Condition for Super-Shear Rupture Propagation in a Heterogeneous Stress Field, *Pure Appl. Geophys.*, in press.

[37] Garfunkel, Z. and Z. Ben-Avraham, The Structure of the Dead Sea Basin, *Tectonophysics, 266,* 155 – 176, 1996.

[38] Geller, R.J., Scaling Relations for Earthquake Source Parameters and Magnitudes, *Bull. Seis. Soc. Am., 66,* 1501 – 1523, 1976.

[39] Giardini, D., The Global Seismic Hazard Assessment Program (GSHAP), 1992-1999, *Annali di Geofisica, 42*, 957 – 976, 1999.

[40] Giardini, D., G. Grünthal, K.M. Shedlock, and P. Zhang, The GSHAP Global Seismic Hazard Map, *Annali di Geofisica, 42*, 1225 – 1228, 1999.

[41] Ginzburg, A. and Z. Ben-Avraham, A Seismic Refraction Study of the North Basin of the Dead Sea, *Geophys. Res. Lett., 24,* 2063 – 2066, 1997.

[42] Gottschämmer, E. and K.B. Olsen, Accuracy of the Explicit Planar Free-Surface Boundary Condition Implemented in a Fourth-Order Staggered-Grid Velocity-Stress Finite-Difference Scheme, *Bull. Seis. Soc. Am., 91*, 617 – 623, 2001.

[43] Gottschämmer, E. and K.B. Olsen, Ground Motion Synthetics for Spontaneous Versus Prescribed Rupture on a 45 Degree Thrust Fault, *Geophys. Res. Abs., 4*, 530, 2002.

[44] Gottschämmer, E. and K.B. Olsen, Time-Dependent Normal-Stress Alteration of Ground Motions for Dipping Thrust Faults, subm. to *Bull. Seis. Soc. Am.,* 2002.

[45] Gottschämmer, E. and F. Wenzel, Nahfeldeffekte großer Erdbeben, *Proceedings of the Annual Meeting of the German Geophysical Society (DGG)*, Munich, 144, 2000.

[46] Gottschämmer, E., K.B. Olsen, and F. Wenzel, Three-Dimensional Simulation of Earthquakes in the Upper Rhinegraben: Effects of Topography and Material Attenuation, *Geophys. Res. Abs., 1*, 249, 1999.

[47] Gottschämmer, E., K.B. Olsen, and F. Wenzel, 3D Finite-Difference Simulation of Wave Propagation in the Rhinegraben: Effects of Crustal Structure, Event Magnitude, and Hypocentral Depth, *Eos Trans. AGU, 80*, F711, 1999.

[48] Gottschämmer, E., K.B. Olsen, and F. Wenzel, Finite-Difference Modeling of Earthquakes in the Upper Rhinegraben, Germany, *Eos Trans. AGU, 81*, F827, 2000.

[49] Gottschämmer, E., F. Wenzel, G.H. Wust-Bloch, and Z. Ben-Avraham, Earthquake Modeling in the Dead Sea Basin, *Geophys. Res. Lett.*, in press.

[50] Gottschämmer, E., F. Wenzel, G.H. Wust-Bloch, and Z. Ben-Avraham, Finite-Difference Simulations of the 1927 Jericho Earthquake, in: F. Wenzel (Editor), *Challenges for Earth Sciences in the 21st Century,* Springer, Berlin, in press.

[51] Graves, R.W., Simulating Seismic Wave Propagation in 3D Elastic Media Using Staggered Grid Finite Differences, *Bull. Seis. Soc. Am., 86*, 1091 – 1106, 1996.

[52] Graves, R.W., 3D Finite Difference Modeling of the San Andreas Fault: Source Parameterization and Ground Motion Levels, *Bull. Seis. Soc. Am., 88*, 881 – 897, 1998.

[53] Grünthal, G., Seismic Hazard Assessment for Central North and Northwest Europe: GSHAP Region 3, *Annali di Geofisica, 42*, 999 – 1012, 1999.

[54] Guatteri, M., P.M. Mai, G.C. Beroza, and J. Boatwright, Strong Ground Motion Prediction from Stochastic-Dynamic Source Models, *Bull. Seis. Soc. Am.,* in press.

[55] Gutscher, M.A., Structure and Dynamics in the Rhinegraben and the Alpine Foreland, *Geophys. J. Int., 122*, 617 – 636, 1995.

[56] Harris, R. and S.M. Day, Effects of a Low-Velocity Zone on a Dynamic Rupture, *Bull. Seis. Soc. Am., 87*, 1267 – 1280, 1997.

[57] Hanks, T.C. and H. Kanamori, A Moment Magnitude Scale, *J. Geophys. Res, 84*, 2348 – 2350, 1979.

[58] Heaton, T., Evidence for and Implications of Self-Healing Pulses of Slip in Earthquake Rupture, *Phys. Earth Planet. Inter., 64,* 1 – 20, 1990.

[59] Heaton, T., J.F. Hall, D. Wald, and M.W. Halling, Response of High-Rise and Base-Isolated Buildings to a Hypothetical $M_W = 7$ Blind Thrust Earthquake, *Science, 267,* 206 – 211, 1995.

[60] Hestholm, S.O. and B.O. Ruud, 3-D Finite-Difference Elastic Wave Modeling Including Surface Topography, *Geophysics, 63*, 613 – 622, 1998.

[61] Holbrook, W. S., D. Gajewski, A. Krammer, and C. Prodehl, An Interpretation of Wide-Angle Shear-Wave Data in Southwest Germany: Poisson's Ratio and Petrological Implications, *J. Geophys. Res., 93*, 12081 – 12106, 1988.

[62] Ida, Y., Cohesive Force Across the Tip of a Longitudinal Shear Crack and Griffith's Specific Surface Energy, *J. Geophys. Res., 77*, 3796 – 3805, 1972.

[63] Igel, H. and Ita, J., The Effects of Subduction Zones on Teleseismic SH Waves: A Numerical Study, in: K. Fuchs (Editor), *Upper Mantle Heterogeneities from Active and Passive Seismology,* 333 – 341, Kluwer Academic Publishers, 1997.

[64] Igel, H. and M. Weber, SH Wave Propagation in the Whole Mantle Using High-Order Finite Differences, *Geophys. Res. Lett., 22*, 731 – 734, 1995.

[65] Igel, H. and M. Weber, P-SV Wave Propagation in the Earth's Mantle Using Finite Differences: Application to Heterogeneous Lowermost Mantle Structure, *Geophys. Res. Lett., 23*, 415 – 418, 1996.

[66] Igel, H., T. Nissen-Meyer, and G. Jahnke, Wave Propagation in 3D Spherical Sections: Effects of Subduction Zones, *Phys. Earth Planet. Inter.*, in press.

[67] Inoue, T. and T. Miyatake, 3D Simulation of Near-Field Strong Ground Motion, *Bull. Seis. Soc. Am., 88,* 1445 – 1456, 1998.

[68] Joyner, W.B. and D.M. Boore, Peak Horizontal Acceleration and Velocity from Strong Motion Records, *Bull. Seis. Soc. Am., 71,* 2011 – 2038, 1981.

[69] Kanamori, H., The Energy Release in Great Earthquakes, *J. Geophys. Res., 82,* 2981 – 2987, 1977.

[70] Kanamori, H. and D.L. Anderson, Theoretical Basis of Some Empirical Relations in Seismology, *Bull. Seis. Soc. Am., 65,* 1073 – 1095, 1975.

[71] Karrenbach, M., *Elastic Tensor Wave Fields,* Ph.D. thesis, Stanford University, 1995.

[72] Karrenbach, M., *Modeling Physical Systems: Wave Propagation by FD Examples,* Lecture book, University Fridericiana, Karlsruhe, 1996.

[73] Karrenbach, M., J. Ritter, and K. Fuchs, Wave Propagation in the Heterogeneous Lower Crust, *Stanford Exploration Project, 80,* 1 – 572, 2001.

[74] Kelly, K.R., R.W. Ward, S. Treitel, and R.M. Alford, Synthetic Seismograms: A Finite-Difference Approach, *Geophysics, 41,* 2 – 27, 1976.

[75] Lay, T. and T.C. Wallace, *Modern Global Seismology,* Academic Press, San Diego, 1995.

[76] Levander, A., Fourth-Order Finite-Difference P-SV Seismograms, *Geophysics, 53*, 1425 – 1436, 1988.

[77] Leydecker, G., *Erdbebenkatalog für die Bundesrepublik Deutschland mit Randgebieten für die Jahre 1000 – 1981,* Geol. Jahrbuch, E 36, 3 – 81, Hannover, 1986.

[78] Madariaga, R., Dynamics of an Expanding Circular Fault, *Bull. Seis. Soc. Am., 66*, 639 – 666, 1976.

[79] Madariaga, R., K.B. Olsen, and J.R. Archuleta, Modeling Dynamic Rupture in a 3D Earthquake Fault Model, *Bull. Seis. Soc. Am., 88*, 1182 – 1197, 1998.

[80] Madariaga, R., K.B. Olsen, and J.R. Archuleta, 3D Finite Difference Simulation of a Dynamic Rupture, *Eos Trans. AGU, 77*, F470, 1996.

[81] Madariaga, R., Radiation from a Finite Reverse Fault in a Halfspace, in preparation.

[82] Madariaga, R. and K.B. Olsen, Criticality of Rupture Dynamics in 3-D, *Pure Appl. Geophys., 157*, 1981 – 2001, 2000.

[83] Madariaga, R. and K.B. Olsen, Earthquake Dynamics, in: W.H.K. Lee, H. Kanamori, P.C. Hennings, and C. Kisslinger (Editors), *International Handbook of Earthquake and Engineering Seismology,* 2002.

[84] Mai, P.M., *Characterizing Earthquake Source Complexity for Improved Strong Motion Prediction,* Ph.D. thesis, 149 pp., Stanford University, Stanford, 2002.

[85] Malvern, L.E., *Introduction to the Mechanics of a Continuous Medium,* Prentice-Hall, Englewood Cliffs, 1969.

[86] Mayer-Rosa, D. and Cadiot, B., A Review of the 1356 Basel Earthquake, *Tectonophysics, 53*, 325 – 333, 1979.

[87] Meghraoui, M., B. Delouis, M. Ferry, D. Giardini, P. Huggenberger, I. Spottke, and M. Granet, Active Normal Faulting in the Upper Rhine Graben and Paleoseismic Identification of the 1356 Basel Earthquake, *Science, 293*, 2070 – 2073, 2001.

[88] Miksat, J., *3D-Finite-Differenzen-Modellierung des Marmarabebens,* Diplom thesis, 93 pp., University Fridericiana, Karlsruhe, 2002.

[89] Miksat, J., E. Gottschämmer, and F. Wenzel, 3D Finite-Difference Modeling of the 1999 Marmara Earthquake, *Geophys. Res. Abs., 4*, 3493, 2002.

[90] Molin, D. and A. Paciello, Seismic Hazard Assessment in Florence City, Italy, *J. Earthq. Eng., 3*, 475 – 494, 1999.

[91] Musson, R.M.W., Probabilistic Seismic Hazard Maps for the North Balkan Region, *Annali di Geofisica, 42*, 1109 – 1124, 1999.

[92] Neuberg, J., R. Luckett, B. Baptie, and K.B. Olsen, Models of Tremor and Low-Frequency Earthquake Swarms on Montserrat, *J. Volc. Geoth. Res., 101*, 83 – 104, 2000.

[93] Nielsen, S.B. and K.B. Olsen, Constraints on Stress and Friction from Dynamic Rupture Models of the 1994 Northridge, California, Earthquake, *Pure Appl. Geophys., 157*, 2029 – 2046, 2000.

[94] Nielsen, S.B., J.M. Carlson, and K.B. Olsen, Influence of Friction and Fault Geometry on Earthquake Rupture, *J. Geophys. Res., 105*, 6069 – 6088, 2000.

[95] Nielsen, S.B., Free Surface Effects on the Propagation of Dynamic Rupture, *Geophys. Res. Lett., 25*, 125 – 128, 1998.

[96] Nur, A. and H. Ron, And the Walls Came Tumbling Down: Earthquake History in the Holyland, in: S. Stirros and R.E. Jones (Editors), *Archaeoseismology,* 75 – 85, Institute of Geology & Mineral Exploration, Athens, 1996.

[97] Oglesby, D.D., R.J. Archuleta, and S.B. Nielsen, Earthquakes on Dipping Faults: the Effects of Broken Symmetry, *Science, 280*, 1055 – 1059, 1998.

[98] Oglesby, D.D., R.J. Archuleta, and S.B. Nielsen, Dynamics of Dip-Slip Faulting: Explorations in two Dimensions, *J. Geophys. Res., 105*, 13643 – 13653, 2000.

[99] Oglesby, D.D., R.J. Archuleta, and S.B. Nielsen, The Three-Dimensional Dynamics of Dipping Faults, *Bull. Seis. Soc. Am., 90*, 616 – 628, 2000.

[100] Ohminato, T. and B.A. Chouet, A Free Surface Boundary Condition for Including 3D Topography in the Finite Difference Method, *Bull. Seis. Soc. Am., 87*, 494 – 515, 1997.

[101] Ohnaka, M. and L.F. Shen, Characteristic Features of Local Breakdown Near Crack-Tip in the Transition Zone from Nucleation to Dynamic Rupture During Stick-Slip Shear Failure, *Tectonophysics, 175*, 197 – 220, 1990.

[102] Ohnaka, M. and L.F. Shen, Scaling of Rupture Process from Nucleation to Dynamic Propagation: Implications of Geometric Irregularity of the Rupturing Surfaces, *J. Geophys. Res., 104*, 817 – 844, 1999.

[103] Olsen, K.B., *Simulation of Three-Dimensional Wave Propagation in the Salt Lake Basin,* Ph.D. thesis, 157 pp., University of Utah, Salt Lake City, 1994.

[104] Olsen, K.B., Site Amplification in the Los Angeles Basin from 3D Modeling of Ground Motion, *Bull. Seis. Soc. Am., 90,* S77 – S94, 2000.

[105] Olsen, K.B. and R.J. Archuleta, Three-Dimensional simulation of Earthquakes on the Los Angeles Fault System, *Bull. Seism. Soc. Am., 86*, 575 – 596, 1996.

[106] Olsen, K.B., R.J. Archuleta, and J.R. Matarese (1995). Three-Dimensional Simulation of a Magnitude 7.75 Earthquake on the San Andreas Fault, *Science, 270*, 1628 – 1632, 1995.

[107] Olsen, K.B., R. Madariaga, and R.J. Archuleta, Three-Dimensional Dynamic Simulation of the 1992 Landers Earthquake, *Science, 278*, 834 – 838, 1997.

[108] Olsen, K.B., R. Nigbor, and T. Konno, 3D Viscoelastic Wave Propagation in the Upper Borrego Valley, California, Constrained by Borehole and Surface Data, *Bull. Seis. Soc. Am., 90*, 134 – 150, 2000.

[109] Olsen, K.B. and G.T. Schuster, Causes of Low-Frequency Ground Motion Amplification in the Salt Lake Basin: The Case of the Vertical Incident P-Wave, *Geophys. J. Int., 122*, 1046 – 1061, 1995.

[110] Orozova, I.M. and P. Suhadolc, A Deterministic-Probabilistic Approach for Seismic Hazard Assessment, *Tectonophysics, 312*, 199 – 202, 1999.

[111] Peyrat, S., K.B. Olsen, and R. Madariaga, Dynamic Modeling of the 1992 Landers Earthquake, *J. Geophys. Res., 106*, 26467 – 26482, 2001.

[112] Prodehl, C., S. Müller, A. Glahn, M. Gutscher, and V. Haak, Lithospheric Cross Sections of the European Cenozoic Rift System, *Tectonophysics, 208*, 113 – 138, 1992.

[113] Robertsson, J.O.A., A Numerical Free-Surface Condition for Elastic/Viscoelastic Finite-Difference Modeling in the Presence of Topography, *Geophysics, 61*, 1921 – 1934, 1996.

[114] Romanowicz, B., Strike-Slip Earthquakes on Quasi-Vertical Transcurrent Faults: Inferences for General Scaling Relations, *Geophys. Res. Lett., 19*, 481 – 484, 1992.

[115] Romanowicz, B. and J.B. Rundle, On Scaling Relations for Large Earthquakes, *Bull. Seis. Soc. Am., 83*, 1294 – 1297, 1993.

[116] Ruina, A., Slip Instability and State Variable Friction Laws, *J. Geophys. Res., 88*, 10359 – 10370, 1983.

[117] Sadigh, K., C.Y. Chang, J.A. Egan, F. Makdisi, and R.R. Youngs, Attenuation Relationships for Shallow Crustal Earthquakes Based on California Strong Motion Data, *Seismol. Res. Lett., 68*, 180 – 189, 1997.

[118] Sato, T., R.W. Graves, and R.G. Somerville, Three-Dimensional Finite-Difference Simulations of Long-Period Strong Motions in the Tokyo Metropolitan

Area During the 1990 Odawara Earthquake ($M_J$ 5.1) and the Great 1923 Kanto Earthquake ($M_S$ 8.2) in Japan, *Bull. Seis. Soc. Am., 89,* 579 – 607, 1999.

[119] Schmidt-Aursch, M., *Zweidimensionale Modellierung von Wellenausbreitung bei Erdbeben mit Finiten Differenzen,* Diplom thesis, 122 pp., University Fridericiana, Karlsruhe, 1998.

[120] Scholz, C.H., Scaling Laws for Large Earthquakes: Consequences for Physical Models, *Bull. Seis. Soc. Am., 72,* 1 – 14, 1982.

[121] Scholz, C.H., A Reappraisal of Large Earthquake Scaling, *Bull. Seis. Soc. Am., 84,* 215 – 218, 1994.

[122] Scholz, C.H., C.A. Aviles, and S.G. Wesnousky, Scaling Differences Between Large Interplate and Intraplate Earthquakes, *Bull. Seis. Soc. Am., 76,* 65 – 70, 1986.

[123] Shapira, A., H. Ron, and A. Nur, A New Estimate for the Epicenter of the Jericho Earthquake of 11 July 1927, *Israel J. Earth Sci., 42,* 93 – 96, 1993.

[124] Shapira, N., K.B. Olsen, and S.K. Singh, Wave-Guide Effects in Subduction Zones: Evidence from Three Dimensional Modeling, *Geophys. Res. Lett., 27,* 433 – 436, 2000.

[125] Shedlock, K.M., Seismic Hazard Assessment Map of North and Central America and the Caribbean, *Annali di Geofisica, 42*, 977 – 998, 1999.

[126] Shedlock, K.M., D. Giardini, G. Grünthal, , and P. Zhang, The GSHAP Global Seismic Hazard Map, *Seismol. Res. Lett., 71*, 679 – 686, 2000.

[127] Sieberg, A., *Untersuchungen über Erdbeben und Bruchschollenbau im östlichen Mittelmeer,* Verlag von Gustav Fischer, Jena, 1932.

[128] Smith, G.D., *Numerical Solution of Partial Differential Equations: Finite Difference Methods,* Clarendon Press, Oxford, 1985.

[129] Somerville, P.G., Observations of Earthquake Source and Ground Motion Scaling at the Macro Level, *2nd ACES Workshop Proceedings*, Tokyo and Hakone, 167 – 174, 2000.

[130] Somerville, P.G., N.F. Smith, R.G. Graves, and N.A. Abrahamson, Modification of empirical Strong Ground Motion Attenuation Relations to Include the Amplitude and Duration Effects of Rupture Directivity, *Seismol. Res. Lett., 68,* 199 – 222, 1997.

[131] Stange, S., Landesamt für Geologie, Rohstoffe und Bergbau, Baden-Württemberg, Stationen et al., *written communication,* 2001.

[132] Tittgemeyer, M., *Streuung elastischer Wellen im oberen Erdmantel,* Logos-Verlag, Berlin, 1999.

[133] Vidale, J. and D.V. Helmberger, Path Effects in Strong Motion Seismology, in B.A. Bolt (Editor): *Seismic Strong Motion Synthetics,* Academic Press Inc, London, 1987.

[134] Virieux, J., SH-Wave-Propagation in Heterogeneous Media: Velocity-Stress Finite-Difference Method, *Geophysics, 49*, 1933 – 1957, 1984.

[135] Virieux, J., P-SV-Wave-Propagation in Heterogeneous Media: Velocity-Stress Finite-Difference Method, *Geophysics, 51*, 889 – 901, 1986.

[136] Wald, D. and R.W. Graves, The Seismic Response of the Los Angeles Basin, California, *Bull. Seis. Soc. Am., 88*, 337 – 356, 1998.

[137] Wang, J. and S. Ou, On Scaling of Earthquake Faults, *Bull. Seis. Soc. Am., 88*, 758 – 766, 1998.

[138] Wells, D.L. and K.J. Coppersmith, New Empirical Relations Among Magnitude, Rupture Length, Rupture Width, Rupture Area, and Surface Displacement, *Bull. Seis. Soc. Am., 84,* 974 – 1002, 1994.

[139] Wenzel, F., M.C. Onescu, M. Baur, F. Fiedrich, and C. Ionescu, 25 Seconds for Bucharest, in: F. Wenzel, D. Lungu, O. Novak (Editors): *Vrancea Earthquakes: Tectonics, Hazard and Risk Mitigation,* 349 – 356, Kluwer Academic Publishers, Dordrecht, 1999.

[140] Wust-Bloch, G.H., The Active Dead Sea Rift Fault Zone: A Seismic Wave-Guide, European Geophysical Society, Stephan Müller Special Publication Series, in press.

[141] Wust-Bloch, G.H. and D. Wachs, Seismic Triggering of Unstable Slopes in Northern Israel, *Israel J. Earth Sci., 49,* 103 – 109, 2000.

[142] Zeis, S., D. Gajewski, and C. Prodehl, Crustal Structure of Southern Germany from Seismic-Refraction Data, *Tectonophysics, 176,* 59 – 86, 1990.

[143] Zucca, J.J., The Crustal Structure of the Southern Rhinegraben from Re-Interpretation of Seismic Refraction Data, *Zeitschr. f. Geophys., 55,* 13 – 22, 1984.

# Acknowledgements

I thank Prof. Dr. Friedemann Wenzel for suggesting me to work on this highly interesting topic and for guiding and advising me during the time of my PhD thesis. The discussions with him helped greatly to improve my general understanding of geophysics, and of seismology in particular. Furthermore, I wish to thank him for giving me the possibility to take an active part in the world of geophysics during several conferences and in international cooperations.

I am thankful to Prof. Dr. Karl Fuchs for willing to be co-referent of my thesis, and for discussing the results of my research during the last years in several seminars and, very intensively, in the final stages of this work. The suggestions and ideas he provided helped to improve the thesis considerably.

Special thanks are due to Dr. Kim B. Olsen who gave the ideas to several parts of this thesis and who provided me with his Finite Difference code. He was always available and ready to help when I had questions, answered them very patiently and did not get tired in explaining me the details of the Finite Difference method. Kim read the first version of this thesis carefully and helped to improve it with his comments. I especially want to thank him for inviting me to spend several weeks in 1999 and 2000 at the Institute for Crustal Studies (University of California) in Santa Barbara which I enjoyed as a time of intensive research but also for his delicious home-brewed beer.

I am deeply grateful to Dr. Walter Zürn who critically read the very first version of this thesis and suggested several improvements which helped to make things much clearer. During all the years of my PhD he showed continuous and great interest in my work and loved to discuss the details over a pizza.

Thanks to Dr. Wolfgang Brüstle and Dr. Stefan Stange (Landesamt für Geologie, Rohstoffe und Bergbau, Baden-Württemberg) for providing me with the Rhinegraben data used for the comparison in chapter 2 and for continuously answering my questions about relevant technical details. Dr. Klaus Bonjer helped to improve this thesis with his constructive comments on the results of the Rhinegraben simu-

lations. Thanks also to Dipl.-Ing. Rainer Plokarz who extracted and converted the Rhinegraben data.
Fruitful discussions with Prof. Dr. Zvi Ben-Avraham and Dr. Hillel Wust-Bloch helped to improve my knowledge about both, the seismicity of Israel and the geology of the Dead Sea Rift. I very much enjoyed a visit to Tel Aviv in 2001 which gave me insight into research currently carried out on historic earthquakes and made me see most interesting historical places.
Thanks to Prof. Dr. Raul Madariaga who helpfully adviced on the error analysis and to Prof. Dr. Steve Day who helped with the deconvolution procedure used in the appendix.
I am thankful to my colleagues and the students from the Geophysical Institute for many fruitful discussions, for their help on solving 'technical' problems and for letting me intensively and sometimes exclusively use our parallel computer. Special thanks to Dipl.-Geophys. Joachim Miksat and Dipl.-Geophys. Markus Brenk who I had the pleasure to co-advise during their Diplom theses, and who helped to improve my understanding of the Finite Difference method and their applications substantially. I also thank cand. geophys. Andreas Wüstefeld and cand. geophys. Uli Miksch for their help compiling the 3D-Rhinegraben model.
I want to thank many people without whose continuous support this work could not have been realized: My parents for always being there for me, and, together with my parents-in-law and especially Veronika for spending many days and hours with their grandson Lovis. I thank Gustav for critically reading the German summary of this thesis and for his help with the new German orthography, Sophie, who gave me insight into the dynamic modeling during several presentations at AGU fall meetings and EGS conferences, and taught me a lot about the french way of life, Robert for providing me with his LaTeX- template, Hanna for her company during conferences, and, together with Bettina for many interesting discussions during lunch break.
Finally I wish to thank my wonderful husband Johannes, who especially during those last months always supported me when I was going to work 'just another hour', never complained about the many weekends and long evenings he had to spend without me, and who on the other hand always realized when I did too much and kindly asked me to slow down. His continuous love and support were essential for me to finish this task. Very special thanks are also due to our son Lovis who definitely added a new dimension to my life. He allowed me to finish this thesis in time by sleeping through (most) nights, and shows me every day what matters most.

# Lebenslauf

**Persönliche Daten:**

| | |
|---|---|
| Name: | Ellen Gottschämmer |
| Geburtsdatum: | 22.11.1971 |
| Geburtsort: | Herborn, Lahn-Dill-Kreis |
| Nationalität: | deutsch |
| Familienstand: | verheiratet |
| Kinder: | Sohn Lovis, geb. 30.09.2001 |

**Werdegang:**

| | |
|---|---|
| 1978 – 1982 | Grundschule, Biedenkopf |
| 1982 – 1984 | Berhard-Adelung-Schule, Darmstadt |
| 1984 – 1991 | Viktoriaschule, Darmstadt |
| Sept. – Dez. 1987 | Longcroft-Comprehensive-School, Beverley, UK |
| 13.06.1991 | Abitur an der Viktoriaschule, Darmstadt |
| Sept. – Dez. 1991 | Studium der italienischen Sprache an der Università Italiana per Stranieri, Perugia, Italien |
| Jan. – Mai 1992 | Praktikum am Osservatorio Geofisico Sperimentale, Macerata, Italien |
| Okt. 92 – Juli 98 | Studium der Geophysik an der Universität Karlsruhe |
| 13.07.1998 | Diplom in Geophysik an der Universität Karlsruhe |
| Sept. 98 – Juli 99 | Wissenschaftliche Mitarbeiterin am Geophysikalischen Institut der Fakultät für Physik, Universität Karlsruhe |
| seit Aug. 1999 | Assistentin am Geophysikalischen Institut der Fakultät für Physik, Universität Karlsruhe |

# Erklärung

Ich erkläre hiermit, die vorliegende Arbeit selbständig und nur mit den angegebenen Hilfsmitteln angefertigt zu haben.

Ellen Gottschämmer

Karlsruhe, den 31. Mai 2002